A Characterization of Seal Whisker Morphology and the Effect of Angle of Incidence on Wake Structure

AIDAN WALKER RINEHART

BACHELORS OF SCIENCE IN AEROSPACE ENGINEERING

IOWA STATE UNIVERSITY

submitted in partial fulfillment of the requirements for the degree

MASTERS OF SCIENCE IN MECHANICAL ENGINEERING

at the

CLEVELAND STATE UNIVERSITY

Dec 2016

We hereby approve this thesis for

Aidan Walker Rinehart

Candidate for the Master of Science in Mechanical Engineering degree for the

Department of Mechanical Engineering

and the CLEVELAND STATE UNIVERSITY

College of Graduate Studies

____

Thesis Committee Chairperson, Dr. Wei Zhang

____

Department/Date

____

Dr. Mounir Ibrahim

____

Department/Date

____

Dr. Vikram Shyam

____

Department/Date

Student's Date of Defense 12/08/2016

ACKNOWLEDGMENTS

The author would like to take the next few lines to acknowledge the fact that this work would not have been possible without the help and support of many colleagues, friends and family.

To begin I would like to thank the numerous people at Cleveland State University that have assisted in various ways in my education and research efforts. Foremost among them is my advisor Dr. Zhang who has been an immense help to my development as a researcher. She has helped me to understand the value in a well thought out research question. Her expertise in particle image velocimetry was invaluable as I learned directly from her the incredible capabilities this measurement process provides. I am grateful for the way she challenged me to pursue as many opportunities to present and publish my work along the way. She was also very gracious in working with me to accommodate my challenging schedule of working full-time. Dr. Ibrahim has served the role of counselor from my very first day at CSU as I sought to map out a plan for my education and research goals. In addition to receiving his advice I was fortunate enough to take a couple of his classes and highly value the energy and commitment he had to making sure the students within his class learned as much as possible. Joseph Bunjevac a fellow graduate student has been a needed companion on the long and at times frustrating journey that is graduate school while working full-time. I very thankful for the support and encouragement we were able to share in the classroom and in our research.

In addition to there were a number of folks at the NASA Glenn Research Center that aided my research. First is Dr. Shyam who introduced me to seal whiskers and all of their fascinating properties. While providing a guest lecture at CSU I heard about some of the research that he was conducting in biomimicry and was very intrigued by his application of the seal whisker geometry to a turbine blade. From there he graciously provided me with some foundational information and on every step of the way helped to provide support, resources and connections to people who were able to assist my research. Mr. Rauser provided the expertise necessary to conduct the CT scanning required for the morphology study. Mr. Poinsatte and Mr. Thurman experimental fluid dynamicists helped me understand some of the complexities of establishing a good experimental setup as well as how to overcome those complexities. They were also very supportive and helpful in formulating my understanding of the wake features.

In this season of graduate school and work many of my friends and family have graciously allowed me to be less involved and been very understanding when I was not able to be physically or mentally present. I truly am grateful for the ways you have served me by allowing my to be a little less present. The primary example of this has been my wife, Chelsea. She has been absolutely incredible in this whole process. From seasons of needing to prepare and pack lunch and dinner while taking night classes many of those meals she prepared she never got to eat. To picking up significant slack in ensuring our house didn't turn into a disaster zone. To simply allowing me to work all day and spend all night at school has been a great gift. If these physical things weren't enough she has offered countless words of encouragement when the weight of responsibilities seems to stack up too high. She has pointed and directed my attention back to God when I would become too consumed with the tasks in font of me. I am so lucky to have a best friend and wife who loves me so well.

Finally I would like to acknowledge my savior Jesus Christ. I firmly believe that everything I have I own to him. The fact that he has provided me with abundance such that I could even pursue graduate school is a gift from him. He provides me with confidence, security and hope that cannot be found in anything else. My appreciation

for the beauty that is found in fluid dynamics and nature has grown during this research and made me that much more fond of my creator.

A Characterization of Seal Whisker Morphology and the Effect of Angle of Incidence on Wake Structure

AIDAN WALKER RINEHART

ABSTRACT

Seal whiskers have been found to produce unique wake flow structures that minimize self-induced vibration and reduce drag. The cause of these wake features are due to the peculiar three-dimensional morphology of the whisker surface. The whisker morphology can be described as an elliptical cross section with variation of diameter in the major and minor axis along the length and, angle of incidence, rotation of the elliptical plane with respect to the whisker axis, α at the peak and β at the trough. This research provided a more complete morphology characterization accomplished through CT scanning and analysis of 27 harbor and elephant seal whisker samples. The results of this study confirmed previously reported values and added a characterization of the angle of incidence finding that the majority of angles observed fall within $\pm 5°$ and exhibit a random variation in magnitude and direction along the whisker length.

While the wake effects of several parameters of the whisker morphology have been studied, the effect of the angle of incidence has not been well understood. This research examined the influence of the angle of incidence on the wake flow structure through series of water channel studies. Four models of whisker-like geometries based

on the morphology study were tested which isolate the angle of incidence as the only variation between models. The model variations in angle of incidence selected provided a baseline case ($\alpha = \beta = 0°$), captured the range of angles observed in nature ($\alpha = \beta = -5°$, and $\alpha = \beta = -15°$), and investigated the influence of direction of angle of incidence ($\alpha = -5°$, $\beta = -5°$). The wake structure for each seal whisker model was measured through particle image velocimetry (PIV). Angle of incidence was found to influence the wake structure through reorganization of velocity field patterns, reduction of recovery length and modification of magnitude of T_u. The results of this research helped provide a more complete understanding of the seal whisker morphology relationship to wake structure and can provide insight into design practices for application of whisker-like geometry to various engineering problems.

TABLE OF CONTENTS

LIST OF TABLES

LIST OF FIGURES

NOMENCLATURE

Roman

a	Radius of major axis at peak location
A	Area of ellipse
b	Radius of minor axis at peak location
C	Circumference of ellipse
C_i	Coefficient of the i^{th} polynomial fit
dt	Time step between first and second image pairs
D_h	Hydraulic diameter
D_m	Average diameter of four elliptical diameters
h_i	The i^{th} element of a data set
i	Index
j	Number of image pairs used for ensemble average
k	Radius of major axis at trough location
l	Radius of minor axis at trough location
m	Order of polynomial
M	Distance between peak and trough location
n	Data sample size
N	Total number of image pairs used in ensemble average
r	Recovery length, distance required for flow to return to 90% of U_o
Re	Reynolds Number with D_m as reference length
Re_{Dh}	Reynolds Number with hydraulic diameter as reference length
T_u	Turbulence intensity of the u velocity component
T_v	Turbulence intensity of the v velocity component

T_w	Turbulence intensity of the w velocity component
u	Velocity in the x direction
$u^{'}$	Velocity fluctuations in the x direction
U_o	Freestream velocity
v	Velocity in the y direction
ν	Kinematic viscosity
w	Velocity in the z direction
x	Cartesian coordinate aligned with major axis of whisker model
y	Cartesian coordinate aligned with minor axis of whisker model
Y_j	Savitzky-Golay smoothed data
z	Cartesian coordinate aligned with axis of whisker model

Greek

α	Ange of incidence at the peak location
β	Angle of incidence at the trough location
Δ	Difference
ϵ	Eccentricity of whisker cross section
λ	Distance between neighboring peaks or neighboring troughs
∇	Curl operator
$\tau^{''}_{xy}$	Reynolds shear stress in x-y plane
$\tau^{''}_{xz}$	Reynolds shear stress in x-z plane
ω_y	Vorticity about the y axis
ω_z	Vorticity about the z axis

Subscript

i, j, k	Index
max	Maximum value
rms	Root mean square value
$peak$	Peak location
$trough$	Trough location
h	Hydraulic
m	Mean
x, y, z	Cartesian component
u, v, w	Velocity component

Accent

$\lvert()\rvert$	Absolute value
$\overline{()}$	Average (ensemble)
$()'$	Fluctuation

CHAPTER I

Introduction

1.1 Biomimicry

The area of biomimicry has gained a heightened level of interest as engineers and biologists seek to understand how different features in nature have evolved over time to optimize various functions and abilities observed in nature. In particular the aerospace community has found this field to be particularly enlightening looking at aerodynamics, materials, and control theory [6, 8, 65]. A few examples are provided to give the reader a glimpse into biomimicry breadth with focus on the aerospace community.

One of these areas revolves around the unmanned aerial vehicles (UAVs) and micro UAVs. Due to the scale of some designs, typical aircraft design philosophy does not scale appropriately. In an effort to address some of the design challenges researchers have looked to nature, specifically birds and insects, to understand how different features observed in nature address the challenges of flight.

One example of this is found in the hummingbird wing design and wing stroke pattern which have been studied extensively due to the bird's ability to hover and the incredible rate of flapping required. The wings pass through a figure 8 that generates lift in both down and upward strokes [20,21,28]. It is often referenced that the famous helicopter designer Igor Sikorsky was inspired by the hummingbird and more recently helicopter designers have returned to look at hummingbird design to gain efficiency in rotor blade design [44].

Similarly general research into the unique rotations and morphing associated with insect flapping wings has been investigated as these flight mechanics are far more complex than conventional aircraft flight dynamics [15]. Micro UAVs have found great inspiration through the study of various insects. High speed cameras have been used to observe the various twists and rotations present in the bumblebee flapping motion with follow on work to extract how those motions contribute to lift generation [16,17]. One specific research group has recently focused on bumblebee flight mechanics and have successfully replicated the flight dynamics in a micro air vehicle [68].

Another insect to gain interest in the aerospace community is the dragonfly. Research on the dragonfly wing can be traced as far back as 1975. The comparatively large size of the dragonfly made it a good candidate for optical analysis. In addition the dragonfly's unique corrugated wing features, shown in Fig. 1, have been found to reduced flow separation and increased lift. These features have been applied to small UAVs requiring lightweight wing design while also addressing flow separation [42,56,69].

Still within the aerodynamic realm of interest is the humpback whale flipper. Tubercles, bumps along the leading edge of flippers, have been understood to aid in maneuverability of the humpback whale known for its sharp turning and rotating capabilities. These designs features have been applied to the leading edge of wing profiles and found to increase the maximum angle of attack achieved before stall and

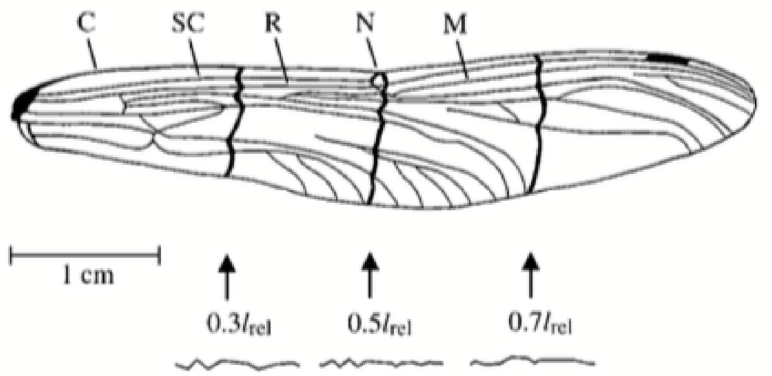

Figure 1: Drawing of dragonfly wing with cross section profiles identifying corrugation [42]

improved lift features [19, 34, 40, 47, 49, 71]. An example of the test articles used to identify the aerodynamic features of tubercles is shown in Fig. 2.

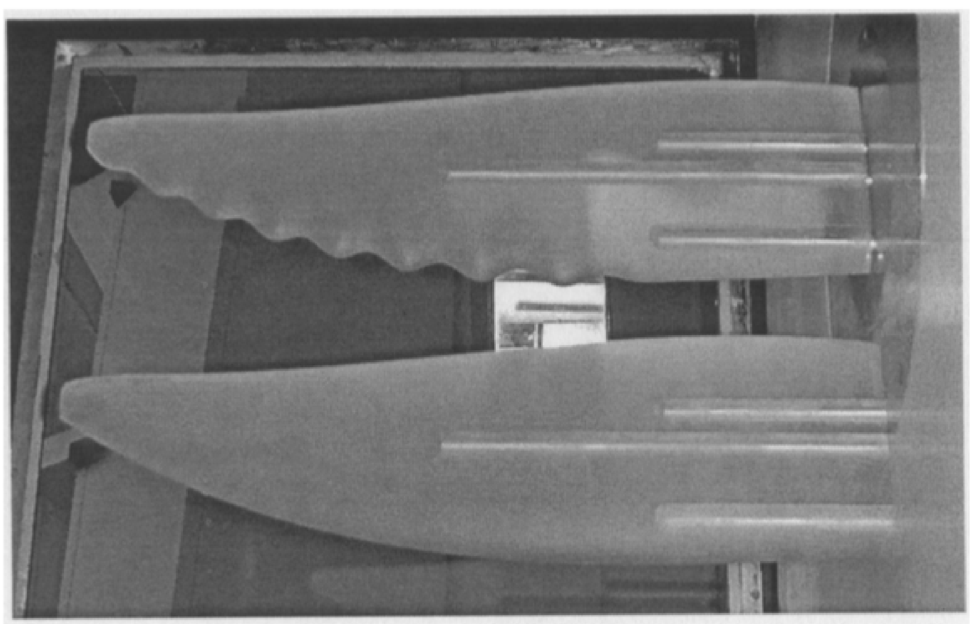

Figure 2: Wind tunnel test articles studying the effect of tubercles observed on humpback whales flippers [49]

1.2 Seal Whisker Sensing

The previously mentioned list is a very limited survey of a few areas where biomimicry has yielded some fascinating results and insight into how nature addresses various design challenges. Going forward an in depth review of research surrounding the unique features of seal whiskers will be provided as a foundation for the focus of this paper.

Pinnipeds or more commonly, seals, are a class of semiaquatic mammals. There exist a wide range of characteristics defining the different species of seals, but for this research focus will be given to the vibrissae or whiskers. Seals posses one of the most highly developed array of whiskers which has lead to various studies to define their capabilities and understand how the seal utilize their whiskers for sensing. Whiskers among seal species vary and can be grouped into two categories smooth and undulating [23]. Figure 3 shows an example of some undulating and smooth whisker species.

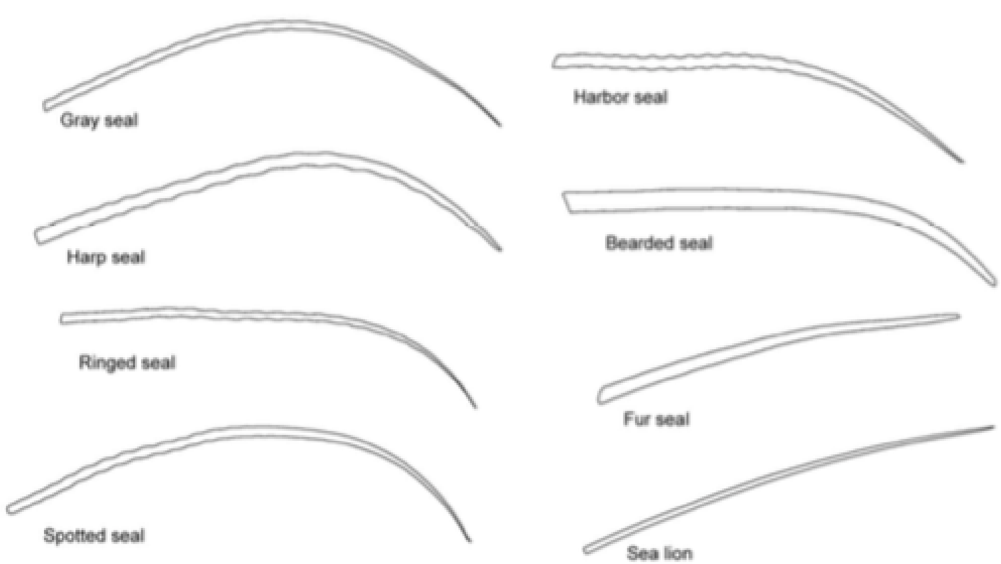

Figure 3: Examples of seal whisker morphology in undulating (Phocid) and smooth (Otariids) surface features [23]

All seals posses whiskers that are useful in various methods of sensing and communication [2]. Seals split their time living on land and in water which provide vastly different environments. It is postulated that different sensory systems are utilized in these different environments allowing seals to operate effectively in a wide range of environments [58]. Harbor seals have an ability to sense how fast they are traveling in water that is believed to be discerned with their whiskers [59]. Optic flow analysis, the pattern of apparent motion elicited on the retina during movement, has been observed within seals. Finding that the seal could use particles in the flow to deduce flow direction within 1° of heading direction [25]. Harbor seals have also been found to effectively navigate to precise locations for breeding over long distances even with human intervention and disorientation suggesting that their overall sensory abilities are finely tuned [39].

Seals typically hunt by periodic diving and surfacing; they can be observed to dive as low as 350 m deep and typically the water is covered with ice producing low visibility for the seal [48]. Whiskers have been postulated to be necessary for hunting in these low light environments. Seals often have visibility limited to 2 meter in the areas they hunt. Whiskers could possibly be used to sense sound and compression waves [36]. Early investigations to understand exactly what role the whiskers play included experiments with captive harbor seals. Seals were successful in locating an air hole in a frozen tank while blindfolded, eliminating visual cues; yet when their vibrissae were obstructed the same seals struggled to locate the air hole [57, 66]. This observation of the vibrissae's role in detection was evaluated even further when a captive seal was trained to track a toy submarine and showed equal capability to follow the hydrodynamic trail created by the toy submarine when the seal was equipped with a blindfold and earmuffs, shown in Fig. 4, canceling out visual and audio cues [10]. Follow on studies had California sea lions, whose whiskers are smooth consistent cross sections, perform the task of tracking a toy submarine. It was observed that the California sea lion were equally successful in locating the submarine when no initial wait was required; however, the California sea lion were far less successful than the harbor seal in locating the submarine when requiring an initial delay [26]. These studies suggested there was an enhanced ability to sense due to the unique geometry of the harbor seal vibrissae.

Figure 4: Harbor seal with blindfold and ear muffs preparing for wake tracking experiment [10]

A similar study was conducted to discern the interplay between visual and tactile sensory input for navigation. Grey seals, another beaded seal specie, were trained to navigate mazes in various lighting conditions. It was observed that under well light situations seals rely predominantly on visual cues while in dim settings tactile cues from the whiskers play a dominate role in navigation [53]. This reliance on whiskers for navigation during low light situations is not limited to seals. Hyvarinen has conducted various studies identifying how vibrissae over a range of mammals are used to aid nocturnal and limited light hunters [36–38].

Experiment have also shown that while blindfolded various species of seals are capable of differentiating size of various object through vibrissae tactile sensitivity. This is accomplished through comparison of the Weber fractions, a measure of tactile acuity. Harbor seals were found to have size discernment sensitivity on the same range as hands [11–13, 41]. Tactile sensitivity for the harbor seal was examined in both air and under water environments with no discernible difference in sensitivity observed suggesting that the sensitivity is not limited or impaired significantly in by the operating medium [14].

Specifically looking at the whisker of beaded seals and their unique ability to provide superior sensing has been established through various studies as described in the following section. Harbor seals are among the longest vibrissae making them some of the largest known animal active flow sensors [64]. Growth rate and shedding rate of the vibrissae were captured for harbor and grey seals finding that vibrissae shedding did not occur with annual molting and the seals employ other methods for ensuring sufficient coverage of vibrissae [27, 35]

In a comparison of various mammal mystacial vibrissae, whiskers located near the mouth and nose, it was observed that beaded seal vibrissae showed a significantly higher rate of response to both low and high frequency vibrations that are not uniquely tied to an aquatic adaptation [18]. In addition beaded seal whiskers show more flexibility when compared against non-beaded vibrissae [24]. The combination of the reduced vibrations associated with beaded and the increased flexibility likely function to enhance sensitivity of the vibrissae.

The ring seal, a beaded seal, posses 2-5 times the number of Merkel cells within the sinus when compared to cats thus suggesting that the role of the vibrissae in the seal is of greater sensory significance [37, 38]. The increased sensitivity is observed in seals ability to resolve vibrations in the range of 50-1000Hz [50, 60]. The natural frequencies calculated for harbor and harp seals are in the range of 20-200Hz suggesting that different whiskers may be tuned to be excited at different frequencies [33, 63].

More specifically how these whiskers are able to resolve wakes and fluctuations of incoming flow have been observed in other species such as the catfish. Investigation into the use of wake for tracking prey has also been investigated in catfish and guppies [54]. These same abilities were hypothesized to exist within the seal. The wakes left by prey fish has been described by their respective wake size as well as how long the wake persist. Various studies have quantified wakes left by fish ranging in size from 38 mm to 100 mm these wakes can last up to 5 minutes after the fish has left [30, 31]. These quantities are helpful in grounding how likely it would be for seals to be able to sense and track the wakes left by prey.

Developing on these observations others identified that the undulating geometry helps to breaks down and suppresses vortex induced vibration shown in Fig. 5. This lead to the hypothesis that the beaded vibrissae provides greater sensitivity to incoming flow disturbances and aids in the ability to track hydrodynamic trails [29]. Delving even further into the fundamentals of the vibrissae flow physics was a decomposition of the undulating features and their relationship to generated forces on the vibrissae finding that both undulations on the major and minor axis are necessary for the disruption of strong von Karman vortex street [32]. A comparison of whisker-like geometry to similar non-undulating circular and elliptical cross-section and an undulating circular cylinder found the whisker-like geometry to reduce the recirculation zone and disrupt organized vortical structures [70]. Other studies have focused on quantifying the sensitivity of the beaded whisker to detect fluctuations as well as the impact of the angle orientation of the whisker to flow [52].

As the ability to reduce self-induced vibration was realized some efforts shifted to applying this function to enhance performance of various engineering problems.

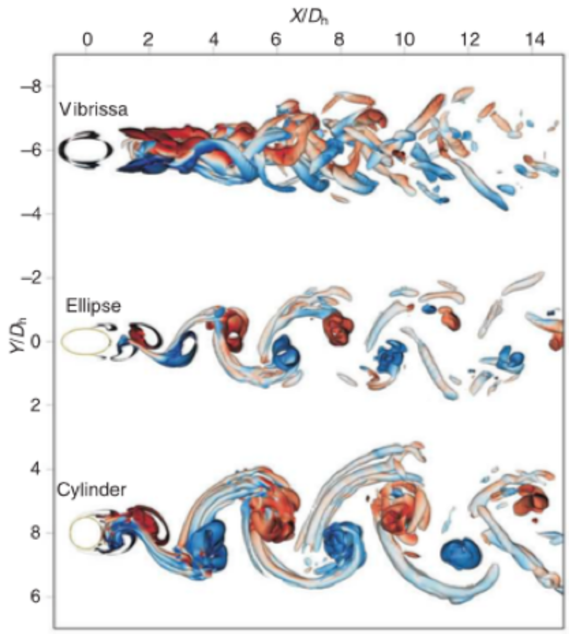

Figure 5: Comparison of wake Q-criterion (rotational strength) of circular, elliptical, and whisker-like cylinders. Showing the whisker's ability to break coherent vortex structures [29]

One of which involved designing novel flow sensors that utilize the geometry observed in the beaded seal whiskers [5]. In addition to novel flow sensors the geometry's ability to reduce drag has inspired investigation into modifying the geometry of gas-turbine blades for enhanced performance [65]. Other possibilities for the beaded seal vibrissae geometry include structures in consistent flow paths such as wind turbine towers, sensor mounting supports on aircraft frames, and offshore oil drilling rigs. This range of potential application provides a rich environment and motivation for developing a more complete understanding of the unique geometry of beaded seal whiskers.

The beaded seal whisker has proven to be a very interesting area of research with many nuances. Due to the complex morphology of the seal whisker there are several areas that have not been fully understood as research has simplified the geometry to establish baseline understanding for some of the associated phenomena. One of the areas that has not been fully understood is the influence the angle of incidence has on the whisker's wake structure. Previous studies that have focused on describing the morphology of the whisker have mostly focused on length parameters and little attention have been given to characterizing the angle of incidence. When the angle of incidence has been reported the sample size is small and does not provide sufficient evidence for generalization. Furthermore when computational and experimental fluid dynamic research has been conducted on whisker-like geometry the angle of incidence, α and β, have always modeled as a constant value. Where these prior research efforts have left off this study will pick up. This study will address the limited data available on the occurrence of the angle of incidence by analyzing the morphology of a larger sample size of beaded seal whiskers. The results of the morphology study will guide the design parameters of the whisker-like geometry used in the wake flow study. Finally the flow study of various whisker-like geometries will inform how the angle of incidence affects the wake structure.

1.3 Outline of Current Study

The aim of this paper is to provide a more complete characterization of two species of beaded seal, the harbor and elephant, vibrissae geometries that could provide design guidelines for applying this geometry to various engineering applications. Then using those geometry characterizations build on the present flow physics research of the beaded vibrissae whisker by characterizing the effect the angle of incidence has on the wake structure.

Chapter 1 provided some background on how biomimicry has been used in the past to gain greater insight into adaptations within nature. It also established a baseline and framework for the research that has already been conducted in the realm of seal whisker morphology and wake structures.

Chapter 2 establishes the nomenclature needed to define the morphology of beaded seal whiskers. A CT scanner and image processing are used to characterize the morphology of 27 harbor and elephant seal whiskers. Observations of morphology characterization and trends are presented for the whiskers sampled.

Chapter 3 defines the fluid dynamic study experiment. Four models with different angle of incidence patterns are used to observe the wake structure created by the whisker-like geometries. This survey of different angle of incidence details how the angle of incidence contributes to the unique wake structure observed in seal whiskers.

Chapter 4 provides a summary of the key findings obtained trough this research.

Chapter 5 outlines whisker-like wake structure features that are still not well understood as well as potential areas for extending the research presented within this thesis.

CHAPTER II

Characterization of Whisker Morphology

2.1 Introduction

Seal whiskers that possess undulating surface features have been identified as early as 1977 and remained a source of interest and study to today [23, 43, 46]. Some of their basic morphology has been characterized and even shown to provide a distinct indicator of the species of seal [23]. Beaded seal whiskers can be thought of as a series of ellipses that are lofted about the length of the whisker. These ellipses vary in the major and minor axis along the length of the whisker producing smooth undulating features in both the major and minor axis. In addition to the variation in major and minor axis diameters the plane on which the ellipse reside experience a rotation with respect to the axis of the whisker. This rotation of the ellipse plane will be referred to as the angle of incidence which produces a variation between the location of the leading and trailing edge of the whisker along the major axis. Finally the axis of the whisker also exhibits curvature that is minimal near the root and increases towards the tip of the whisker. For the purposes of this paper we will be adopting the

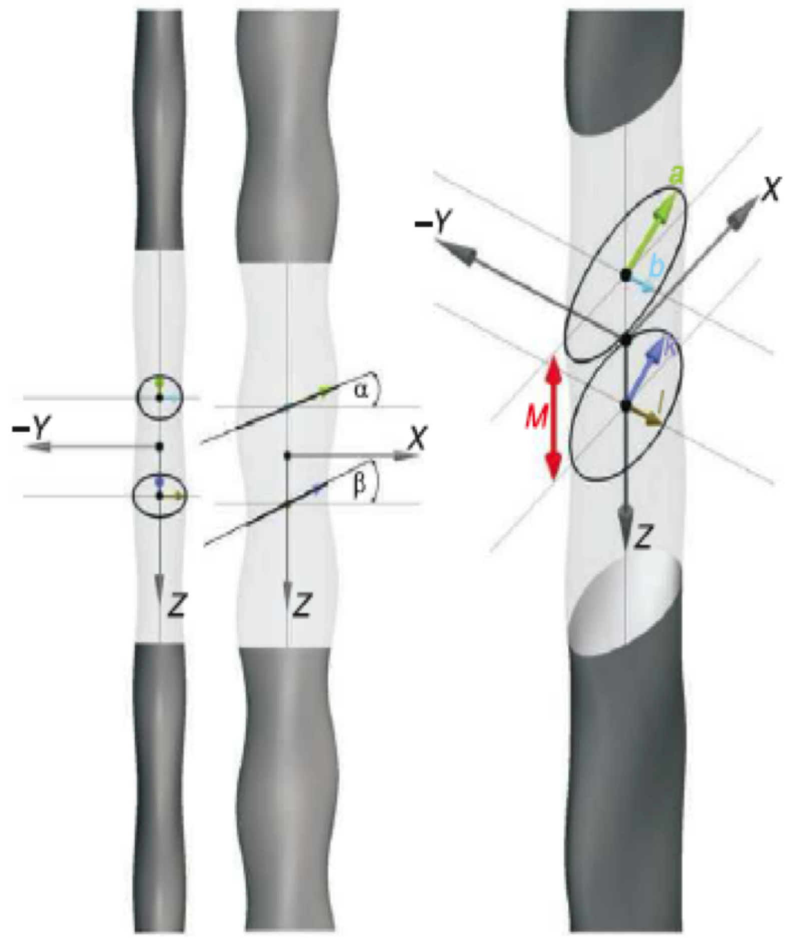

Figure 6: 7 Parameter Whisker Definition provided by Hanke et al. [29]

parameterization outlined by Hanke et al. where he used a seven parameter system to completely define the Harbor seal whisker geometry [29].

As indicated in the figure the above the ellipse defined at the peak location is characterized by a major axis radius of a and minor axis radius of b and an angle of incidence α. The trough geometry is defined by the major axis radius k, the minor axis radius l and the angle of incidence β. Finally the half wavelength, or distance between the peak and trough location is defined by M. While some of these parameters have been measured for various beaded seal whiskers other have limited data sets available. Primarily the angle of incidence is not a strongly reported feature when beaded seal whisker geometry studies have been conducted in the past.

Previous studies that have reported these values have had limited sample sizes making definitive characterization impossible [51]. The intent of this section is to build off the available data sets characterizing beaded seal whisker geometry and add to the publicly available datasets to provide greater confidence in generalizing features of beaded seal whiskers particularly in the area of characterizing the angle of incidence.

2.2 Methodology

Previous research to this point has focused on whisker models that have a constant angle of incidence [5,29,32,65]. Often within these studies no explanation of why a particular angle was chosen is provided by the author. This research conducted a morphology study of seal whiskers to establish how the angle of incidence occurs within nature with the intent to use the results to inform and bound the follow on flow study. The expectation being that if certain magnitudes, patterns or direction are more beneficial than others they might be observable in nature. The measurement of the seal whiskers was accomplished through a three step process; the whiskers were subjected to a CT scan, those scanned images were processed with ImageJ to identify the surface of each whisker, the ImageJ surface feature extractions were reconstructed and processed to capture the seven identifying parameters with a custom Matlab code.

2.2.1 Measurement Tool Selection

The characterization of the whisker geometry began with investigation into which method would yield the most reliable results. Several key features were considered for the morphology study. First the whiskers are highly three dimensional therefore the measurement tool and process need to accommodate these variations. The whiskers need to be mounted in a secure fashion that does not distort the natural geometry of the whisker. The measurement tool needs to have spatial resolution that provides finer resolution that the smallest detail of the whisker. Differences in the whiskers are assumed to be small and easily corruptible by human error. Finally a large sample size is required for generalized observations and therefore speed and efficiency of measurement is also important. These requirements will be used to evaluate three different measurement options available to this research.

Initial measurements were obtained through a Zeiss Axioscope microscope, Fig. 7, at the NASA Glenn Research Center [74]. This method required mounting the whisker on a flat plate with aid of putty securing the whisker during measurement. Measurements were taken along the major axis and then the whisker was rotated 90° to measure the minor axis. Using the associated software guide lines were over laid to provide measurements of the 7 whisker geometry parameters defined in Fig. 6. This method was found to be impractical due to the high reliance on operator discernment. The operator discernment manifested itself in the selection of points that defined the peak and trough locations on the leading and trailing edges as well as mounting the whiskers on their proper axis. Another deficiency of the microscope is the lengthy time requirements to capture measurements. Due to the dependence on the operator discernment it was determined if this method were to be pursued measurements would need to be repeated multiple times and an average value taken from the repeated measurements to limit error introduced by the operator.

An Asylum MFP-3D-IO Atomic Force Microscope located at CSU was used to measure a sample whisker for determining which measurement technique to select [3]. This microscope is designed for analyzing biological material and captures high resolution topographical images. Similar issues observed while measuring with the electromagnetic microscopes at NASA were still present with this method although the features were slightly more readily identified due to the topographical feature of the microscope. The ability of the microscope to capture images at multi-

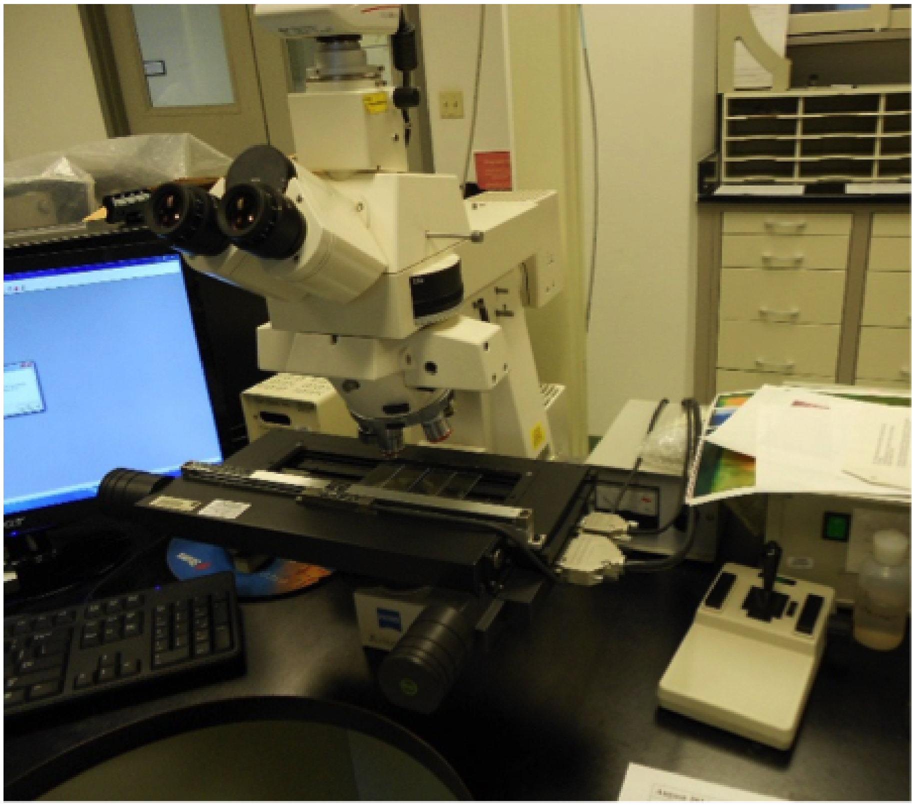

Figure 7: Zeiss Axioscope Microscope at NASA Glenn Research Center

ple focal points and then reconstruct them to provide a depth sensitive image yielded greater confidence to selection of true peak and trough locations as well as reduced the skill needed to position the whisker precisely on the major and minor axis for measurements. An additional constraint provided by this tool was the requirement of a trained expert to operate the machine.

The final option tested was the computer-tomography scanner (CT Scanner). This method provided high resolution available through the x-ray cross-sectional slices. Perhaps the greatest advantage provided by the CT scanner is minimizing the operator influence. The CT scanner provides the user with complete surface geometry with the re-assembly of the cross-sectional slices which lends this method more easily to the use of computerized methods identifying the peak and trough locations instead of the human eye. One of the down side of the CT scanner is that

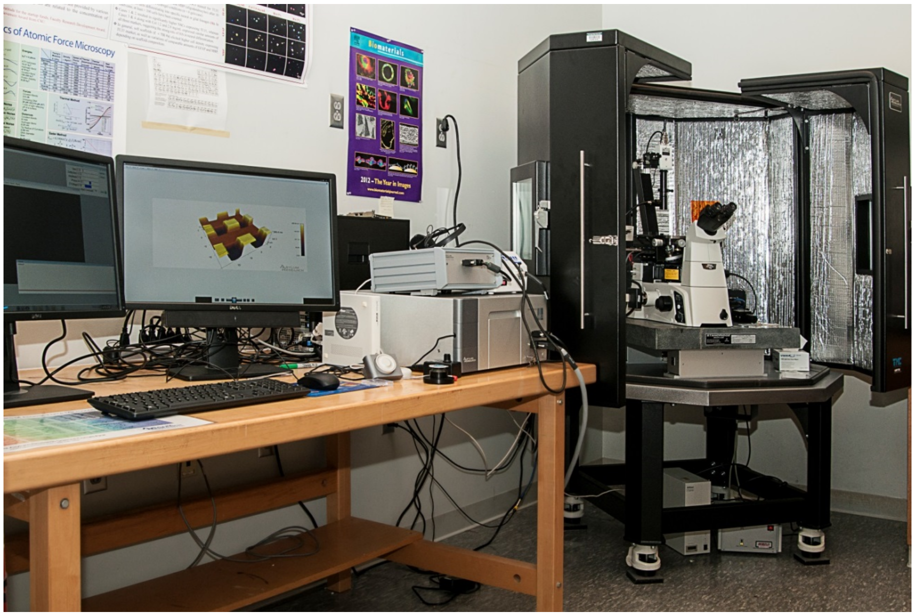

Figure 8: Asylum MFP-3D-IO Atomic Force Microscope at Cleveland State University

is requires a highly trained operator to select appropriate settings to ensure surface features are properly resolved. The time required to conduct a scan due to the detail required by the size of the whisker was long. In addition the cost to operate the CT scanner is significantly higher than operation of the microscope options available to this research task. Further details about the particular CT scanner will be provided in the following section.

These observations on techniques for characterizing whisker morphology are similar to those experienced in other efforts to characterize vibrissae. Where Ginter et al. conducted measurements with a SLR camera and a dye to enhance the contrast between the whisker and the mounting background [23]. Those images were then processed utilized multiple imaging software tools to that either extracted the outlines of the whisker through threshold analysis or traditional techniques of operator selection of points of interest were identified. Murphy et al. obtained measurements through CT scanning and image processing tools to extract various surface features [51]. Finally DeArmon et al. investigated multiple techniques including; 3D scanner, microscope and CT scanner finally selecting the CT scanner as the method of choice [9].

After exploring the three options available to this research effort the CT scanner was selected as the method of choice. The sample measurements obtained while using the microscopes at NASA Glenn revealed that too much of the measurement process depended on operator discernment and might not be readily reproducible. The microscope located at CSU did not provide sufficient improvement from the results and operator dependency experienced at NASA Glenn. In addition it was found that even with the long time required for the CT scanner to scan the length of the whisker measurements were obtained much faster than those obtained through microscope measurements through the automation of computer code. The result of this initial investigation was selection of the CT scanner as the tool for characterizing the whisker morphology.

2.2.2 CT Scanner

CT scanners have become increasingly common in the field of non-destructive evaluation due to the advancement of the key components critical to CT scanners [61]. The CT scanner's rise at a tool for analyzing material is linked to their ability to capture fine detail from large scale items on the order of 1 m down to the sub 1 µm. CT scanners provide a wide range of function including but not limited to; evaluating build quality of new manufacturing techniques, assisting in medical diagnosis, reverse engineering, inspecting fatigue, and general 3D digitization for measurements [7]. CT scanners are measurement tools that function by emitting x-rays through an object of interest and collecting the emitted x-rays on the opposite side of the object. The collected x-rays create a grey scale image. The values of the grey scale image can then be interpreted to understand features of the object of interest by relating darker areas in the grey scale image as areas of high density. The dark areas on the grey scale image received little to no x-rays on the detector plate. In constrast the areas of lighter grey indicate that more or most of the x-rays were able to pass through with little to no interference from the object of interest. This relates to low density in the object of interest.

The particular CT scanner used for the whisker characterization is a custom designed North Star Imaging Inc. machine [1] located at the NASA Glenn Research Center. It is comprised of three primary components; the emitter, object platform, and detector. The emitter is an XRayWorX emitter; it operated at a voltage of 90 kV and current of 60 μA. The object platform is simply a rotating pedestal allowing images to be captured from every angle and then reconstructed. The detector plate is a Dexela 2923; it operated at 4 frames per second with a pixel pitch of 75x75 μm. The distance from the emitter tube to the detector plate was 760 mm. Below is a figure depicting the layout of the CT scanner used in characterizing the seal whisker geometries.

The whisker samples were mounted in a Styrofoam cylinder providing a stable position for the whiskers to be accurately scanned without shifting during the scanning process. The Styrofoam also provides a drastically different density than the whisker; this is key to being able to clearly distinguish between the two materials being scanned. Whiskers were pressed in thin slits cut in the Styrofoam cylinder. The cylinder with whiskers was then mounted to the CT scanner platform. Below is one of the Styrofoam cylinder whisker mounts created for the CT scanning. This particular mount held eight unique seal whiskers.

A summary of the different scanning cases is presented below. These scanned whiskers will provide the data necessary to characterize the geometry of the seal whisker.

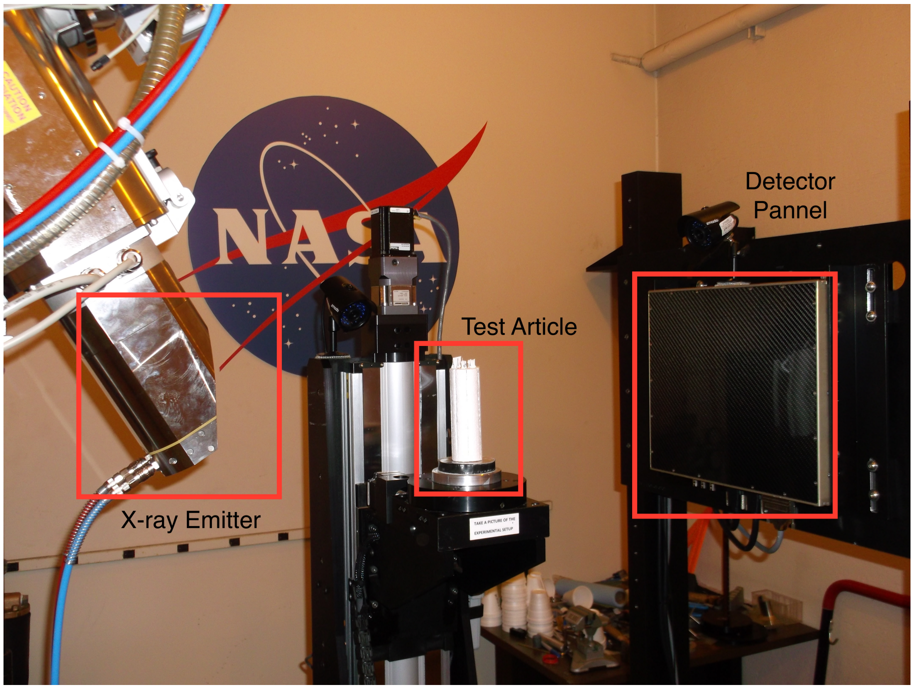

Figure 9: CT Scanner at NASA Glenn Research Center

Table I: CT Scanning Summary

	Number of Whiskers	Number of Cross Sectional Slices	Voxel Size (μm)
Case 1	3	2595	4
Case 2	8	2290	4
Case 3	10	2254	4
Case 4	8	2750	10.5
Case 5	8	2745	10.7
Total	37	12634	

The range of voxel size is due to the different windows of interest. The smaller 4 μm voxels relate to scans where a small length of the whisker was in frame capturing 2-3 peaks and trough features per whisker. The smaller window allowed for the surface detail to be observed; however, this is not the focus of our study and will not be discussed further. The larger 10.5 and 10.7 μm voxel sizes focused on much longer length sections of the whisker samples and captured up to 10 peak and trough features per whisker. The different cases were conducted to provide a range of species, seals, and when possible multiple whiskers from the same seal. The cost of running the CT

Figure 10: Whiskers Mounted in Styrofoam

scanner and availability of seal whisker samples were limiting factors for this study. The total number of whiskers measured with the CT scanner is 37; however, 10 of those whiskers are California sea lion whiskers which do not feature an undulating surface and will not be discussed within this study leaving 27 whisker that posses undulation to be characterized within the remainder of this study.

The CT scans were also compiled in a 3D viewing executable that was not sufficient for extracting measurements, but still provides a helpful understanding of the CT scan setup and results. A reconstruction of one of the cases with 8 whiskers mounted radially about a styrofoam cylinder is provided in Fig. 11.

2.2.3 Image Processing

The images created by the CT scanner were then processed with ImageJ [4]. ImageJ is an image analyzing software suite that provided the resource of identifying the edge of each whisker within the images. This was accomplished by identifying a threshold value for the grey scale that accurately categorized the Styrofoam and whisker as two separate object. ImageJ provides a features called 'Analyze Particles,' this tool is designed to identify separate objects in the provided image based on the

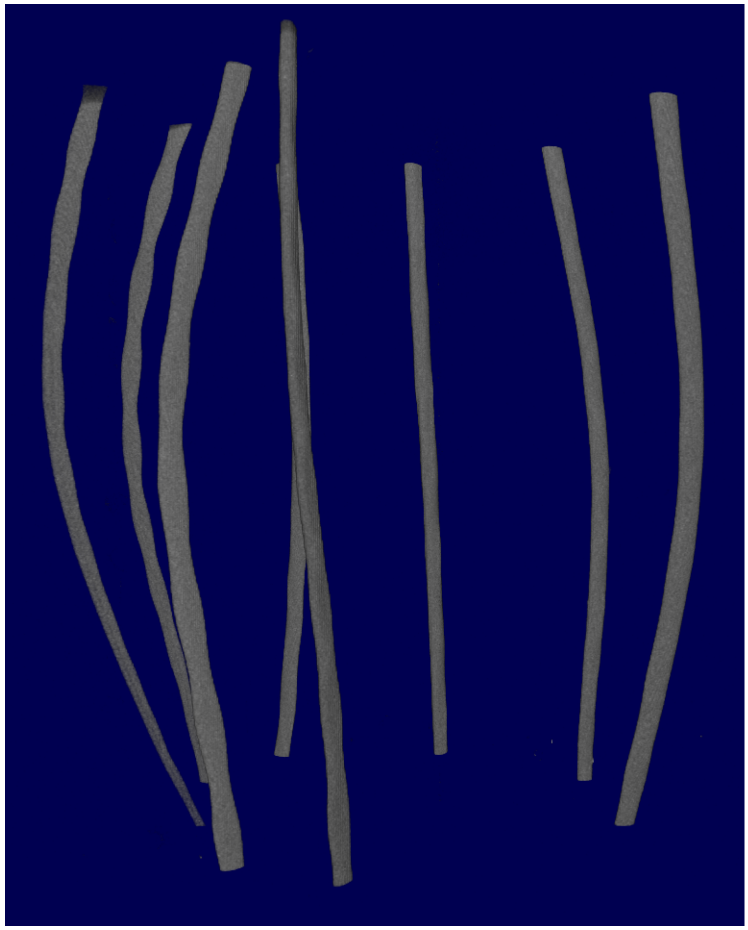

Figure 11: Whisker Reconstruction from CT Scanner

user provided threshold value. A script was written to automate the process for the thousands of images representing each cross sectional slice of the whiskers. The thresholds were manually identified for each CT scan as the intensities varied and needed to be fine tuned to produce the best results for batch of CT scanned images. The final part of the script created data files providing the x and y coordinates for each whisker outline. An example of the raw image produced by the CT scanner and the first stage of processing done by ImageJ is show below. Where the grey scale CT scan image is on the left and the two tone image in the center is the result of ImageJ applying the threshold then finally on the right the outlines of each whisker identified by the analyze particle tool.

After the outlines of each whisker have been identified the x and y coordinates

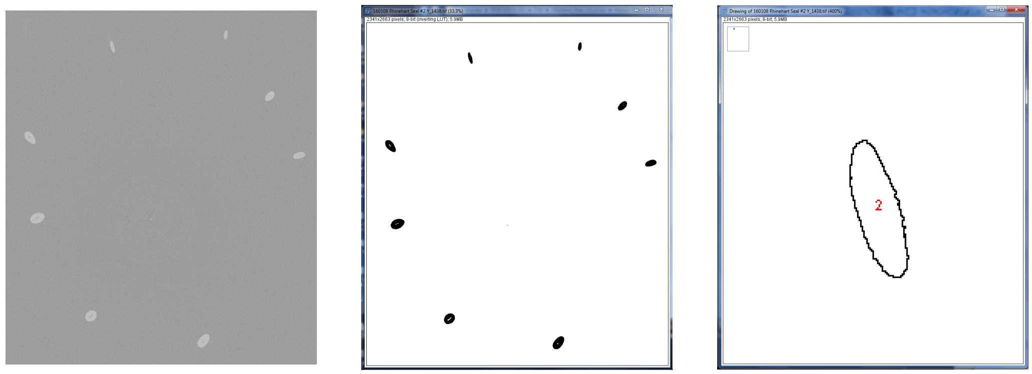

(a) Whisker Cross Section Image from CT Scanner

(b) Results of ImageJ Threshold Analysis

(c) Results of ImageJ Particle Analysis

are saved to data files for further processing with Matlab. There parameters of interest; a,b, k, l, M, α, and β will be extracted at the peak and trough locations along the length of the whisker samples.

2.2.4 3D Reconstruction and Parameter Extraction

The next step was to process the x and y coordinates data files generated by ImageJ. Each cross sectional slice contained multiple whiskers which needed to be properly identified so that the each individual whisker could be reconstructed. Once the whiskers were reconstructed the seven geometry parameters could be extracted for the entire length of the whisker that was scanned. This was accomplished with a custom Matlab code that identified the four end points defining the major and minor axis of each whisker at each cross sectional slice. The end points were identified by calculating the distance of each outline point to the centroid of the outline. The largest distance was identified at the major axis and from the major axis the minor axis was identified being perpendicular to the major axis. The major axis was broken into leading and trailing edge data sets. The distances were smoothed using the combination of an outlier removal followed by a moving window average and a Savitzky-Golay filter function [62]. The Savitzkt-Golay filter applies a polynomial fit to the data set with the advantage of maintaining the integrity of the peaks and troughs within the smoothing process. This is of critical importance for identifying the correct location of the peaks and troughs along the whisker length. The following three equations define the moving window averaging followed by the Savitzky-Golay filter function.

$$\overline{h}_i = \frac{h_{i-2} + 2h_{i-1} + 3h_i + 2h_{i+1} + h_{i+2}}{9} \tag{2.1}$$

$$Y_j = \sum\nolimits_{i=-(m-1)/2}^{i=(m-1)/2} C_i y_{j+1} \tag{2.2}$$

$$\frac{m+1}{2} \leq j \geq n - \frac{m-1}{2} \tag{2.3}$$

Here y_{j+1} is the raw data and C_i is the coefficient of the polynomial fit, m is the order of the polynomial and n is the data sample size. Finally Y_j is the smoothed data. Equation 2.3 is the range over which the Savitzky-Golay filter is allowed to operate.

The following two figures show an example whisker being processed. The figure on the left is the reconstruction of a whisker displaying the centroid in green, leading in red and trailing edge in blue along the length of the whisker no smoothing has been applied to the coordinates of the whisker outline at this stage of the processing. The figure on the right shows the same whisker after calculating the distance from the centroid for the trailing edge and identifying the peaks and troughs of the trailing edge. The displacement is show in the blue line where the peaks are identified by red squares and the troughs are identified by green squares.

The peak and trough locations are stored then the seven geometry properties that define the whisker are calculated. It should be noted that the overall whisker experiences varying degrees of curvature along the length of the whisker as well as from sample to sample. The approach taken in this measurement method was to focus

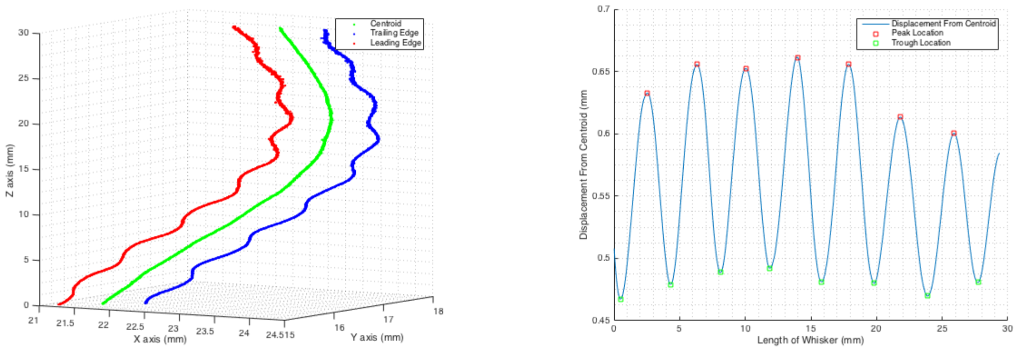

(a) 3D Reconstruction of Leading and Trailing Edges

(b) Trailing Edge Peak and Trough Identification

on scanning the mid sections of the whisker where curvature is limited. In addition it was assumed that due to the measurements being conducted in a piecewise fashion, that is to say lengths calculations are only performed between two adjacent peak of trough points, that the curvature would have a minimal effect on the measurement and could be ignored. This assumption was shown to be acceptable as the wavelength measurements obtained in this study show strong agreement with literature explained in greater detail in the next section [23].

Once all of the whisker data sets were processed a statistical analysis was performed on the extracted properties to identify trends and patterns in the whisker morphology. The results of the morphology study are summarized in the following section.

2.3 Results

This section will present the results of the whisker measurements identifying the geometry features of the seal whisker. As a brief recap the following data represents the findings of the 27 whiskers analyzed by the above process. Of primary interest in this study was to determine how the angle of incidence occurs in nature. This question was prompted due to multiple studies utilizing scaled up models of harbor seal whiskers that defined a constant angle of incident. These angles of incidence choices were often not explicitly explained. As a result it was deemed prudent to conduct our own study to see of these angles appeared in nature and then moving forward we would be better equipped to make decisions on how to design representative whisker models for the flow study.

Whisker samples were provided by The Marine Mammal Center, a nonprofit veterinary research hospital and education center located in Sausalito, California. Whisker sample were collected from deceased seals that were found by the research center or brought to the center for rehabilitation, no seals were harmed in the collection of these whisker samples. Each seal was given a unique identifier consisting of two letters defining the species of seal followed by a four digit number distinguishing the seal from others. Multiple whiskers from each seal were packaged in plastic bag and shipped to the NASA Glenn Research Center.

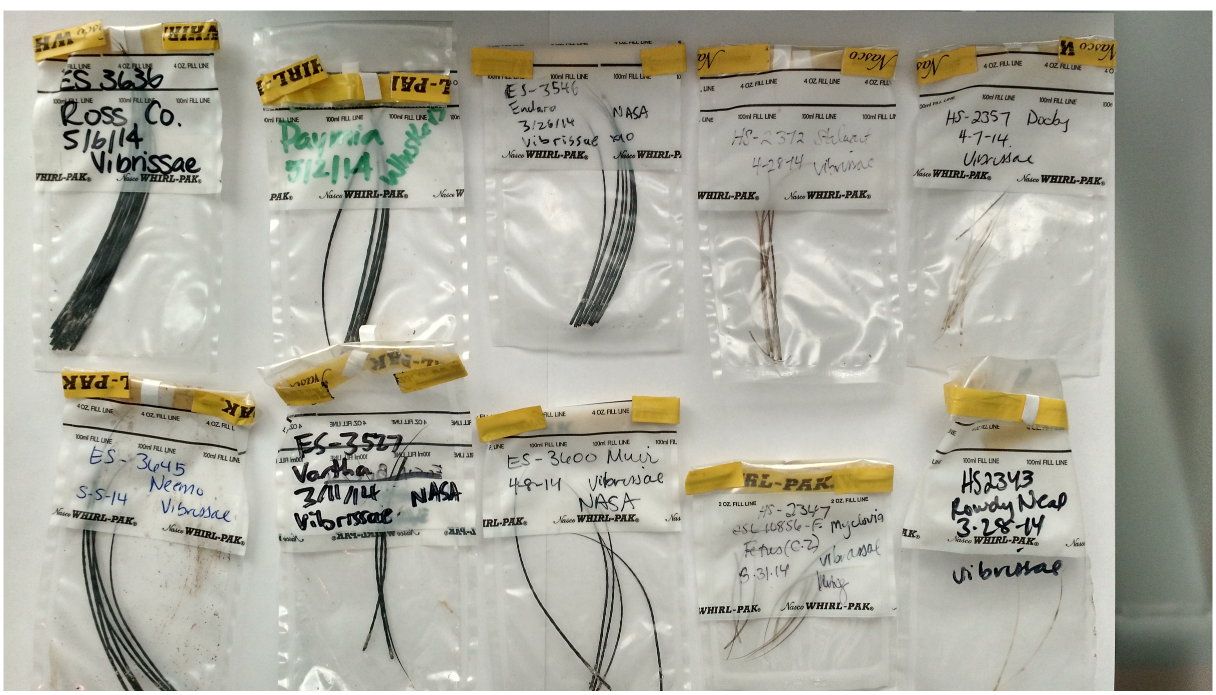

Figure 14: Whisker Shipping Packets

What this means is that each seal has a unique identifier but the whiskers themselves do not; therefore, in the following results if an identifier appears multiple times it should be understood that multiple whiskers from the same seal have been measured. Below is a break down of the seal samples provided for this study and some basic information about the seal.

Table II: Seal Information

Field ID	**Name**	**Sex**	**Cause of Death**	**Length (cm)**	**Weight (Kg)**	**Class Age**
HS-2355	Maia	Female	maternal separation	79	11	Pup 0-1 month
HS-2372	Stalwart	Female	abscess	78	9.3	Pup 0-1 month
HS-2347	Myclovio	Female	prematurity	77	7.8	Pup 0-1 month
HS-2357	Dooby	Male	maternal separation	81	8.6	Pup 0-1 month
HS-2373	Golfball	Male	unknown	76	11.5	Pup 0-1 month
HS-2343	Rowdy Neal	Male	pneumonia (aspiration)	71	10.5	Pup 0-1 month
ES-3527	Vartha	Female	trauma	138	102	Weaner 1-12 months
ES-3531	Ares	Female	shark bite neoplasia obstruction	138	111	Weaner 1-12 months
ES-3546	Endara	Female	euthanasia malnutrition	120	31	Weaner 1-12 months
ES-3600	Muir	Male	unknown	137	42.5	Weaner 1-12 months
ES-3636	Ross Co	Male	otostrongyliasis	135	51	Weaner 1-12 months
ES-3645	Neemo	Male	unknown	120	30.5	Weaner 1-12 months

In designing the morphology study it was initially intended to include samples covering the whole demographic of both the harbor and elephant seal population. We were successful in obtaining both sexes for each species, but were limited to young seals, none reaching ages beyond 1 year. It is possible that further morphological distinctions could be observed in relationship to age and sex of the samples. It was deemed sufficient for this study to characterize the whiskers by species alone not seeking to extract further distinctions.

2.3.1 Mean Value and Standard Deviations

The whiskers measured can be summarized by the following chart displaying the mean and standard deviation of each parameters measured for the elephant and harbor seal whiskers. The values were calculated from the 27 whisker samples from these samples 120 peak locations and 119 trough locations are captures providing a grand total of 239 data points for characterizing the whisker geometry.

The parameters included in the following table are described as follows; angle of incidence at peak α, a major axis length at peak, b minor axis length at peak, M distance from peak to trough, angle of incidence at trough β, k major axis length at trough, l minor axis length at trough, Dm is the average of the of the four diameters defining the ellipse cross section at the peak and trough location defined by equation 2.4.

$$D_m = \frac{a+b+k+l}{2} \tag{2.4}$$

The average distance between peaks or troughs is defined by lambda, λ. Due to the complex geometry there are two wavelengths per feature, a distance between peaks on the leading edge of the whisker as well as the trailing edge. This is also true of the trough wavelengths, as such and due to their similar spacing the four values can be combined as a single parameter to define the spacing between features defined in equation 2.5.

$$\lambda = \frac{\lambda_{peakLE} + \lambda_{peakTE} + \lambda_{troughLE} + \lambda_{troughTE}}{4} \tag{2.5}$$

Hanke et al. defined M as the distance between adjacent peak and trough locations [29]. This measurement is equivalent to half of the average λ as defined in Eq. 2.6.

$$M = \frac{\lambda}{2} \tag{2.6}$$

Both species of whiskers studied displayed variations in their cross section profiles where the peaks exhibited more elliptical shapes in comparison the trough locations while still elliptical tended more towards circular cross sections. For this study the eccentricity, ϵ, will be the measure used to quantify the difference in cross sectional shape defined by equation 2.8. Where values of 1 signify a perfect parabolic shape and values of 0 signify a perfect circle.

$$\epsilon_{peak} = \sqrt{\frac{a^2 - b^2}{a^2}} \tag{2.7}$$

$$\epsilon_{trough} = \sqrt{\frac{k^2 - l^2}{k^2}} \tag{2.8}$$

The measured parameters were compared to previously reported values to ensure the measurement methods utilized produce accurate results. Ginter et al. provided the most exhaustive analysis of beaded seal whiskers available at the time [23]. Their analysis contained 92 whiskers spanning 11 different seal species. The only overlap in species between their study and this study was the harbor seal. A comparison between Ginter et al. and the results of this study are shown in table IV.

It can be seen that each measurement in common falls within one standard deviation of the other study providing confidence that the methods used in this study produce accurate measurements in agreement with results accepted within the field of expertise.

The whisker geometry summary table, Table IV, shows the length measurements for the whiskers tend to be consistent. However, the angles α and β vary

Table III: Whisker Morphology Summary

Harbor Seal	$\boldsymbol{\alpha}$ **(Deg)**	**a (mm)**	**b (mm)**	**M (mm)**	$\boldsymbol{\epsilon_{peak}}$	$\boldsymbol{\epsilon_{trough}}$
Mean	0.299	0.525	0.178	1.724	0.924	0.836
Std Dev	5.266	0.118	0.067	0.364	0.115	0.121
	$\boldsymbol{\beta}$ **(Deg)**	**k (mm)**	**l (mm)**	$\boldsymbol{D_m}$ **(mm)**	$\boldsymbol{\frac{\lambda}{D_m}}$	
Mean	1.218	0.416	0.219	0.664	5.257	
Std Dev	5.838	0.094	0.083	0.083	0.918	
Elephant Seal	$\boldsymbol{\alpha}$ **(Deg)**	**a (mm)**	**b (mm)**	**M (mm)**	$\boldsymbol{\epsilon_{peak}}$	$\boldsymbol{\epsilon_{trough}}$
Mean	-5.092	0.599	0.282	1.931	0.856	0.751
Std Dev	17.359	0.186	0.104	0.432	0.120	0.165
	$\boldsymbol{\beta}$ **(Deg)**	**k (mm)**	**l (mm)**	$\boldsymbol{D_m}$ **(mm)**	$\boldsymbol{\frac{\lambda}{D_m}}$	
Mean	-9.604	0.560	0.330	0.886	4.657	
Std Dev	21.049	0.224	0.132	0.275	1.115	

Table IV: Whisker Geometry Study Comparison

Harbor Seal	$\boldsymbol{\lambda_{Top}}$ **(mm)**	$\boldsymbol{\lambda_{Bottom}}$ **(mm)**	**2a (mm)**	**2k (mm)**	$\boldsymbol{\frac{a}{k}}$
Ginter et al. [23]	3.27 ± 0.39	3.26 ± 0.40	0.92 ± 0.13	0.73 ± 0.12	1.28
Rinehart	3.44 ± 0.72	3.45 ± 0.73	1.05 ± 0.24	0.83 ± 0.19	1.26

significantly and cannot be characterized by a mean value. The leading and trailing edge wavelength values show similar results as well. This corroborates with the results shown later that the angle of incidence α and β tend to be small in magnitude requiring that the difference in length between the leading and trailing edge be relatively small. The peak locations tend to have a more pronounced elliptical cross-section where the trough location features a slightly more circular cross-section. A study conducted by Lin et al. concluded that an optimal λ/D_m of 6.06 for reduction of lift and frag forces acting on the sinusoidal wavy cylinder [45]. The seal whiskers show similar values, the harbor seal within one standard deviation and the elephant seal within two standard deviations of the optimal value this suggests that there may be some natural optimization occurring in the whisker undulation sizing.

The length parameters are all represented well by mean values. This allows for an easy transition into experimental design, where whisker models can be constructed with the mean values observed in the whisker samples. This also provides confidence that it is reasonable to design an experiment that isolates the angle of incidence as the only design change, while ensuring the unique features of the seal whisker wake will not be compromised. Whisker models used for the flow experiment to be described in greater detail later will only vary along the length with respect to the angle of incidence. This will allow easier isolation of angle of incidence study noting that only varying the angle of incidence will still be an appropriate representation of the seal whisker. Also limited uncertainty and complexity is introduced by variations in the geometry outside of the parameter of interest, the angle of incidence.

2.3.2 Variations in Morphology as a Function of Length

This section will focus on depicting how key parameters vary along the length of the sample whiskers. Each whisker has a different length and the CT scans vary in the exact location captured on each whisker, although each scan focused on the mid section, as a results these data sets will be presented with length representing the distance from the first cross section scan captured for each whisker even though the zero location does not represent the same absolute distance from the root of the whisker. This will allow the different whiskers to be more readily compared.

Figure 15 shows how the major axis radii, a and k vary along the length of the whisker. Two representative whiskers are shown one harbor and one elephant seal to give the reader an understanding how these parameters vary with length. Four data sets are provided in Fig. 15 with color distinguishing the species of seal whisker, square symbols depicting peak data points and circles depicting trough data points.

It can be observed in Fig. 15 that both a and k decrease with increased distance

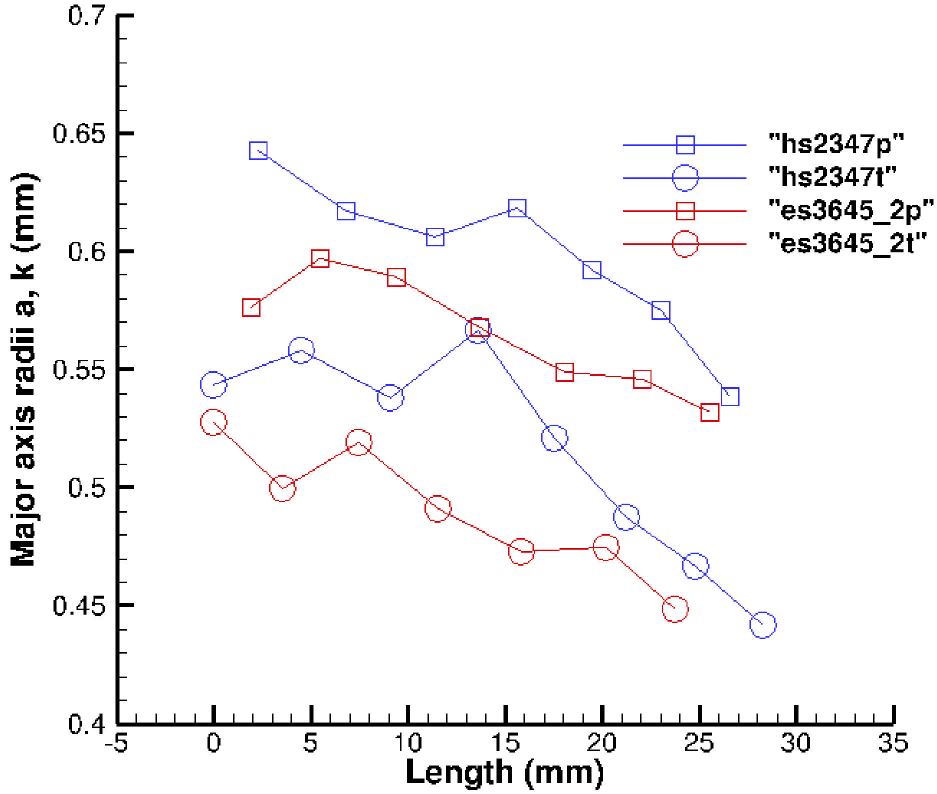

Figure 15: Major axis radii (a,k) as a function of length examples from harbor and elephant seal

from the root. There is consistent undulation along the length of the whiskers in the measured section observed by the distinct separation of a, squares, and k, circles.

Figure 16 shows how the minor axis radii, b and l, vary along the length of the whisker. The same representative whiskers shown in Fig. 15 are used again to give the reader an understanding how minor axis radii vary with length. Four data sets are provided in Fig. 16 with color distinguishing the species of seal whisker, square symbols depicting peak data points and circles depicting trough data points.

Figure 16 shows minor axis radii decrease with increased distance from the root of the whisker. This shows that overall there is a tapering of the whisker from root to tip due to reduction in major and minor radii. Similar to the major axis radii

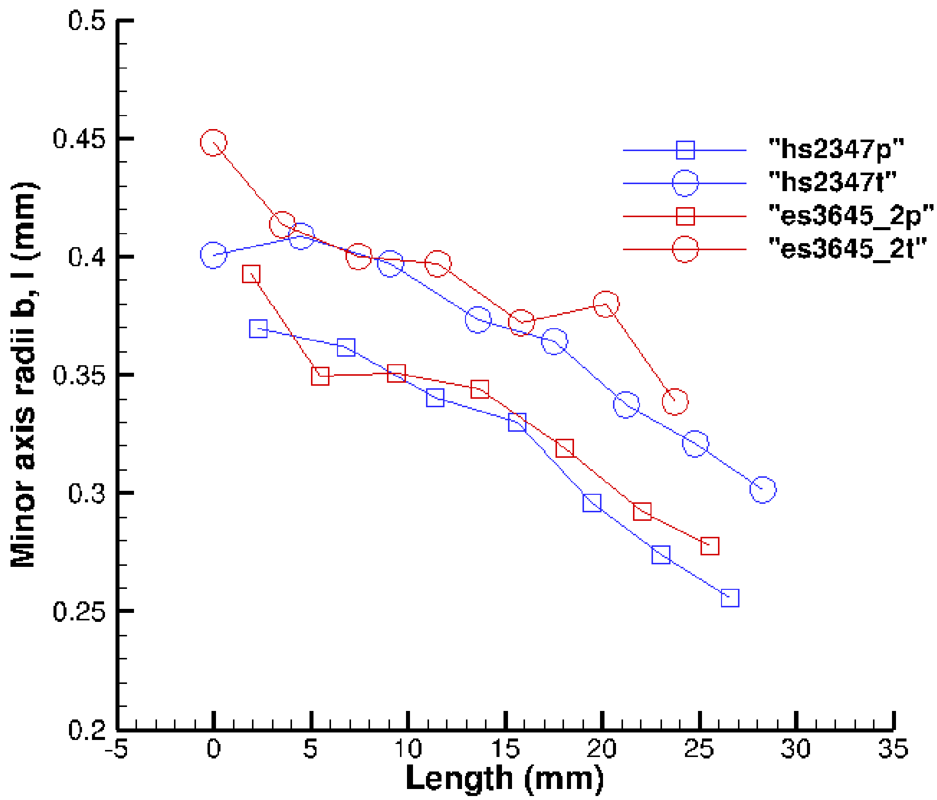

Figure 16: Minor axis radii (b,l) as a function of length examples from harbor and elephant seal

clear distinction is visible in between b and l data points. The undulation observed in the minor axis is less dramatic than that observed in the major axis with roughly 0.05 mm variation in the minor axis radii, b and l, and 0.1 mm variation in the major axis radii, a and k. Finally it can be noted from these variations of radii along the length that average values could be skewed depending on which section of the whisker is sampled, for this study all data resides in the mid section of the whiskers providing reasonable overall averages.

Figure 17 shows how eccentricity of the whisker varies as the distance from the root increases. The same two example whiskers are used here again. For both harbor and elephant seal whiskers the peak locations tend to be more parabolic and

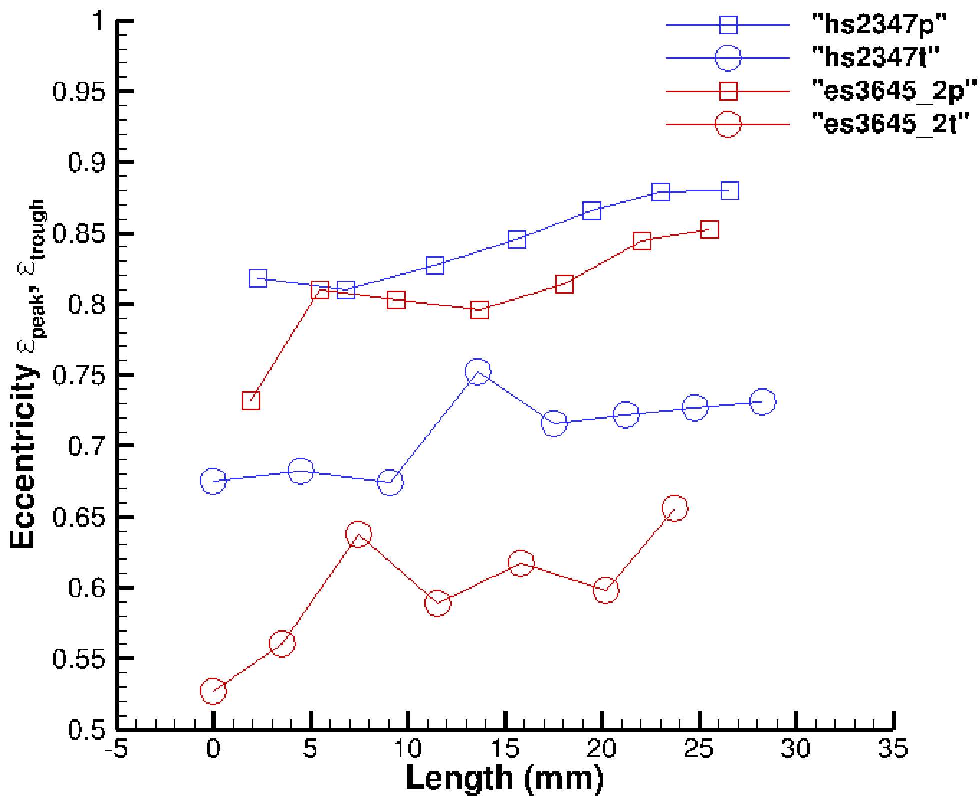

Figure 17: Eccentricty as a function of length examples from harbor and elephant seal

the trough locations are more circular. The elephant seal whiskers show slightly more circular cross sections when compared to the harbor seal. Both harbor and elephant seal whiskers show greater tendency towards parabolic cross sections as the distance from the root increases.

After establishing that the angle of incidence is not a consistent value across whisker samples or even along the length of an individual whisker in the previous section; we shift focus to answer two main questions; is there a typical magnitude of the angle and are there any distribution relationships? First we will look at how the angle of incident is distributed along the length of the whisker. The next sequence of plots will show the values of angle of incidence at the peak and trough locations along the length of the whisker.

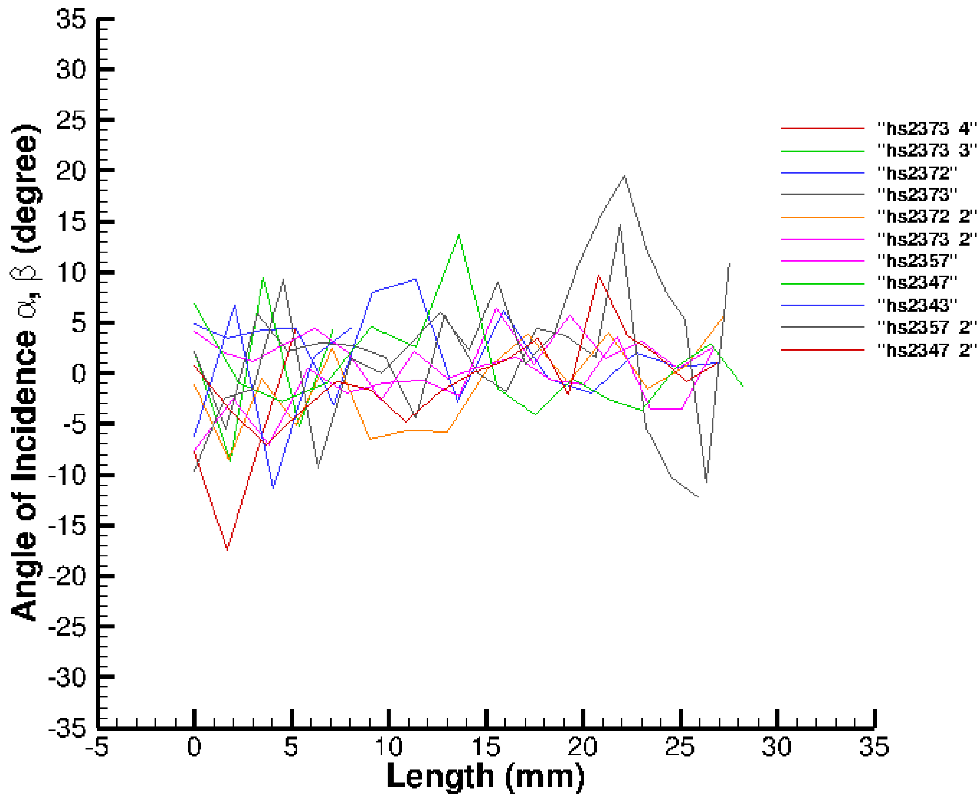

Figure 18: Harbor Seal Angle of Incidence as a Function of Length

Figure 18 shows the harbor seal angle of incidence, α and β, as a function of length. Twelve unique whiskers are presented in Fig. 18. It can be observed that both α and β show variation along the length of the whisker. None of the harbor seal whiskers observed show angle of incidences that are all positive or all negative. There does not appear to be any pattern in direction along the length either; some whiskers flip back and forth between positive and negative direction while others transition direction only once. No clear distinction can be observed between the α and β, nor does there appear to be a pattern that arises from alternating between peak and trough angle of incidence. Multiple whiskers from sample hs2373, hs2347, hs2357, and hs2372 are presented in the data set. Comparing these samples show no pattern or trend among whiskers from the same seal. The only strongly observable feature is that both α and β remain within 20° magnitude centering around 0°.

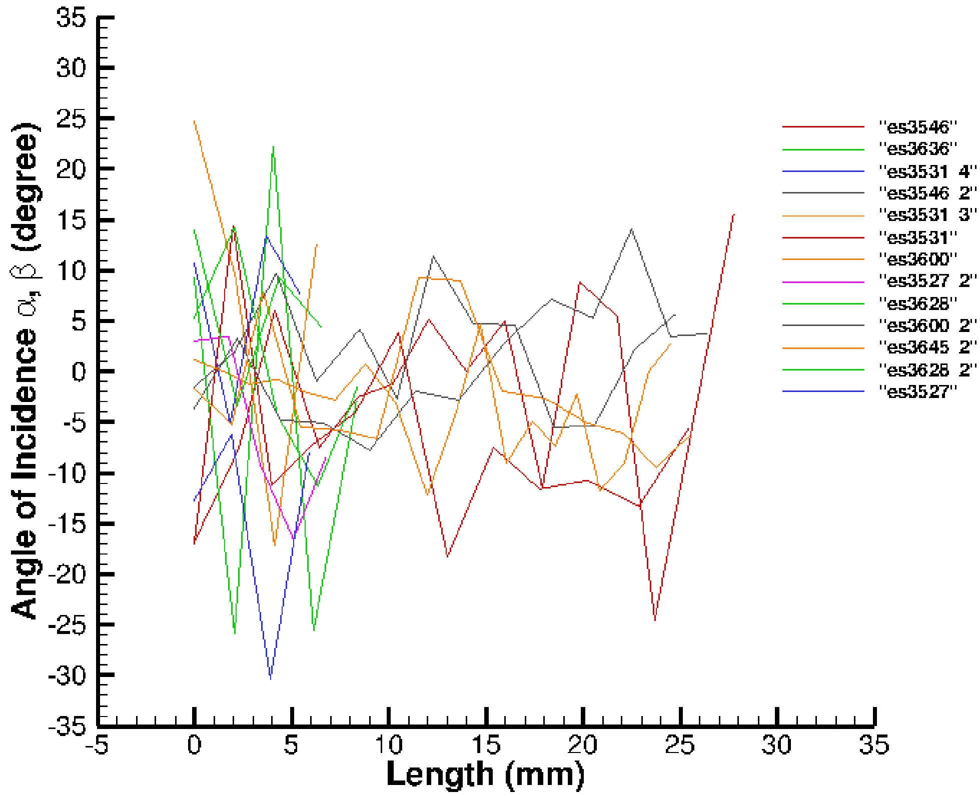

Figure 19: Elephant Seal Angle of Incidence as a Function of Length

Thirteen elephant seal whiskers shown in Fig. 19 exhibit similar characteristics to the harbor seal. Slightly larger extreme angle of incidence values, 30°, are observed in the elephant seal which may be due to the overall larger size of the elephant seal whisker. Again most whiskers show both positive and negative values for the angle of incidence. There does not appear to be any observable trends from whiskers taken from the same seal. Similar to the harbor seal no strong relationship between angle of incidence and distance from the root are evident from this analysis.

These angle of incidence results obtained within this study show strong agreement with those found in Murphy's 2013 work shown in Fig. 20 and 21 [51].

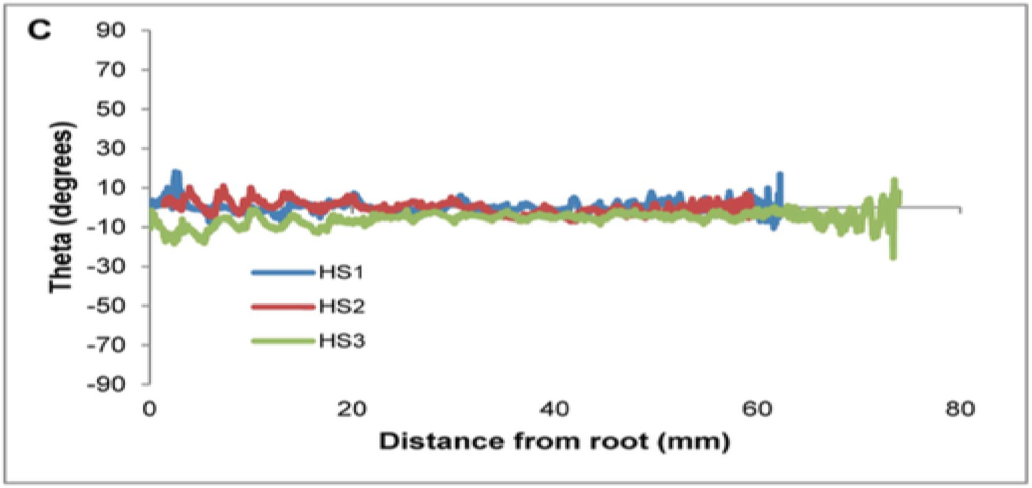

Figure 20: Harbor Seal Angle of Incidence as a Function of Length Murphy [51]

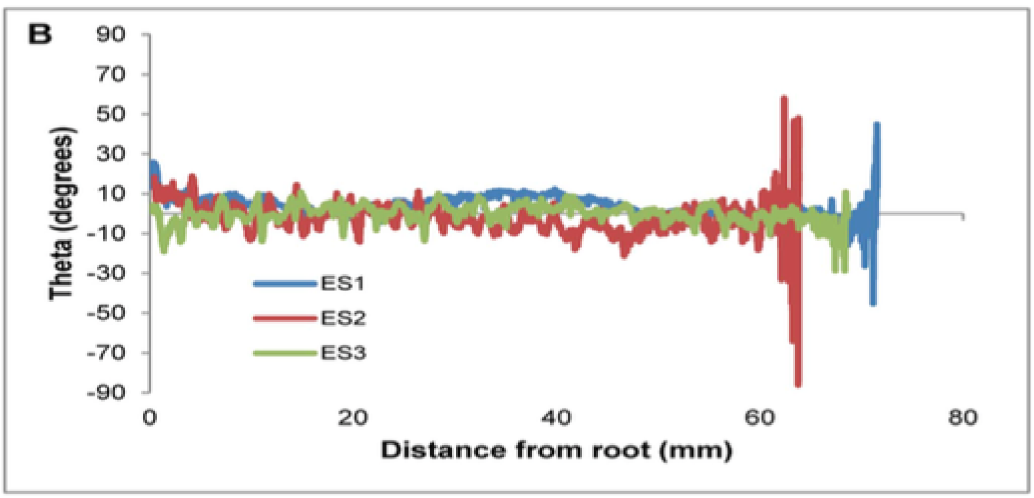

Figure 21: Elephant Seal Angle of Incidence as a Function of Length Murphy [51]

A brief comparison shows that both the harbor and elephant seal angle of incidence magnitudes center around zero degrees. The elephant seal whiskers show slightly larger deviations from a zero degree angle of incidence. There does not appear to be a relationship with distance from the root to angle of incidence observed within Murphy's data set which was also confirmed within this study. The strong agreement of these results provides added confidence in the individual findings as well as validates a broader claim that these characterizations of angle of incidence are repeatable and not unique to either sample set of whiskers analyzed.

One area to note for this study is that two elephant seal whiskers exhibited abnormal morphology features when compared to the rest of the sample set. These two whiskers deviated from the pattern of the leading and trailing edges undulating in unison away from the center line and then towards the center line. The two whiskers in question instead near the root of the whisker exhibited a pattern where the leading and trailing edges would move in the same direction. This resulted in the the leading edge moving away from the center line while the trailing edge moved toward the center line. As a result of this abnormal behavior the angle of incidence measured in this region showed large magnitudes in excess of 60° for some cases. Below is a reconstruction of the CT scanned files for one of the whiskers described above; it can be observed that on the far right side of figure 22a the abnormal feature is visible and returns to more typical undulations towards the left side of the figure. Due to the inconsistencies observed in these whiskers they were excluded from the results. Another whisker showing typical undulation behavior is provided for comparison in figure 22b.

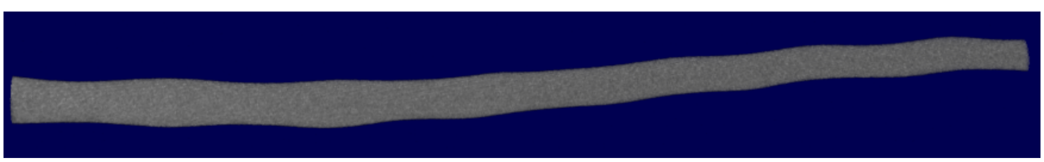

(a) Abnormal elephant Seal Whisker Undulation

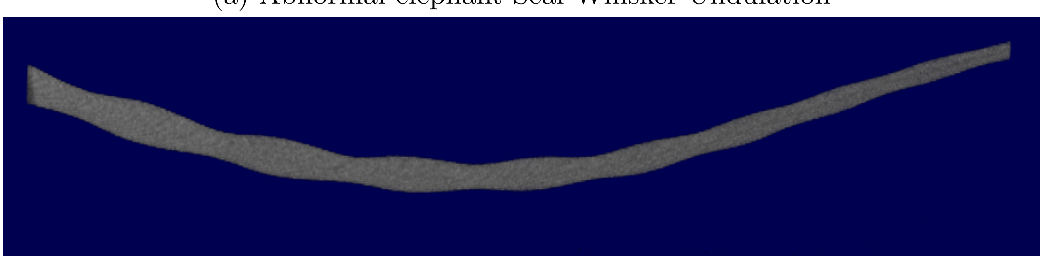

(b) Typical harbor Seal Whisker Undulation

Figure 22: Comparison of Abnormal to Typical Undulation

These instances of abnormal undulation patterns have been treated as outliers and not representative of a typical whisker. It is interesting to note that this feature was only observed with the elephant seal and were whiskers from two different seals. Unfortunately the overall sample size does not allow for generalized conclusions to be made about this interesting anomaly.

2.3.3 Angle of Incidence Frequency of Occurrence

To evaluate the other question regarding the angle of incident it is more appropriate to analyze how often different angle of incidence occur within the sample set. Below are the results of grouping angle of incidence into 5° increments and analyzing the frequency of their occurrence.

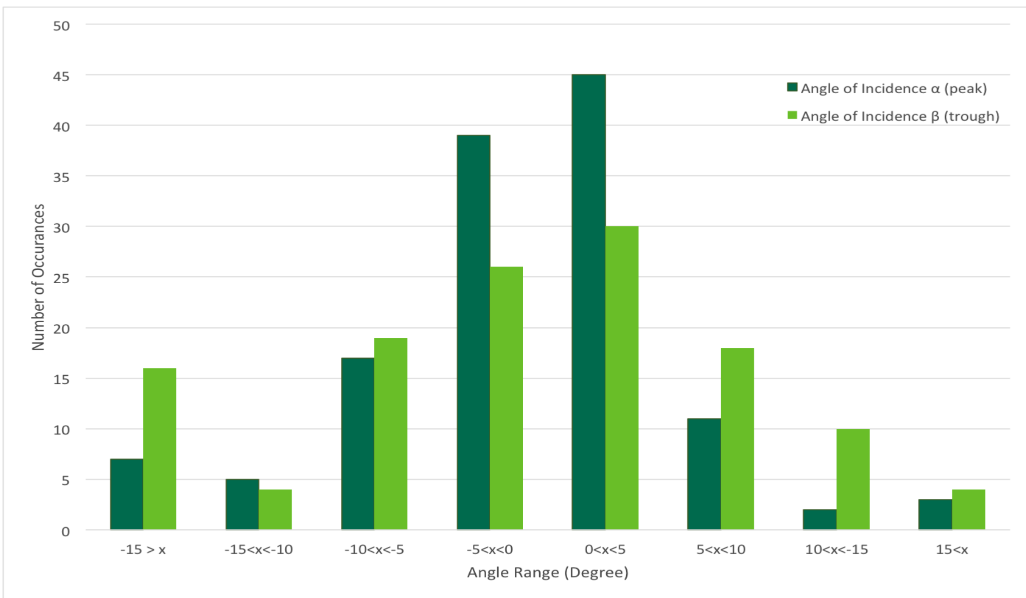

Figure 23: Angle of Incidence Frequency of Occurrence

Here it becomes more obvious that the predominate trend among the whiskers is that the magnitude of the angle of incidence found in nature is small with the bulk of the samples falling within $-5°$ and $5°$. This is of particular interest in comparing to previous studies where representative whisker models had angle of incidence around $15°$ [5, 29]. A summary of other flow studies investigating the undulating seal whisker geometry are provided here for comparison.

Table V: Previous Whisker Flow Study Angle of Incidence

Study	α	β
Hanke et al. [29]	15.27°	17.60°
Wang et al. [70]	15.27°	17.60°
Beem [5]	15.27°	17.60°
Hans et al. [32]	0° 17.6° 15.27°	0° 17.60° 17.60°
Shyam et al. [65]	5°	5°

One thing that should jump out from this summary of previous studies is the limited focus given to the angle of incidence. It appears that some of the initial work conducted by Hanke et al. has had a strong influence on experimental design choices carried out in the follow on studies. Hans et al. study provided the most depth of study with three different combinations of angle of incidence evaluated. Even those three choices seem to be based more on previous work than a systematic study of various magnitude and orientations of angle of incidence. The findings of this study show that while the angles used in other studies do fall in the range of observed natural tendencies they are on the extreme edges of this sample set. This suggests that results found in previous work may not accurately characterization of the wake features produced by seal whiskers. Since research has not been conducted with a range of angle of incidence studied it cannot be know at this point if having an angle of incidence on the larger end of the spectrum enhances the effect it has on the wake structure or detracts from the angle of incidence effect. The flow section of this research will set out to clarify the relationship of the angle of incidence to the wake structure.

2.4 Conclusions

This morphology characterization study has shown that of the seven parameters used to describe the seal whisker shape, five can be accurately described by the mean value of the sample whiskers investigated. These parameters are the major and minor axis lengths located at the peak and trough, a,b,l, and k as well as then distance between peak and trough, M. This shows that these values remain consistent along in the middle section of the whisker as well as between different whiskers of the same species. The remaining two parameters, α and β could not be characterized by their mean values due to the random variation in direction and magnitude observed along the length of each whisker. These variations in magnitude and direction could not be correlated to distance from the root of the whisker either. The angle of incidence were able to be understood in terms of the frequency in which different magnitudes occurred within the sample set. Here it was found that the majority of the whiskers fall between $-5°$ and $5°$ angle of incidence. As noted in the introduction interest in applying the geometry of the beaded seal whiskers to various designs to improve performance could utilize the relationships observed in this study as a baseline for design practices. The results found here will inform the rest of this study. The mean values for the length parameters will be used to design a scaled up model of the seal whisker where various angle of incidence will be applied to different models allowing the angle of incidence affect on the wake structure to be studied.

CHAPTER III

Wake Dynamics

3.1 Introduction

The study of the beaded seal whisker wake structure was inspired by observing the the seal whisker's unique shape and speculation that this shape contributed to it's ability to hunt prey under low visibility conditions. Research has concluded that the undulating surface of the whisker helps to suppress vortex induced vibrations [29]. Previous studies have investigated the how the undulations in the major and minor axis contribute to this phenomena; however, have not investigate how various angle of incidence observed in nature contribute to the reduction of vortex-induced vibration and overall wake structure [32]. The following section will address this knowledge gap through the use of particle image velocimetry measurements taken downstream of 3D printed seal whisker models possessing various angles of incidence. The remained of this chapter will be organized as follows; an explanation of the experimental design and setup, a presentation of the measured results, followed by a discussion of the experimental results.

3.2 Experimental Setup

3.2.1 Scaled-up Whisker Models

The influence the angle of incidence has on the wake structure is not well understood. To address this knowledge gap an in depth study of the whisker geometry was conducted in the previous chapter. The results of morphology study supplied the parameters to define and construct representative whisker models. The following flow study will focus on the harbor seal geometry. The mean values found in the morphology study were used to define the values for major and minor axis at the peak location, a and b, the major and minor axis at the trough location, k and l, and the distance between the peak and trough M. These values were scaled up approximately 8 times the size of real harbor seal whiskers to maximize the number of undulations within the water channel test section while remaining within the resolution of the 3D printer. Four models were constructed defined by Tab. VI.

Table VI: Whisker Model Angle of Incidence

Model	α	β
Model A	$0°$	$0°$
Model B	$5°$	$-5°$
Model C	$-15°$	$-15°$
Model D	$-5°$	$-5°$

The models were designed with the selected angle of incidence based on the results of the morphology study. Model A was selected to serve as the baseline. Models C was selected based on the observation that the vast majority of the angle of incidence observed in this sample of whiskers falls within $\pm 5°$. Model D was selected to define the extreme edges of the angles observed. Finally model B was selected with the hypothesis that if the angle of incidence can influence the wake structure an alternation of direction along the whisker length could expect the most significant deviation from the baseline model A.

These models were generated using SolidWorks tool. Elliptical cross-sections were created on planes that provided the proper angle of incidence to the centerline of the model and were spaced to maintain the correct half wavelength defining the distance between the peak and trough locations observed in the whisker morphology study. The loft feature was applied to the different cross-sections to create the three dimensional whisker models.

Table VII: Whisker Model Geometry

	a (mm)	b (mm)	l (mm)	k (mm)	M (mm)	λ/Dm	# undulation
Whisker Model Parameters	7.73	2.62	6.20	2.92	12.70	5.22	4.5

Provided in Tab. VII is the parameter D_m. Research involving seal whiskers-like geometry and wavy cylinders have used the parameters D_m and hydrodynamic diameter, D_h, for nondimensionalization. has coalesced around this parameter for nondimensonalization in visualization of results and providing the length scale for Re [73].

An example of one of the SolidWorks files used to design the whisker model is provided in figure 24. This model is for the $\alpha = 5°$ and $\beta = -5°$. One peak and one trough cross section have been highlighted and annotated for reference.

Whisker models were printed using the Stratasys uPrintSE Plus 3D printer located at the Cleveland State University Additive Manufacturing Lab [67]. The models begin to lose some of the precision near the end of the model due to orientation required for printing. The ends of the models where the surface begins to degrade were trimmed and not exposed to the flow and therefore did not influence the flow study. The whisker models were then painted with a black flat matte paint to limit reflections from the laser that might corrupt the illumination of particles near the whisker model. This corruption occurs through a processed called "blooming" where

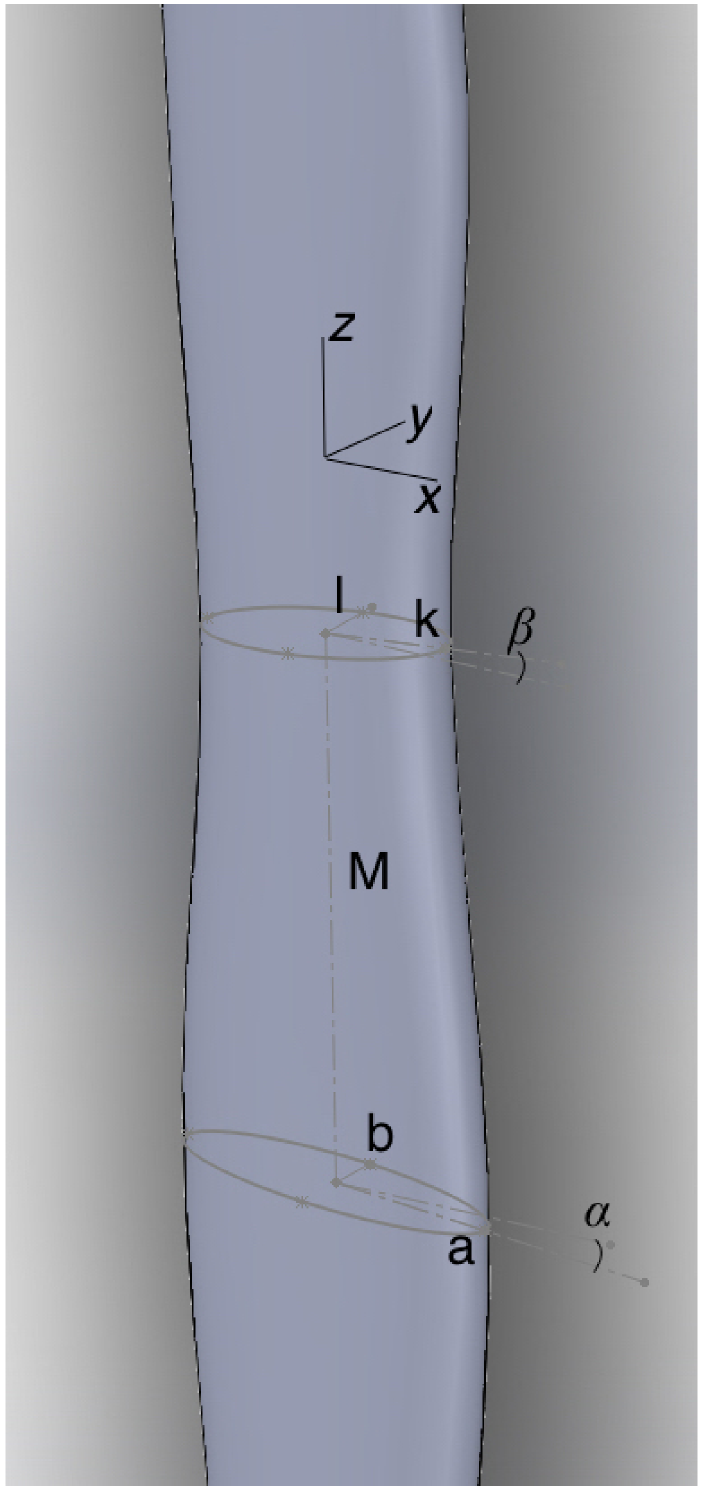

Figure 24: CAD whisker model showing construction dimensions at representative peak and trough cross sectional planes

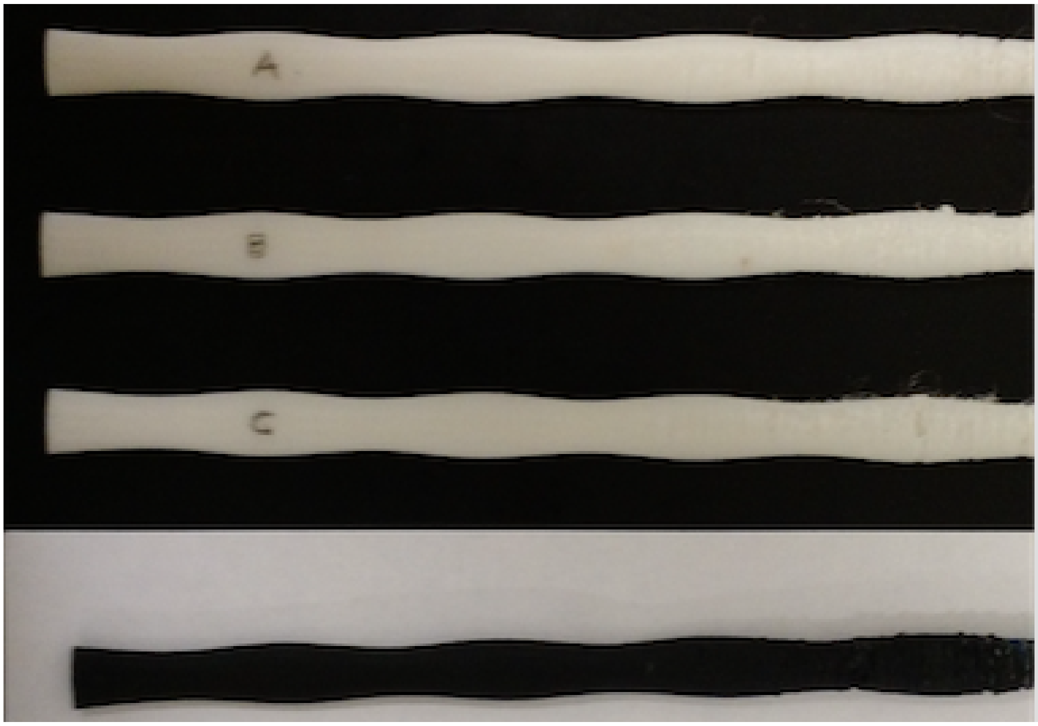

Figure 25: 3D printed whisker models produced with Stratasys uPrintSE Plus 3D printer. Three models shown before application of matte black paint and one after application.

the light reflecting off the model can over expose certain areas of the image making identification of individual particles impossible and producing dead spots within the image where velocity vectors can not be calculated.

3.2.2 Water Channel Facility

A water channel provided the flow environment used to study the wake structure created by the seal whisker models. The water channel is constructed with plexiglass sheet. The water channel consists of a stacked flow path were water is pumped into the upper channel containing the test section and returns to the reservoir by a return path immediately underneath the test section flowing in the opposite direction. The test section for the water channel consisted of a $0.14\,\mathrm{m} \times 0.20\,\mathrm{m} \times 0.61\,\mathrm{m}$ volume. The water channel used a constant speed pump that generated a mean flow of $0.1\,\frac{\mathrm{m}}{\mathrm{s}}$.

The flow was conditioned by six honeycomb flow conditioning devices upstream of the test section visible in Fig. 27. The water channel is characterized by a turbulence intensity of 4 %. The flow can also be characterized by the non-dimensional quantity, Reynolds number, a ratio of the viscous forces and inertial forces acting on the fluid. Reynolds number is defined in Eq. 3.1. For this research the characteristic length term is D_m. The water channel has a Reynolds number of 630.

$$Re = \frac{U_o D_m}{\nu} \tag{3.1}$$

The Characterization of the water channel was conducted through PIV at the three measurement planes where whisker model flow data was captured. The following figures will characterize the mean velocity fields as well as the mean turbulence statistics for the three measurement planes.

Figure 26 the two normalized velocity fields with their corresponding turbulence intensity fields. Figure 26 shows that in the vertical plane the the flow is well conditioned with the bulk of the u velocity within 2% of the free stream velocity. The w velocity is relatively low as well showing less than a percent of the free stream velocity. The turbulence characteristics generally fall within 3-5% T_u and less than 3% for T_w. The streaks of high intensity are the results of these measurements taken at the early stages of the experiment process. While the test was running bubble would accumulate on the top panel of the water channel and slowly migrate. The result of the bubbles caused some inaccurate measurements. A procedure for bubble checking and remove was implemented for later test cases to minimize the corruption of data.

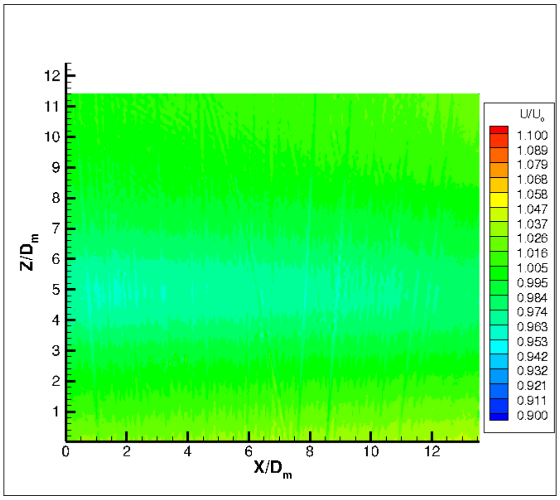

(a) Mean u/U_o Velocity Field

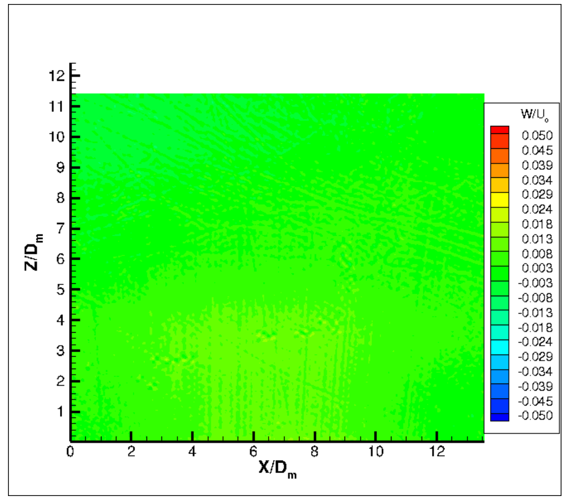

(b) Mean w/U_o Velocity Field

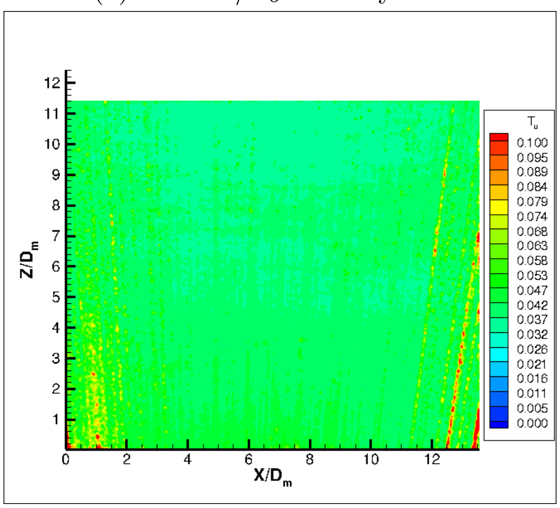

(c) Mean T_u Field

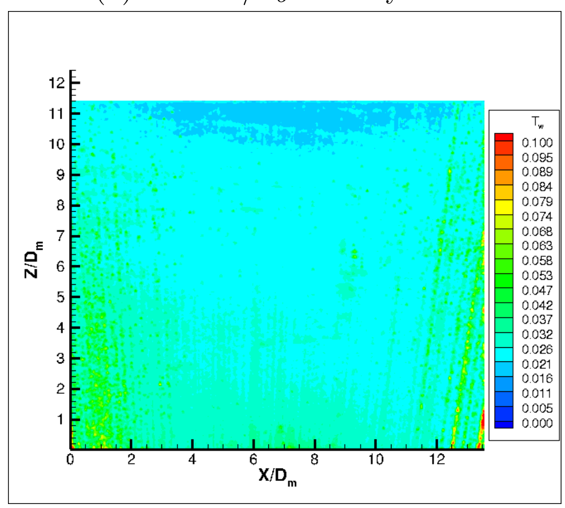

(d) T_w Field

Figure 26: Water channel flow characterization: velocity and turbulence fields in the vertical centerline plane (x-z)

3.2.3 Particle Image Velocimetry Measurement

Particle image velocimetry is a non-intrusive measurement technique for measuring flow conditions. The task is performed by seeding the flow being studied with particles of consistent size. These particles are then illuminated with laser light that has been constructed at a specific wavelength. The laser is pulsed twice in a short amount of time, *dt*. A camera that is fitted with a wavelength bandwidth filter specified to only capture the light from the laser captures two images timed with the laser

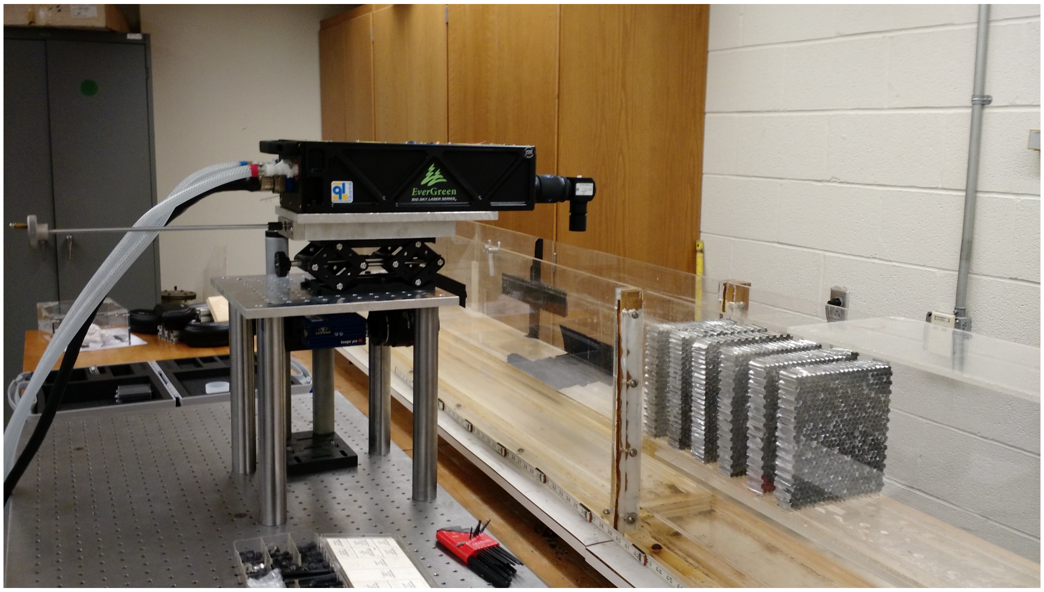

Figure 27: Experimental setup at CSU water channel displaying vertical measurement plane setup: honeycomb flow conditioners, ND:Yag laser, and CCD camera

pulses. The illuminated particles in each image are used in conjunction with dt and the pixel's physical size to compute a velocity field. There are numerous variations to PIV setups the one used in this research is a simple two dimensional two component setup. This means that a single camera captures a two dimensional image and from those two dimensional images two velocity components can be resolved. The PIV system is comprised of the following components. The laser is an Evergreen Dual-Pulsed neodymium-doped yttrium aluminum garnet (ND:Yag) laser with 14.7 Hz. The light output is characterized by 532 nm wavelength and 600 mJ energy output. The camera used is a Pro-Imager SX CCD 5 MP camera fitted with a Nikkon 60 mm lens and a 532 ± 5nm wavelength filter. The water was seeded with glass spheres from LaVision these spheres have an average of diameter of 10 µm. The camera and laser were controlled with the LaVision DaVis software package version 8.2, this software was also used to process the captured image pairs.

The laser and camera are mounted on the adjustable platform. The laser is mounted on the top section of the platform with optic extending over the water channel and positioning the laser to direct the light sheet down the center line of the water channel. The camera is mounted below the laser between the platform legs.

The 3D printed whisker models were mounted in the center of the water channel test section and aligned to have zero angle of attack with respect to the incoming flow. Images were captured for three setups for each whisker model including; a vertical plane along the centerline of the whisker, a cross-sectional plane located at the peak of the whisker model and a cross-sectional plane located at the trough of the whisker model. These different measurement planes are depicted in Fig. 28. Measurements of the highly three dimensional flow would ideally be captured with a tomographic PIV system allowing all three velocity components to be captured simultaneously in a volume behind the whisker models. For this research that measurement technique was not available; therefore these measurement planes were selected to capture all three velocity components with the two dimensional two component PIV setup and provide a representative measurements at critical locations.

For each test case 2000 image pairs were captured. These images were processed with the DaVis software. A multi size interrogation window scheme was used starting with a two pass $32\,\mathrm{pix} \times 32\,\mathrm{pix}$ with $50\,\%$ overlap this was followed by another two pass window interrogation size of $16\,\mathrm{pix} \times 16\,\mathrm{pix}$ with $50\,\%$ overlap. The images were also post processed with a filter that removed windows with less than 5 vectors and a single pass filter that removed and replaced vectors that exceeded 2 standard deviation from neighbors threshold. Once the image pairs were processed a custom Matlab script calculated the ensemble average of each test case. The results of the ensemble averaging will be reported in the following sections.

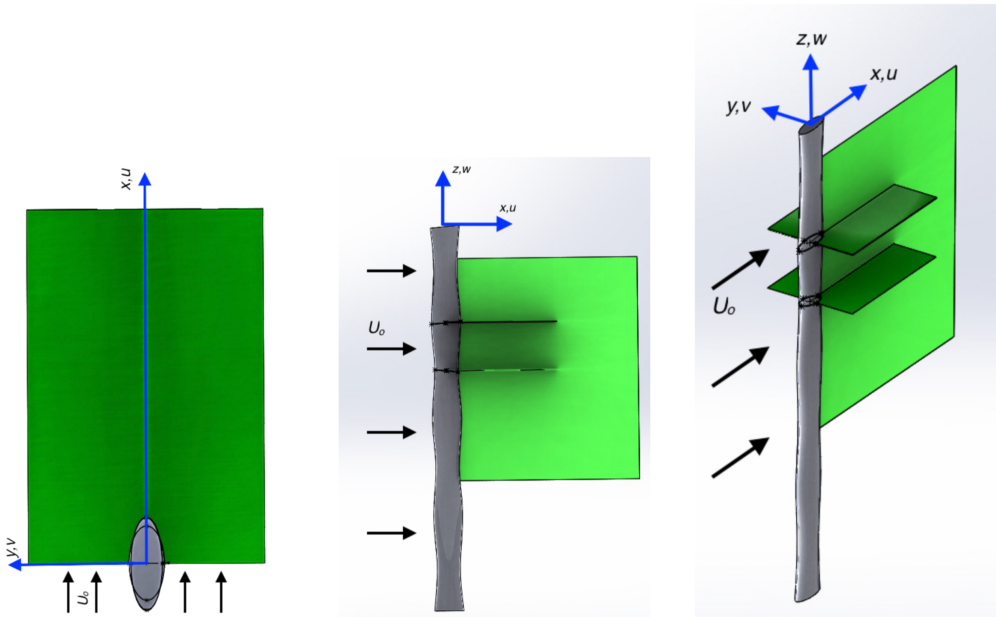

(a) Horizontal measurement plane (b) Vertical measurement plane (c) vertical measurement plane

Figure 28: PIV measurement plane schematics showing vertical, peak and trough measurement planes and coordinate system

3.2.4 Ensemble Averaging

The wake dynamics of the whisker models are highly unsteady, but with a sufficiently large sample of instantaneous velocity data sets an average value can be obtained this is the premise of the PIV measurement technique. Each pair of images obtained yields an instantaneous velocity field. Furthermore velocity fields calculated from the image pairs are considered statistically random due to the low sample rate of the image pair acquisition. From these random samplings statistical analysis can be performed on the dataset. Reynolds ensemble averaging is a statistical method for obtaining steady state flow properties at discrete points in a velocity field. Equations 3.2-3.2 define the ensemble average velocity component equations. Where $u_i(x, y, z)$, $v_i(x, y, z)$, $w_i(x, y, z)$ are instantaneous velocity components at a specific spatial locations.

$$\overline{u}(x,y,z) = \frac{1}{N}\sum_{1}^{N} u_i(x,y,z) \tag{3.2}$$

$$\overline{v}(x,y,z) = \frac{1}{N}\sum_{1}^{N} v_i(x,y,z) \tag{3.3}$$

$$\overline{w}(x,y,z) = \frac{1}{N}\sum_{1}^{N} w_i(x,y,z) \tag{3.4}$$

Velocity components are not directly measured in the PIV analysis; instead particle displacements must be transformed into velocities through knowledge of the pixel to real world scale and the time step, dt, between laser pulses. These ensemble averaged velocity components will be presented in the results normalized by the free stream velocity.

In addition to obtaining the Reynolds average velocity components further work can be done to extract the turbulence statistics. This is accomplished through the Reynolds decomposition method. Here fluctuations from the mean velocity value are calculated for each instantaneous velocity field as defined by Eqs. 3.5-3.7.

$$u_i^{'}(x,y,z) = u_i(x,y,z) - \overline{u_i}(x,y,z) \tag{3.5}$$

$$v_i^{'}(x,y,z) = v_i(x,y,z) - \overline{v_i}(x,y,z) \tag{3.6}$$

$$w_i^{'}(x,y,z) = w_i(x,y,z) - \overline{w_i}(x,y,z) \tag{3.7}$$

After the instantaneous velocity field fluctuations have been calculated the root-mean-square of the fluctuations is calculated through Eqs. 3.8-3.10.

$$u_{rms}(x,y,z) = \sqrt{\frac{1}{N}\sum_{1}^{N}(u_i'(x,y,z))^2} \tag{3.8}$$

$$v_{rms}(x,y,z) = \sqrt{\frac{1}{N}\sum_{1}^{N}(v_i'(x,y,z))^2} \tag{3.9}$$

$$w_{rms}(x,y,z) = \sqrt{\frac{1}{N}\sum_{1}^{N}(w_i'(x,y,z))^2} \tag{3.10}$$

Defining how steady or unsteady the flow is often characterized by turbulence intensity. Turbulence intensity is a single velocity component quantification of how much the flow fluctuations with respect to the free stream flow conditions. This is accomplished by taking the root mean square of the velocity component and dividing by the free stream velocity as seen in Eqs. 3.11- 3.13.

$$T_u = \frac{u_{rms}}{U_o} \tag{3.11}$$

$$T_v = \frac{v_{rms}}{U_o} \tag{3.12}$$

$$T_w = \frac{w_{rms}}{U_o} \tag{3.13}$$

Reynolds shear stress is another valuable measurement that can be obtained trough Reynolds decomposition. Reynolds shear stress provides a measure of the transport of momentum due to the velocity fluctuations. Here for a given plane the two measured instantaneous velocity fluctuations are multiplied and time averaged as defined in Eq. 3.14 and 3.15. The density term has been assumed constant and neglected for normalization purposes.

$$\tau_{xy}'' = -\overline{u_i'(x,y,z)v_i'(x,y,z)} \tag{3.14}$$

$$\tau_{xz}'' = -\overline{u_i'(x,y,z)w_i'(x,y,z)} \tag{3.15}$$

The final flow quantity used to characterize the wake structure in this study is vorticity, an evaluation of how much rotation is present within the flow. Vorticity is defined as the curl of the velocity field defined by Eq. 3.16 and 3.17. For our experiments only two velocity components are captured for each measurement plane the out of plane velocity component is treated as zero.

$$\omega_y = (\frac{\partial}{\partial x}, \frac{\partial}{\partial y}, \frac{\partial}{\partial z}) \times (u, 0, w) \tag{3.16}$$

$$\omega_z = (\frac{\partial}{\partial x}, \frac{\partial}{\partial y}, \frac{\partial}{\partial z}) \times (u, y, 0) \tag{3.17}$$

3.2.5 Convergence and Uncertainty

The results that will be presented in subsequent sections are the ensemble average of the 2000 image pairs collected during each test case. These results will be presented as averages it is important for the results to converge. Convergence was assessed for each test case by averaging limited ranges of the total set of velocity fields and observing how the ensemble average changed with increases data set size.

Figure 29 shows the maximum absolute value change in the velocity field between different numbers of image pairs used for ensemble averaging normalized with the free stream velocity as defined in Eq. 3.18. Where the same ensemble average format as Eq. 3.2 is used but j is the number of image pairs used for the ensemble averaging.

$$\Delta\overline{u}_{max} = |\frac{1}{j+1}\sum_{1}^{j+1} u_i(x, y, z) - \frac{1}{j}\sum_{1}^{j} u_i(x, y, z)| \tag{3.18}$$

It should be noted that Fig. 29 shows data for all three velocity components while the *y-axis* is labeled as $\Delta\overline{u}_{max}/U_o$ where u is understood to be a generic velocity component so that the axis is not cluttered. Figure 29 shows data from two different

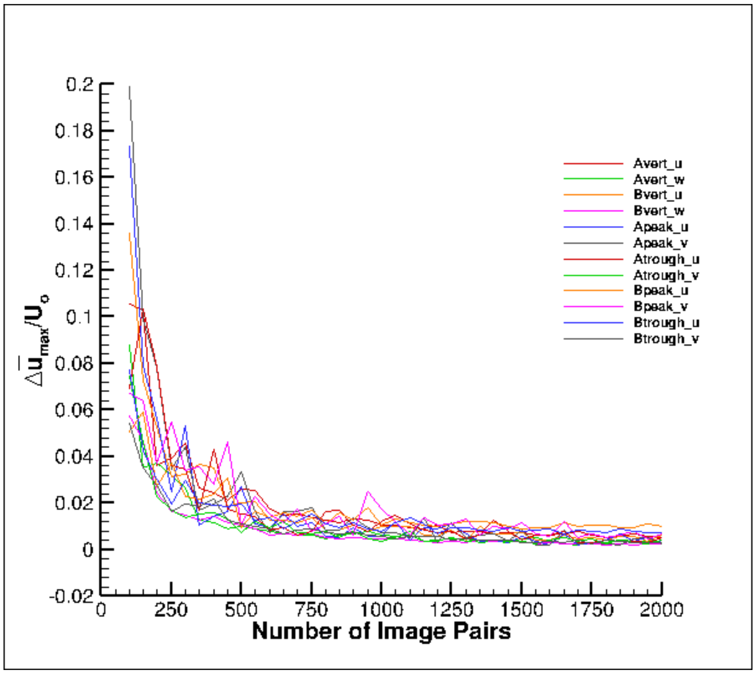

Figure 29: Convergence of ensemble averaged velocity fields in vertical centerline, peak and trough measurement planes

whisker models at all three measurement planes to ensure convergence is obtained for all test cases.

It can clearly be observed in 29 that all velocity components in all three measurement planes converge well before the full complement of 2000 image pairs are used. Most of the data converges once 700 image pairs are used for the ensemble averaging. This yields strong confidence that the ensemble averaged velocity fields presented in the following section do accurately represent the mean value of the velocity field.

A similar method is used to check the convergence of the turbulence statistics. The maximum change in the root-mean-square of the velocity fluctuations is tracked as the number of image pairs used for the ensemble averaging is increased. The change in the maximum root-mean-square value is defined in Eq. 3.19.

$$\Delta u_{rms,max} = \left|\frac{1}{j+1}\sum_{1}^{j+1} u_i'(x,y,z) - \frac{1}{j}\sum_{1}^{j} u_i'(x,y,z)\right| \tag{3.19}$$

Again the *y-axis* in Fig. 30 is defined by $\Delta u_{rms,max}/U_o$ where u is understood

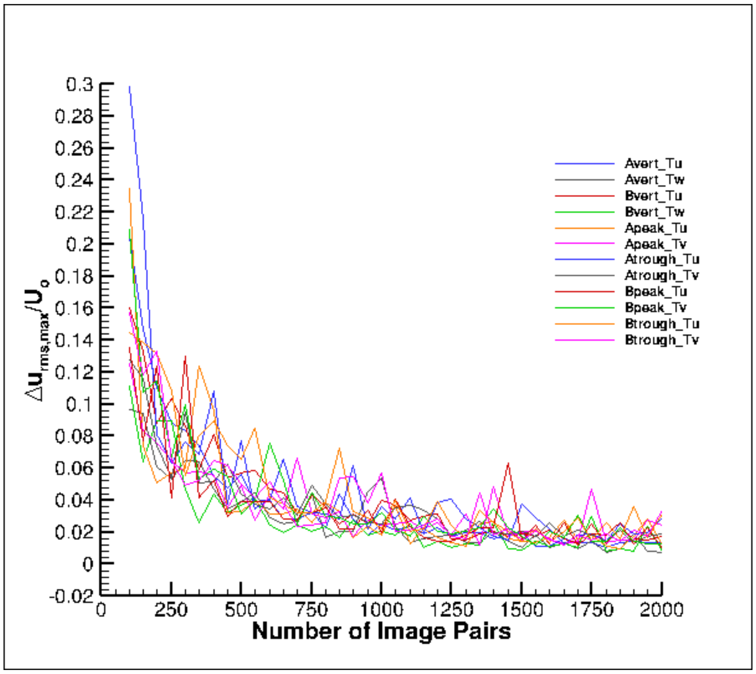

Figure 30: Convergence of ensemble averaged root-mean-square velocity fields in the vertical centerline, peak and trough measurement planes

to be a generic velocity component. Figure 30 shows that for turbulence statistics more image pairs are required for convergence. Here most of the data converges once 1250 image pairs are used for the ensemble averaging process.

The uncertainty of the measurement process should be evaluated in addition ensuring convergence of the data. Quantifying the uncertainty associated with PIV is a young field and many new methods and ideas are currently being presented each with unique advantages and disadvantages. Several methods have been suggested for measurement error evaluation. One method called 'uncertainty surface' compares; particle image size, particle density, displacements and shear for each image pair. Another method utilizes the two highest peak correlation values to define uncertainty. The main principle used to quantify this error in any method relies on maximizing the correlation between the image pairs through the intensities of the images. Error levels within PIV have been reliably bounded between 0.02px to 0.3px [72]. The measurement errors rarely drop below 0.02px due to the stack up of source errors. If errors exceed 0.3px there is strong indication that a more fundamental setup error is present within the experiment. The results of the experiments in this research fall within this range of uncertainty.

3.3 Results

The results will be presented for three representative planes: a vertical plane and two cross-sectional planes one at the peak and one at the trough for each of the models similar to Wang and Liu [70]. Results of the measured flow structures will be presented as mean velocity fields, vorticity, as well as turbulence characteristics of the wake. Model A will serve as the baseline case for the following results and analysis. As seen in the morphology chapter most whiskers found in nature contain angle of incidence that reside near 0°. The deviations from the 0° observed in each of the remaining models will inform how the angle of incidence influences the wake structure. The schematic 28 defines the orientation of the models for each test case as well as the axis labeling that will be used to present the results.

3.3.1 Vertical Centerline Plane

This subsection will characterize the flow properties along the centerline of the whisker model parallel to the *x-axis*. Results will be presented in composite figures with the results for a particular quantity displayed for all four models. The models will appear within the composite figure in the following order starting in the top left and moving clockwise; Model A ($\alpha = 0°$, $\beta = 0°$), Model B ($\alpha = 5°$, $\beta = -5°$), Model C ($\alpha = -15°$, $\beta = -15°$), Model D ($\alpha = -5°$, $\beta = -5°$). General observations about each model will be provided with a more detailed comparison between the models provided in the conclusion section.

Figure 31 displays the mean u velocity field normalized with the free stream velocity. The flow is moving from the left of the figure to the right. Half of the whisker model is in frame indicated by the black object on the left most edge. In addition black lines have been overlaid to indicate peak and trough locations extended further downstream from the model based on the angle of incidence to aid in comparisons between the different models. In addition to the color contour of normalized u velocity a dashed line is provided to indicate the recovery length, r, and a 'dashed-dot-dot' line indicates the edge of the reversed flow region of $u = 0$.

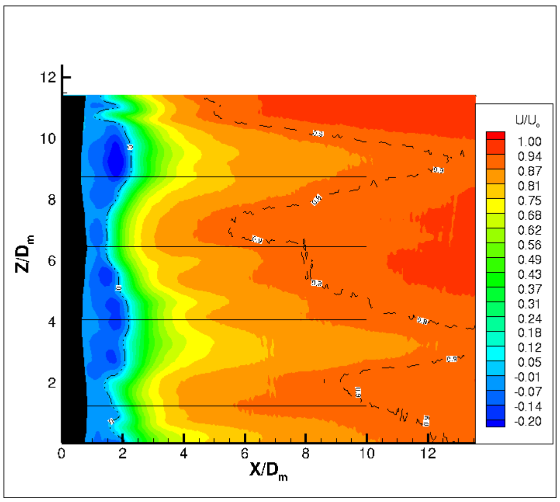

(a) Model A ($\alpha = 0°$, $\beta = 0°$)

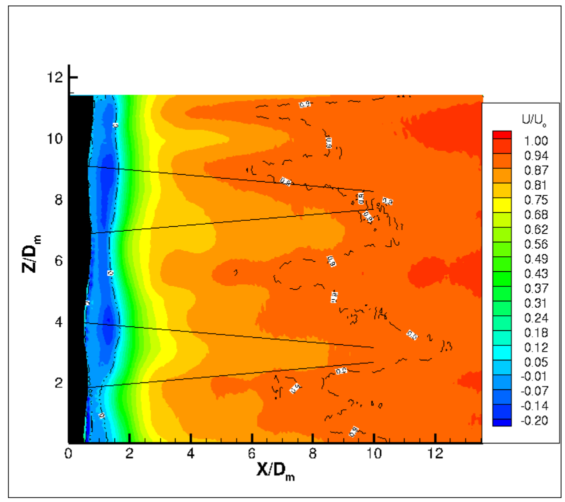

(b) Model B ($\alpha = 5°$, $\beta = -5°$)

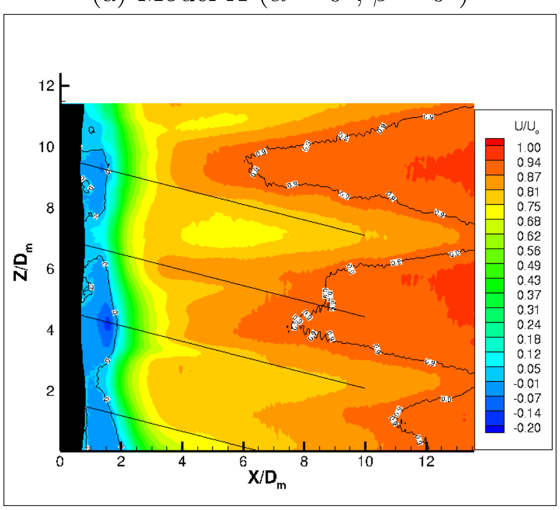

(c) Model C ($\alpha = -15°$, $\beta = -15°$)

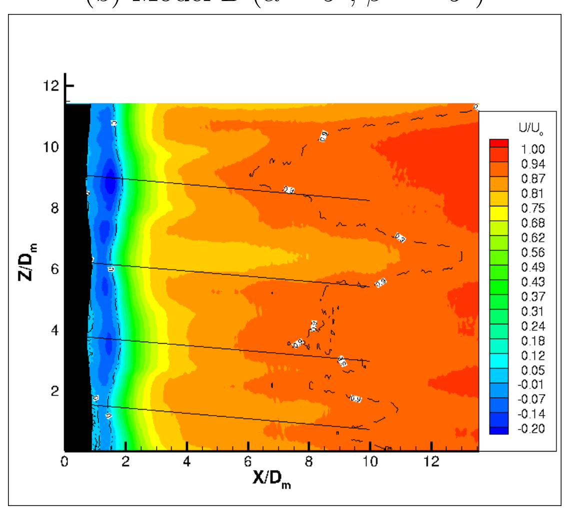

(d) Model D ($\alpha = -5°$, $\beta = -5°$)

Figure 31: Normalized mean u velocity fields in the wake of whisker models A-D (Vertical center x-z plane)

The u velocity field behind the model A is characterized by a reversed flow region immediately following the whisker model varying between 2.25 at the trough and 1.5 X/D_m at the peaks. The flow then begins to recover and shows mirroring of the whisker geometry. The flow recovers in the shortest distance downstream inline with the peak locations. The trough geometry recovers the slowest. The region inline with the troughs tend to recover at nearly twice the distance downstream as the regions inline with the peaks.

The u velocity field behind model B has a region of reverse flow right behind the whisker model varying between 1.5 at the troughs and 1.25 X/D_m at the peaks. The largest regions of reverse flow are inline with the trough locations and the most narrow occur behind the peak locations. The flow recovers to 90% of u/U_o as early as 6 X/D_m and completely by 12 X/D_m.

The u velocity field behind model C has a reversed flow region behind the model that shows a slight shift in the direction of the angle of incidence. The reversed flow regions extend as far as 2 $X/D - m$. The reversed flow behind the peak remains the most narrow with the region behind the trough have a wider reversed flow section. In the far wake region the flow recovers to the free steam flow near 6 D_m downstream behind trough locations and the flow recovers beyond the measurement window behind the peaks.

The u velocity field behind model D has a reversed flow region immediately following the whisker model followed by an recovery of u velocity. The reversed flow regions extend to 2 X/D_m behind the troughs and 1.5 X/D_m behind the peaks. Beyond 4 X/D_m the differences between peak and trough locations becomes much less distinct. Model D shows a recovery length, r as short as 6 X/D_m and the longest length at 13 X/D_m.

Figure 32 shows the mean w velocity field normalized with the free stream

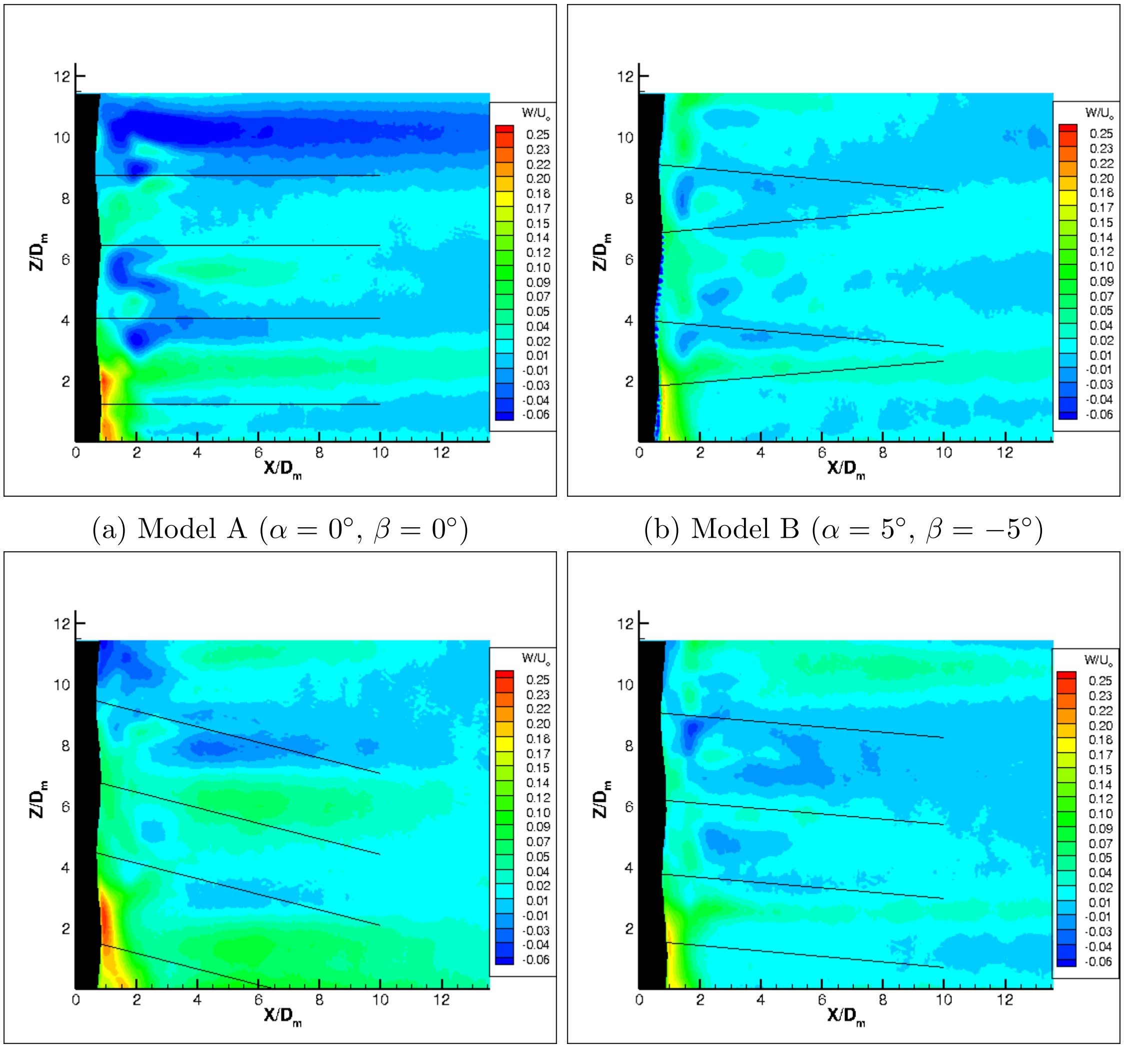

(a) Model A ($\alpha = 0°$, $\beta = 0°$)

(b) Model B ($\alpha = 5°$, $\beta = -5°$)

(c) Model C ($\alpha = -15°$, $\beta = -15°$)

(d) Model D ($\alpha = -5°$, $\beta = -5°$)

Figure 32: Normalized mean w velocity fields in the wake of whisker models A-D (Vertical center x-z plane)

velocity. Common to all of the models in Fig. 32, but with varying effect is the blooming at the bottom right of the model. These areas of high w are not representative of the true flow. Instead these are an effect of the model reflecting some of the laser light at the bottom edge of the model subsequently over exposing the images in this region and producing false velocity calculations.

Model A displays relatively low w velocity values predominately within $\pm 10\,\%$ of the free stream velocity U_o. The regions of positive or negative w extend downstream and for the most part do not switch direction.

Model B shows very low w velocity values. The angle of incidence at the trough location with a $-5°$ value seems to provide the dividing line between direction of w with positive values occurring above the mid point and negative values occurring below the mid point.

Model C has contains a mostly positive w velocity field with exceptions between 8 to 12 D_m in the *z-axis* as well as a smaller region near 4 D_m in the *z-axis*. Both of these areas correspond regions between the bottom half of the trough and the top half of the peak.

Model D has relatively low w velocity. There do not appear to be strong relationships with this model for direction of w and peak or trough location. There seems to be a slight tendency for the angle of incidence extension line to have positive w velocities associated with the peaks and negative values associated with the trough lines; however, these are rather subtle differences.

Figure 33 shows the vorticity, ω_y of the flow field defined by Eq. 3.16 normalized by D_m/U_o. This provides an indication of the strength of the rotation of the fluid out of plane about the *y-axis*.

Model A shows positive rotation about the *y-axis* between the top half of the peak and the bottom half of the trough. The rotation is opposite between the bottom half of the peak to the top half of the trough with rotation into the page or with negative rotation about the *y-axis*. The direction of the rotation remains fairly constant following the angle of incidence extension lines. The strength of the rotation reduces further downstream from the whisker model, but rotation can still be observed to the end of the measurement window.

Model B shows a pattern of positive rotation about the *y-axis* between the top half of the peak and the bottom half of the trough. Negative rotation about the

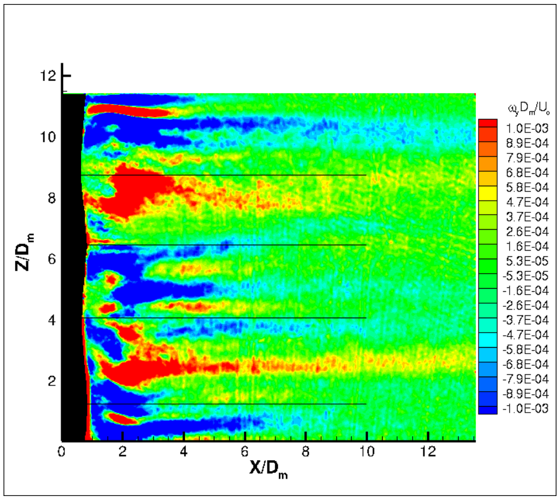

(a) Model A ($\alpha = 0°$, $\beta = 0°$)

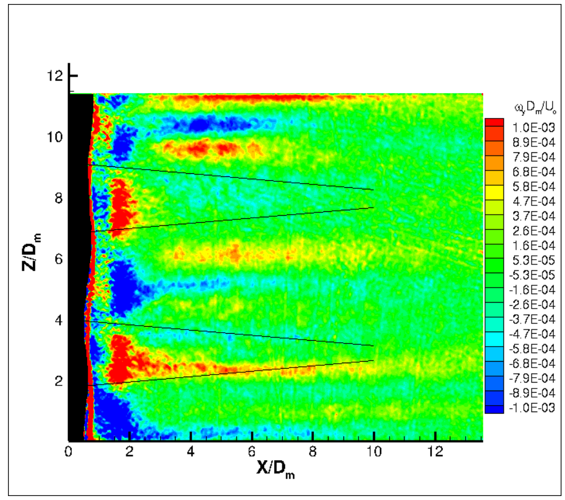

(b) Model B ($\alpha = 5°$, $\beta = -5°$)

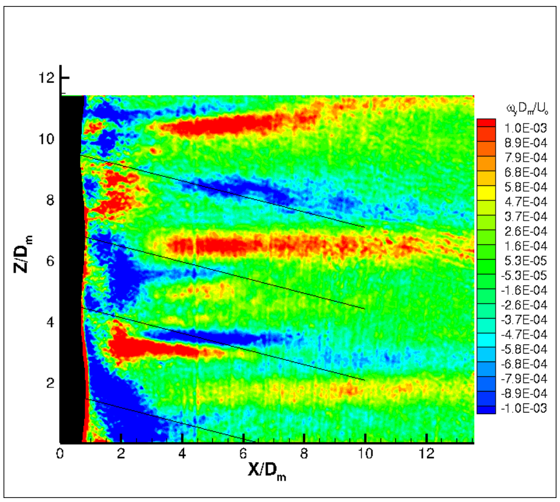

(c) Model C ($\alpha = -15°$, $\beta = -15°$)

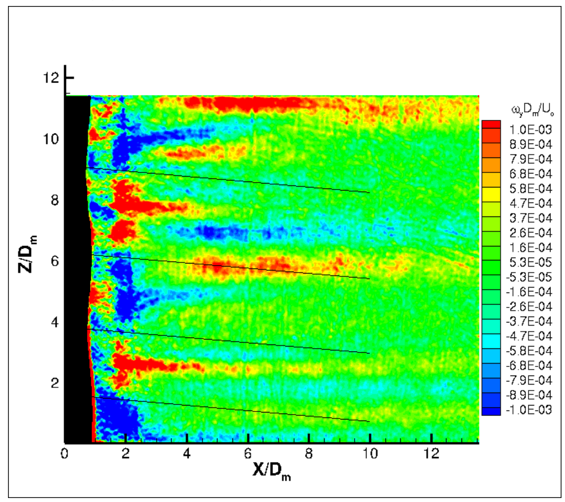

(d) Model D ($\alpha = -5°$, $\beta = -5°$)

Figure 33: Normalized ω_y vorticity fields in the wake of whisker models A-D (Vertical center x-z plane)

y-*axis* is observed between the bottom half of the peak and the top half of the trough. The areas of strong rotation are confined to regions within 3 D_m for the most part. Rotation is mostly dissipated by 10 D_m downstream of the model along the x-*axis*.

Model C also displays the pattern of positive rotation about the y-*axis* between the top of half of the peak and the bottom half of the trough. The negative rotation about the y-*axis* is located between the bottom half of the peak and top half of the trough. Rotation behind the $-5°$ model extends downstream and is visible but dissipated at the furthest locations downstream within the measurement window.

Model D maintains the general trend of positive rotation about the *y-axis* located between the top half of the peak and bottom half of the trough. Where the negative rotation tends to be located between the bottom half of the peak and the top half of the trough. The angle of incidence extension lines show a strong distinction between positive and negative rotation except for the bottom peak at the edge of the measurement window. The streaks of positive and negative appear to be smeared along the angle of incidence lines. The rotations are observed well downstream of the whisker model to the edge of the measurement window.

Figure 34 shows the turbulence intensity in the u direction defined by Eq. 3.11. The turbulence intensity T_u defines the magnitude of the fluctuations in the u velocity direction by taking the root mean square of the velocity fluctuation and normalizing it with the free stream velocity.

Model A shows a region of very low T_u immediately following the whisker model corresponding to the reversed u flow region. The low T_u is followed by a higher region of about 20% T_u with narrow segments of intensity between 27 and 30% T_u. The regions of 20% T_u extend parallel to the angle of incidence extension lines. These bands of 20% T_u are offset slightly from the mid points of the peak and trough locations. The regions directly inline with a peak or trough tend to have much lower T_u. The band of 20% T_u begin to see a reduction around 7 D_m downstream and have undergone significant reduction by 10 D_m downstream.

Model B has a region of 20% T_u immediately following the whisker model. This is followed narrow band of much higher intensity between 27 to 33% T_u. The bands of 20% T_u angle away from the center point of the trough location. These bands of 20% T_u are significantly reduced by 10 D_m downstream of the whisker model. Regions of lower T_u can be found at the same Z/D_m as the peak and trough locations starting

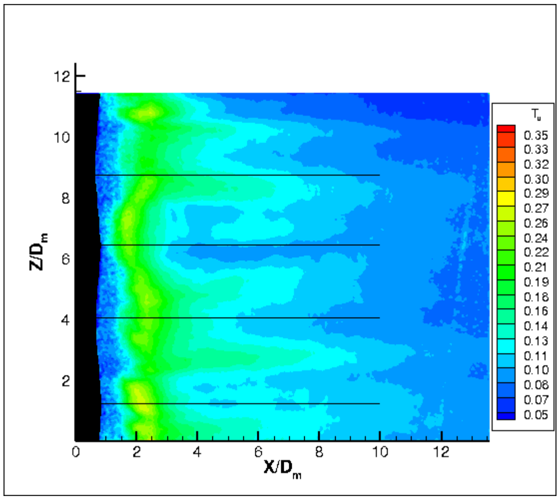

(a) Model A ($\alpha = 0°$, $\beta = 0°$)

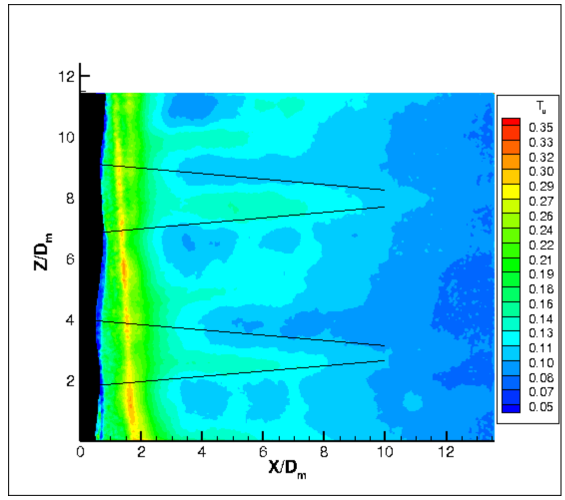

(b) Model B ($\alpha = 5°$, $\beta = -5°$)

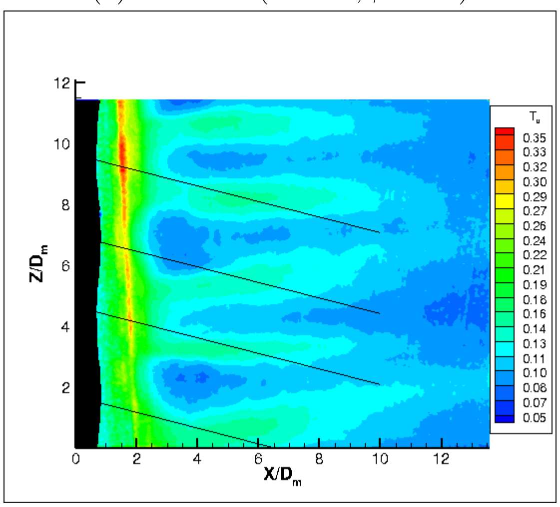

(c) Model C ($\alpha = -15°$, $\beta = -15°$)

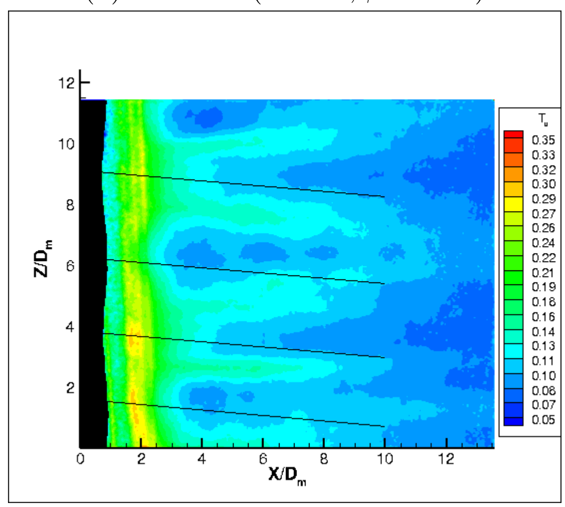

(d) Model D ($\alpha = -5°$, $\beta = -5°$)

Figure 34: Turbulence intensity of u fields in the wake of whisker models A-D (Vertical center x-z plane)

at 4 D_m downstream of the model.

Model C shows a region of 20% T_u immediately following the model. This is followed by a narrow region of higher T_u centered around 2 D_m downstream of the whisker model. Regions of lower T_u can be observed at the same Z/D_m positions that peak and trough point are located. The bands of 20% T_u extend at angles away from the trough center points. The T_u is reduced to 10% or less T_u by 10 D_m downstream of the model.

Model D shows T_u of 20% following the model with a vertical band of higher T_u centered around 2 D_m along the *x-axis*. The higher T_u covers a larger area as well as shows higher intensity near the top of the model with lower intensity and area observed near the bottom of the model. Areas of 10% T_u or less can be observed at the peak and trough locations starting at 4 D_m downstream of the model. The bands of 20% T_u angle away from the trough center point and reduce to 10% or less T_u shortly after 10 D_m downstream.

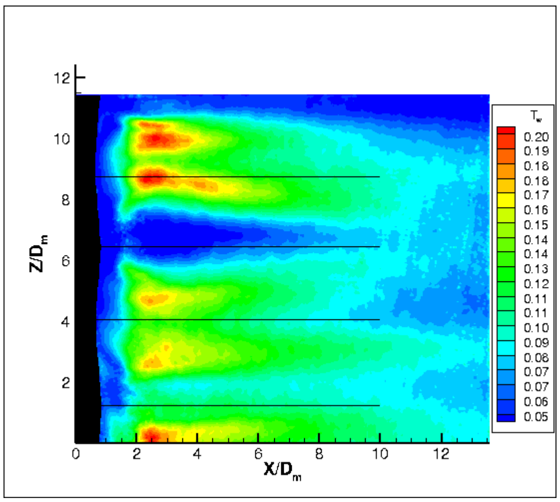

(a) Model A ($\alpha = 0°$, $\beta = 0°$)

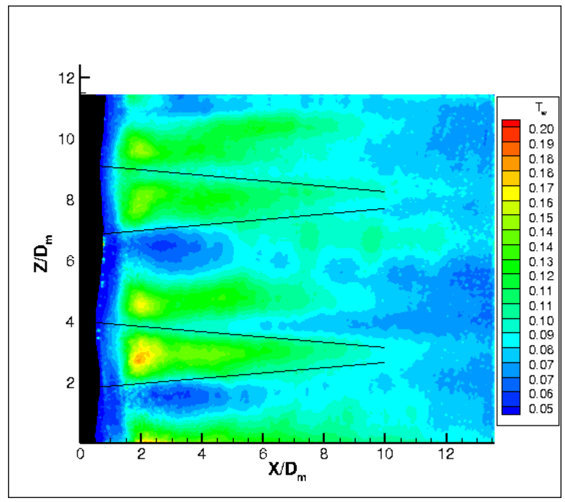

(b) Model B ($\alpha = 5°$, $\beta = -5°$)

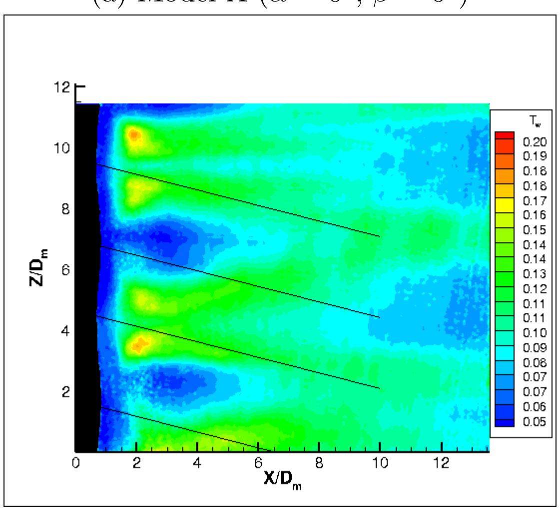

(c) Model C ($\alpha = -15°$, $\beta = -15°$)

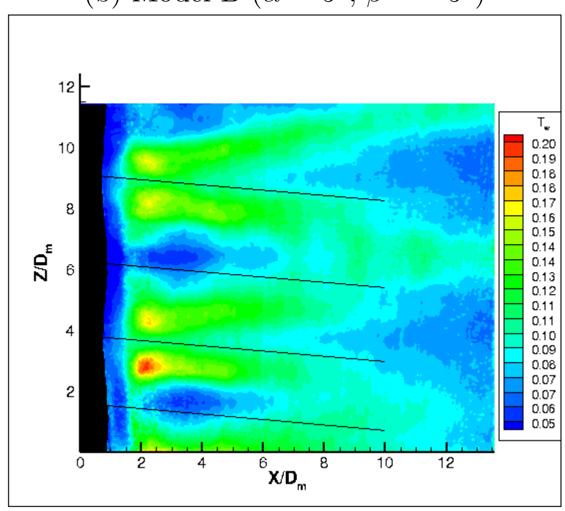

(d) Model D ($\alpha = -5°$, $\beta = -5°$)

Figure 35: Turbulence intensity of w fields in the wake of whisker models A-D (Vertical center x-z plane)

Figure 35 contains the turbulence intensity of the w flow defined by Eq. 3.13. Model A shows a low region of T_w following the model. There are paired pockets of high T_w that center near 3 X/D_m downstream and are located along above and below trough angle of incidence extension lines. Inline with the peak locations are regions of much lower T_w. The peak at 6 Z/D_m has a much larger coverage area as well as much lower T_w than the peak located at 1.5 Z/D_m.

Model B has a low intensity region immediately following the model. Centered at 2 X/D_m are paired pockets of higher T_w that reside on either side of the trough angle of incidence extension lines. The pair centered on the trough located at 4 Z/D_m show a larger area of coverage and higher intensity than those at 9 Z/D_m. The regions of T_w between 10 and 15% extend at angles away from the trough center points. At the Z/D_m peak locations there are areas of lower T_w that extend until 5 X/D_m.

Model C has a region of low T_w following the model extending until 1.5 X/D_m. At 2 X/D_m there are paired pockets of high intensity regions that reside on either side of the trough angle of incidence extension line. The pair centered on 4 Z/D_m has a higher intensity as well as a slightly larger area than those centered at the trough located at 9 Z/D_m. Following the peaks are zones of much lower T_w extending to 6 X/D_m downstream. The bands of T_w between 10 and 15% extend angled away from the trough center points.

Model D has an area of low T_w following the model that extends 1.5 X/D_m downstream. The same paired pockets of high T_w are observed in this model located o either side of the trough angle of incidence extension lines. Bands of 10 to 15% T_w extend from the trough center points and angle away. Regions of low T_w are found at the peak locations of 7 and 2 Z/D_m.

Figure 36 shows the Reynolds shear stress, τ''_{xz}, defined by 3.15 normalized by the square of the free stream velocity. Model A has a band of higher Reynolds shear

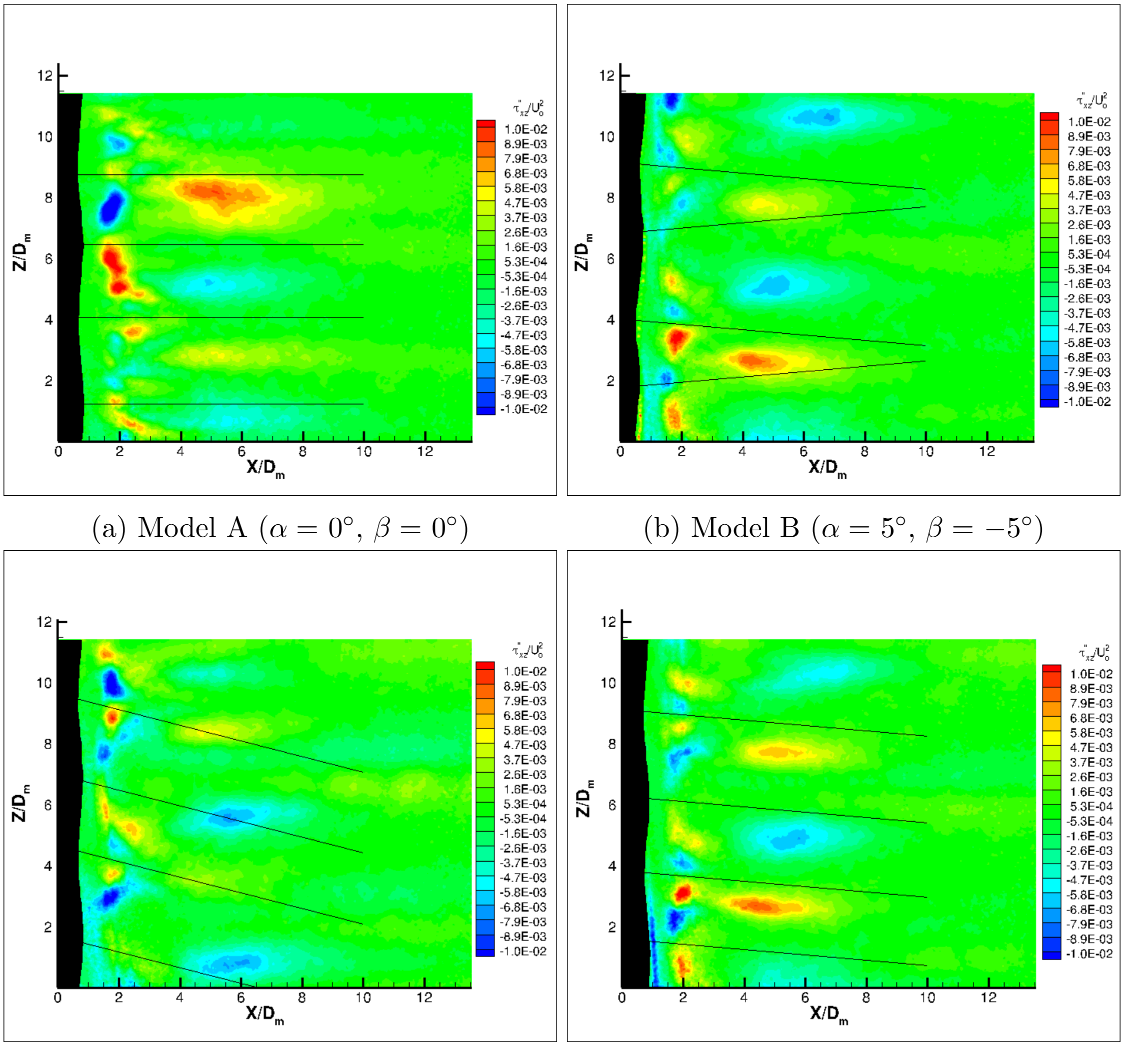

(a) Model A ($\alpha = 0°$, $\beta = 0°$)

(b) Model B ($\alpha = 5°$, $\beta = -5°$)

(c) Model C ($\alpha = -15°$, $\beta = -15°$)

(d) Model D ($\alpha = -5°$, $\beta = -5°$)

Figure 36: Reynolds shear stress fields in the wake of whisker models A-D (Vertical center x-z plane)

stress centering at 2 X/D_m. Other non zero regions of τ''_{xz} are centered near 5.5 X/D_m with positive regions located between the top half of the peak and bottom half of the trough and negative regions occurring at between the bottom half of the peak and top half of the trough.

Model B has an alternating pattern of positive and negative τ''_{xz} regions centered at 2 X/D_m. Further downstream at 5 X/D_m another region of alternating τ''_{xz} is observed. In the far wake region, beyond 3 X/D_m positive τ''_{xz} regions are located between the top half of the peak and bottom half of the trough and negative regions are located between the bottom half of the peak and top half of the trough.

Model C has regions of high τ''_{xz} in the near wake centered at 2 X/D_m with an alternating patter of direction of τ''_{xz}. Further downstream centered between 5 and 6 X/D_m is another region of alternating τ''_{xz}. The negative regions are have higher intensity and cover a larger region than the positive τ''_{xz} regions in the far wake.

Model D has a region of high τ''_{xz} centered at 2 X/D_m of alternating direction. Center between 4 and 6 X/D_m is another region of alternating τ''_{xz} of higher magnitude. Positive regions of τ''_{xz} are located between the top half of the peak and bottom half of the trough locations and negative regions located between the bottom half of the peak and top half of the trough locations.

3.3.2 Cross-Sectional Plane at the Peak

This section will focus on the wake structure observed at a cross-sectional plane at the peak location. Here the model is being observed from above, represented by the back ellipse showing half of the major axis diameter.

Figure 37 displays the mean u velocity normalized with the free stream velocity. In addition to the color contour of the normalized velocity a dashed line indicated the recovery length, r, of $0.9U/U_o$ and a 'dahsed-dot-dot' line indicated the reversed flow section with $U_o = 0$. Model A has a region of reverse flow that extends to 1.4 X/D_m and then begins to recover. The flow along the centerline of the model never fully recovers within this measurement window. The wake shows a slight growth in width that occurs just beyond the reverse flow region and then stabilizes at 0.5 D_m on either side of the whisker model.

Model B has a reversed flow region that extends 1.3 X/Dm downstream. The flow begins to recover until 3.6 X/D_m downstream where the flow experiences a

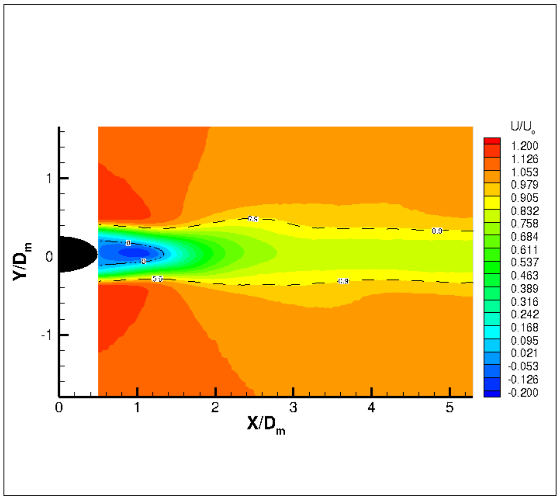

(a) Model A ($\alpha = 0°$, $\beta = 0°$)

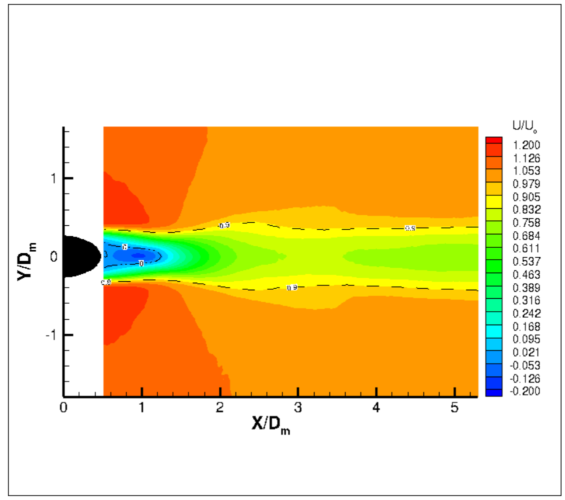

(b) Model B ($\alpha = 5°$, $\beta = -5°$)

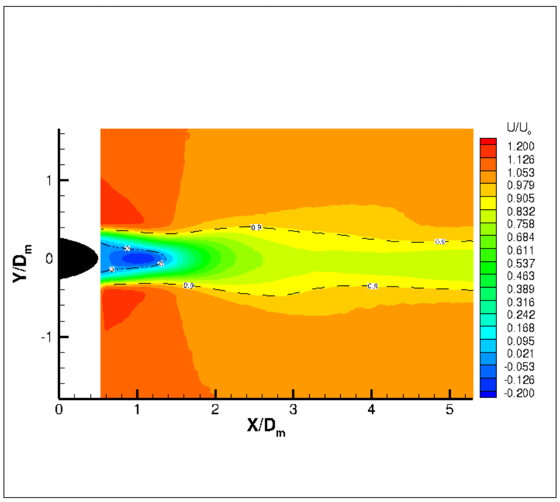

(c) Model C ($\alpha = -15°$, $\beta = -15°$)

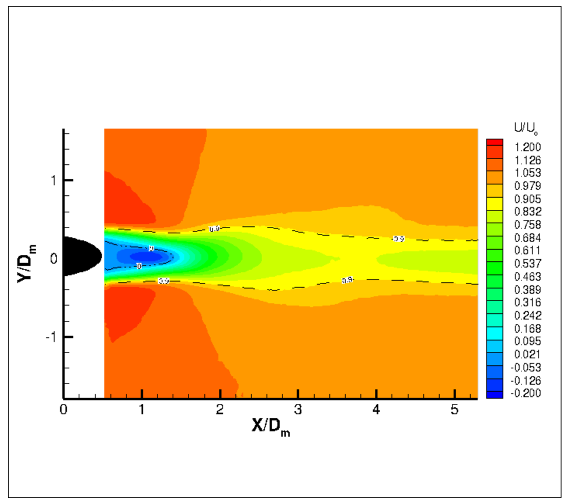

(d) Model D ($\alpha = -5°$, $\beta = -5°$)

Figure 37: Normalized u velocity fields in the wake of whisker models A-D (Peak cross section x-y plane)

reduction in u at the centerline. the reduced u is restricted to the center of the wake and reaches 0.25 D_m in both directions off the centerline. The wake velocity never fully recovers within this measurement window.

Model C has a reversed flow region extending to 1.4 X/D_m. The wake shows a slight expansion in the *y-axis* beginning at 1.5 X/D_m and reaching a maximum width of 0.5 D_m in either direction off the centerline. The u velocity begins recovering at 1.4 X/D_m. The flow in the wake does not fully recover within the measurement window.

Model D has a reversed flow region that extends to 1.4 X/D_m downstream. The wake u velocity then begins to recover at 1.4 X/D_m until 4 X/D_m were the u experiences a slight reduction. The u does not fully recover within the measurement window. The wake expands from 0.25 D_m near the model to a maximum of 0.5 D_m in both directions off of the centerline.

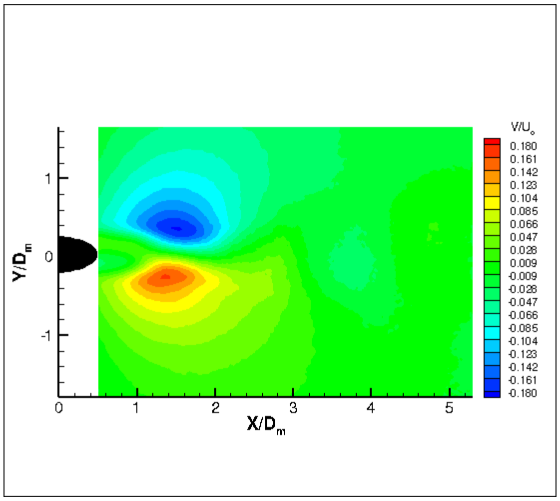

(a) Model A ($\alpha = 0°$, $\beta = 0°$)

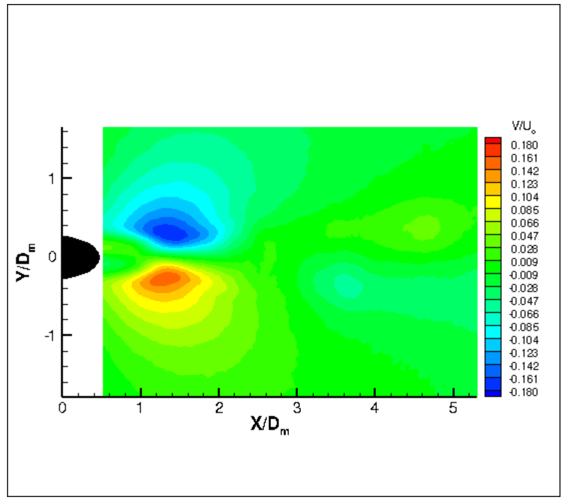

(b) Model B ($\alpha = 5°$, $\beta = -5°$)

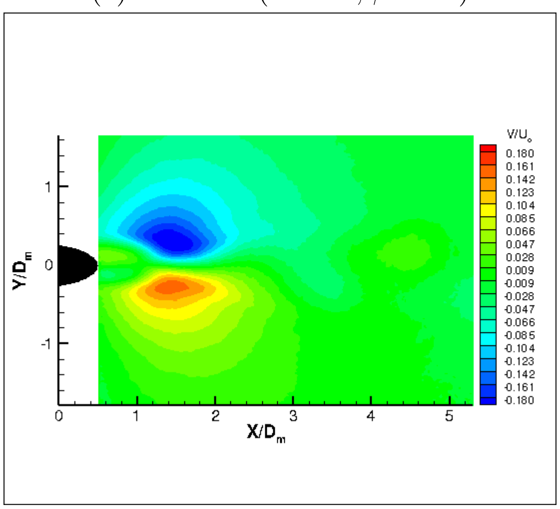

(c) Model C ($\alpha = -15°$, $\beta = -15°$)

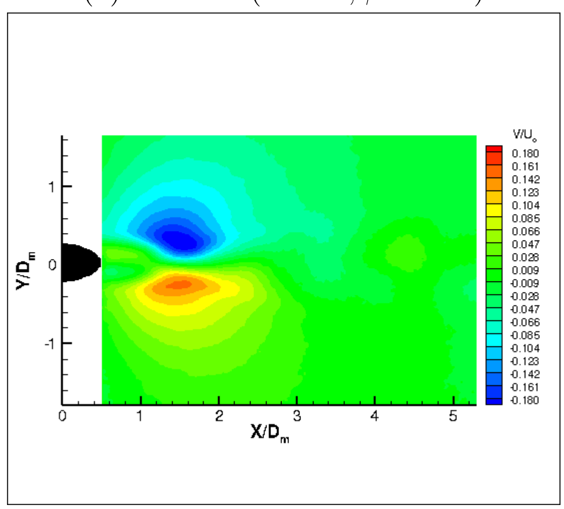

(d) Model D ($\alpha = -5°$, $\beta = -5°$)

Figure 38: Normalized v velocity fields in the wake of whisker models A-D (Peak cross section x-y plane)

Figure 38 shows the mean v flow normalized with the free stream velocity. Model A shows two regions of high v velocity. The region above the model centerline experiencing negative flow and the region below the model centerline experiencing positive flow. The regions of highest velocity are centered around 1.5 X/D_m downstream extending to the model and reaching 2.5 X/D_m downstream after which minimal v velocity is observed. The regions of nonzero v extend in the *y-axis* to $\pm 1.2D_m$.

Model B shows two regions of high v velocity. The region above the model centerline experiencing negative flow and the region below the model centerline experiencing positive flow. The regions of highest velocity are centered around 1.4 X/D_m downstream extending to the model and reaching 2.0 X/D_m downstream after which minimal v velocity is observed. The regions of nonzero v extend in the *y-axis* to $\pm 1D_m$.

Model C shows two regions of high v velocity. The region above the model centerline experiencing negative flow and the region below the model centerline experiencing positive flow. The regions of highest velocity are centered around 1.5 X/D_m downstream extending to the model and reaching 2.5 X/D_m downstream after which minimal v velocity is observed. The regions of nonzero v extend in the *y-axis* to $\pm 1D_m$.

Model D shows two regions of high v velocity. The region above the model centerline experiencing negative flow and the region below the model centerline experiencing positive flow. The regions of highest velocity are centered around 1.5 X/D_m downstream extending to the model and reaching 2.5 X/D_m downstream after which minimal v velocity is observed. The regions of nonzero v extend in the *y-axis* to $\pm 1D_m$.

Figure 39 is the vorticity about the *z-axis*, ω_z normalized with D_m/U_o. All four models exhibit very similar $\omega_z D_m/U_o$ fields. Strong rotation about the *z-axis* occurs near the whisker model. Positive rotation is observed above the centerline of the model and negative rotation is observed below the whisker centerline. These

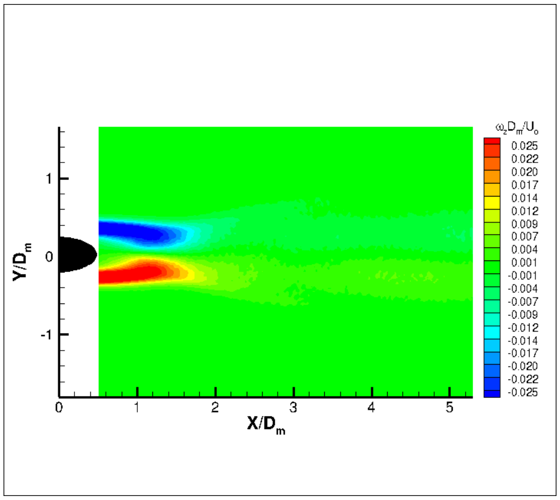

(a) Model A ($\alpha = 0°$, $\beta = 0°$)

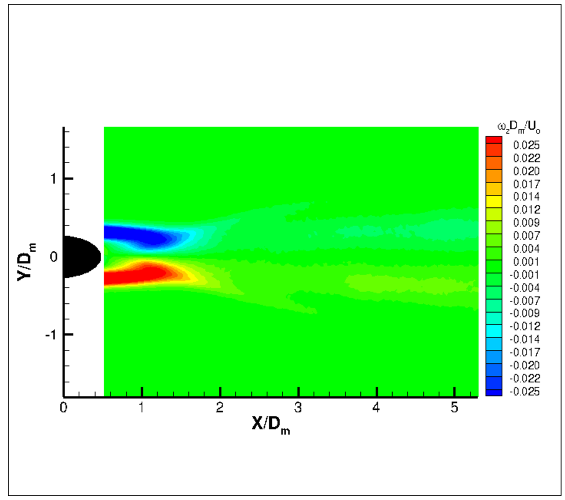

(b) Model B ($\alpha = 5°$, $\beta = -5°$)

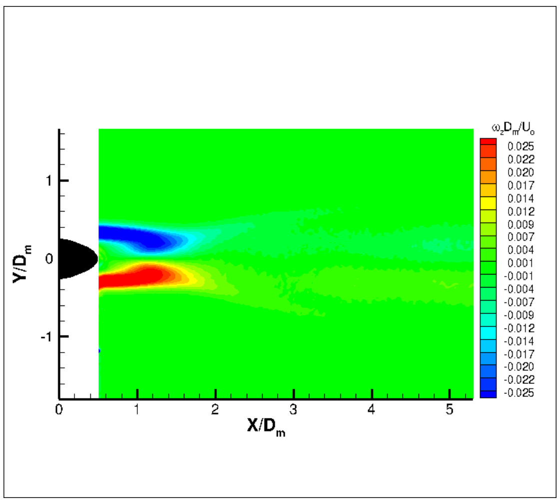

(c) Model C ($\alpha = -15°$, $\beta = -15°$)

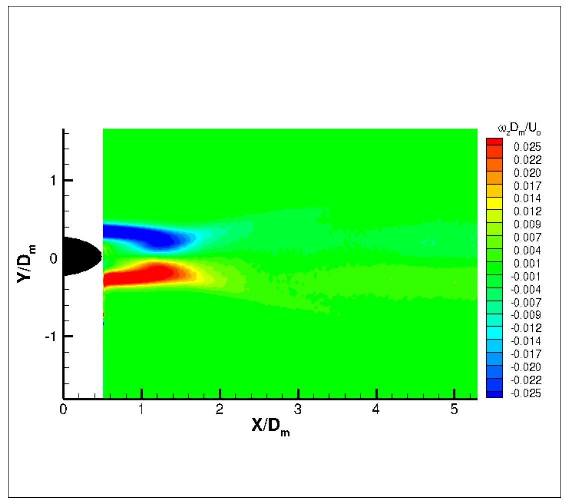

(d) Model D ($\alpha = -5°$, $\beta = -5°$)

Figure 39: Normalized ω_z vorticity fields in the wake of whisker models A-D (Peak cross section x-y plane)

regions of strong rotation extend to 1.8 X/D_m with minimal to no rotation about the *z-axis* observed elsewhere in the wake.

Figure 40 is the turbulence intensity in the u direction, T_u. Model A has a region of low T_u directly following the whisker model. This area of low intensity extends to 1.0 X/D_m downstream of the whisker model. Centered at 1.5 X/D_m extending from 1.2 to 2 X/D_m along the *x-axis* and above and below 0 Y/D_m are two pockets of high T_u reaching a maximum intensity of 30% T_u. The remainder of

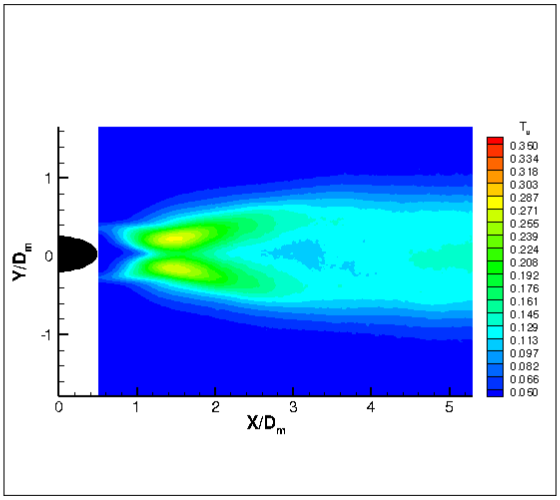

(a) Model A ($\alpha = 0°$, $\beta = 0°$)

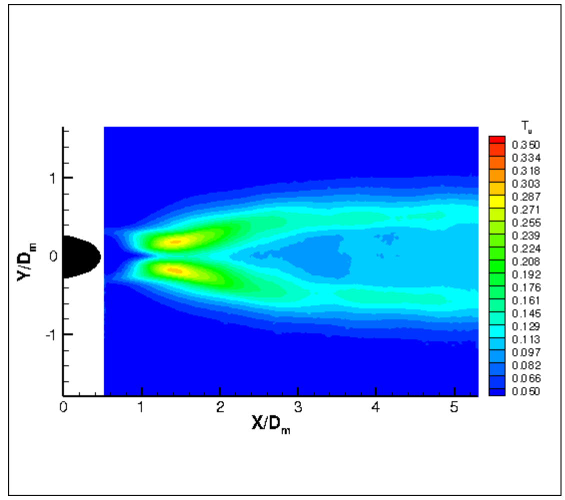

(b) Model B ($\alpha = 5°$, $\beta = -5°$)

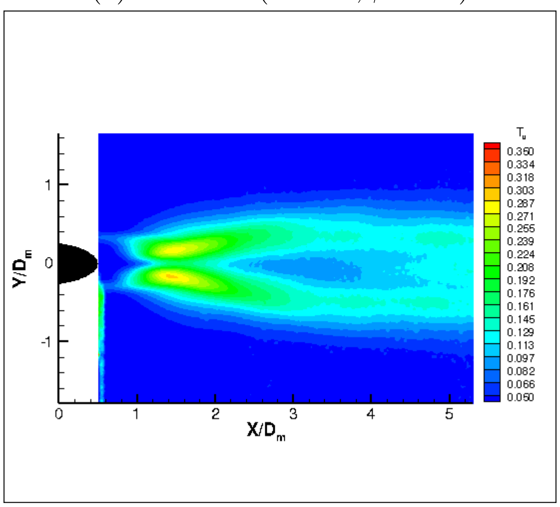

(c) Model C ($\alpha = -15°$, $\beta = -15°$)

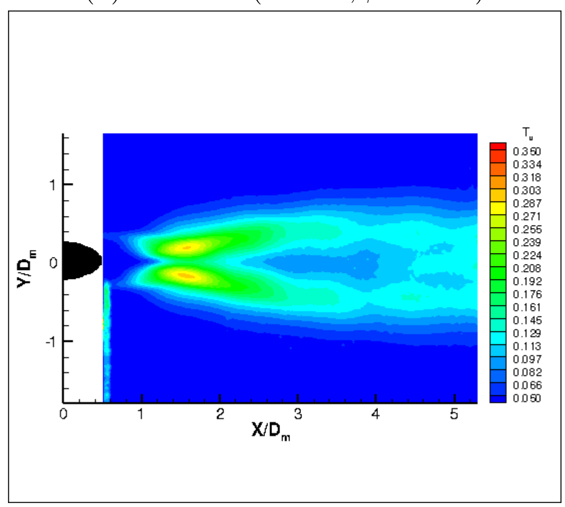

(d) Model D ($\alpha = -5°$, $\beta = -5°$)

Figure 40: Turbulence intensity of u fields in the wake of whisker models A-D (Peak cross section x-y plane)

the wake is characterized by T_u in the 10 to 20% range. T_u above the free stream condition extends 1 D_m in both directions from the model centerline.

Model B has an area of low T_u following the model that extends to 1.0 X/D_m. There are two pockets of high T_u with magnitudes above 30%. These pockets begin at 1.2 X/D_m extend to 2 X/D_m. There is an area of lower T_u separating them along the model centerline. These pockets of high T_u are slightly angled away from the centerline in the downstream direction. The remainder of the wake is characterized by T_u in the 10 to 20% range. T_u greater than the free stream T_u is observed 1 D_m off the centerline in both directions.

Model C has an area of low T_u following the model that extends to 1.2 X/D_m. There are two pockets of high T_u with magnitudes above 30%. These pockets begin at 1.3 X/D_m extend to 2.1 X/D_m. There is an area of lower T_u separating them along the model centerline. These pockets of high T_u are slightly angled away from the centerline in the downstream direction. The remainder of the wake is characterized by T_u in the 10 to 20% range. T_u greater than the free stream T_u is observed 1 D_m off the centerline in both directions.

Model D has an area of low T_u following the model that extends to 1.0 X/D_m. There are two pockets of high T_u with magnitudes reaching maximums around 30%. These pockets begin at 1.2 X/D_m extend to 2.2 X/D_m. There is an area of lower T_u separating them along the model centerline. These pockets of high T_u are slightly angled away from the centerline in the downstream direction. The remainder of the wake is characterized by T_u in the 10 to 20% range. T_u greater than the free stream T_u is observed 1 D_m off the centerline in both directions.

Figure 41 shows T_v for the peak cross-sectional measurement plane. Model A shows a region of high T_v that is centered on the model centerline at 2.2 X/D_m downstream of the model. The area of T_v greater than 30% extends from 1.4 to 4 X/D_m and -0.2 to 0.2 Y/D_m. The wake of the model produces T_v greater than the free stream T_v from -1.2 to 1.2 Y/D_m.

Model B shows a region of high T_v that is centered on the model centerline at 2.2 X/D_m downstream of the model. The area of T_v greater than 30% extends from 1.3 to 4 X/D_m and -0.2 to 0.2 Y/D_m. The wake of the model produces T_v greater than the free stream T_v from -1.2 to 1.2 Y/D_m.

Model C shows a region of high T_v that is centered on the model centerline at

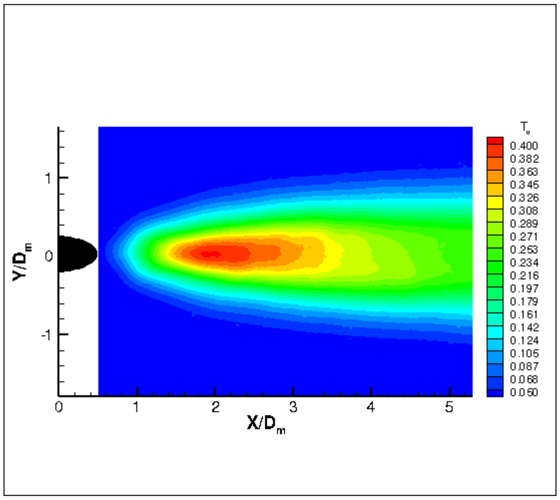

(a) Model A ($\alpha = 0°$, $\beta = 0°$)

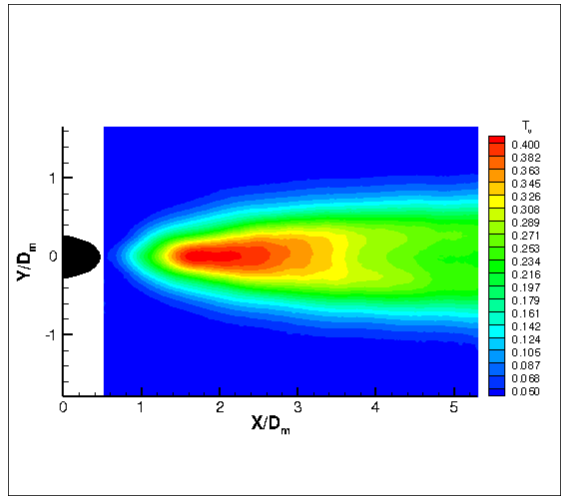

(b) Model B ($\alpha = 5°$, $\beta = -5°$)

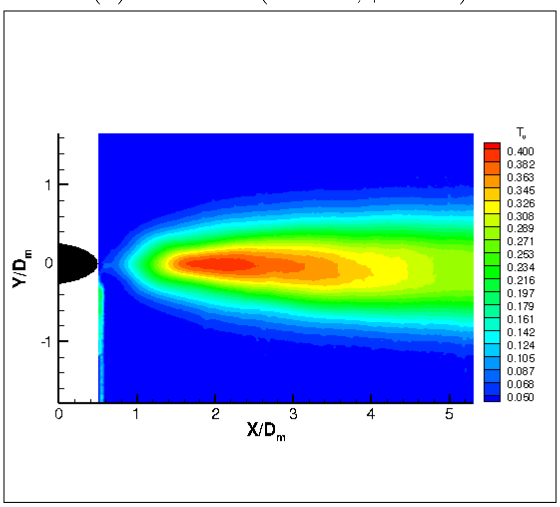

(c) Model C ($\alpha = -15°$, $\beta = -15°$)

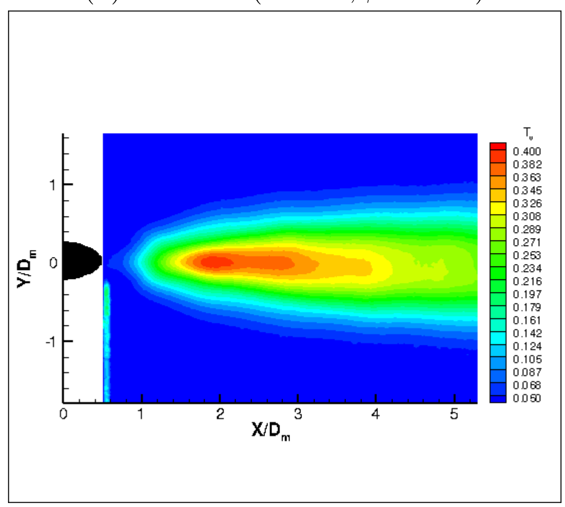

(d) Model D ($\alpha = -5°$, $\beta = -5°$)

Figure 41: Turbulence intensity of v fields in the wake of whisker models A-D (Peak cross section x-y plane)

2.2 X/D_m downstream of the model. The area of T_v greater than 30% extends from 1.4 to 5 X/D_m and -0.2 to 0.2 Y/D_m. The wake of the model produces T_v greater than the free stream T_v from -1.2 to 1.2 Y/D_m.

Model D shows a region of high T_v that is centered on the model centerline at 2.2 X/D_m downstream of the model. The area of T_v greater than 30% extends from 1.4 to 4.8 X/D_m and -0.2 to 0.2 Y/D_m. The wake of the model produces T_v greater than the free stream T_v from -1.2 to 1.2 Y/D_m.

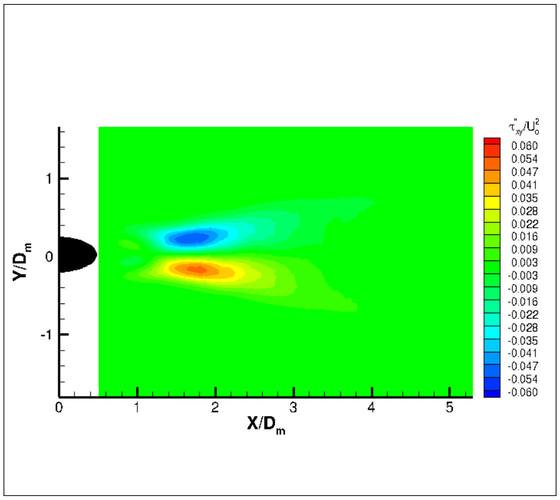

(a) Model A ($\alpha = 0°$, $\beta = 0°$)

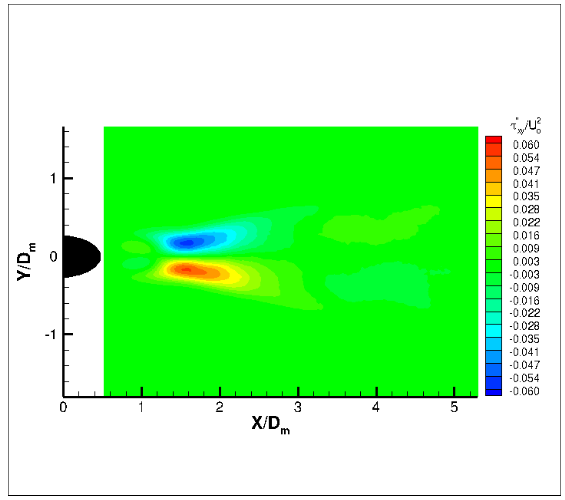

(b) Model B ($\alpha = 5°$, $\beta = -5°$)

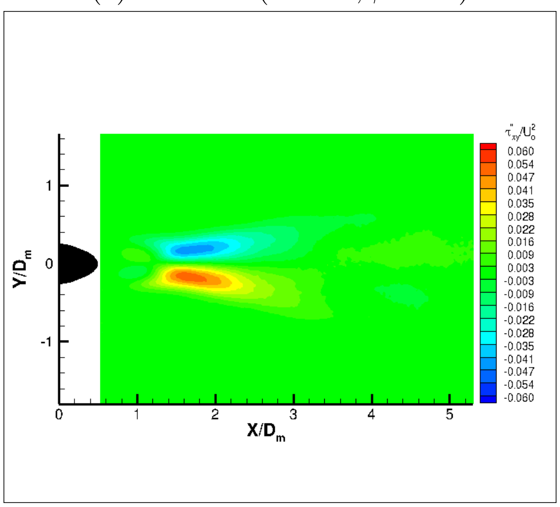

(c) Model C ($\alpha = -15°$, $\beta = -15°$)

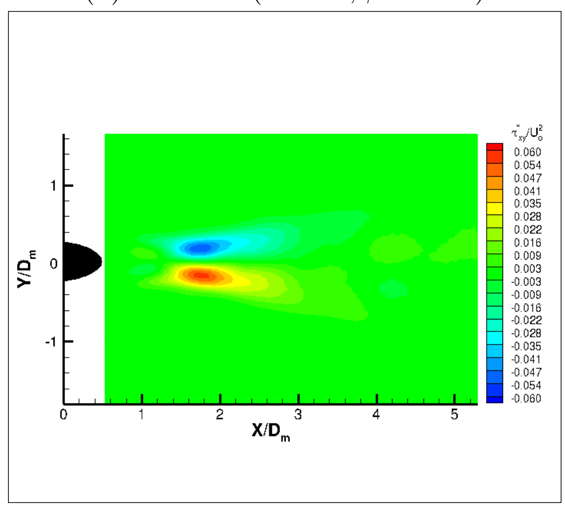

(d) Model D ($\alpha = -5°$, $\beta = -5°$)

Figure 42: Reynolds shear stress fields in the wake of whisker models A-D (Peak cross section x-y plane)

Figure 42 shows the Reynolds shear stress in the x-y plane for the peak cross-sectional measurement plane. Model A shows a region of high τ''_{xy} centered at 1.7 X/D_m. Negative τ''_{xy} is located on the positive *y-axis* and positive τ''_{xy} is located in the negative *y-axis*. The regions of non-zero τ''_{xy} begin at 1.2 X/D_m and extend to 3 X/D_m.

Model B shows a region of high τ''_{xy} centered at 1.6 X/D_m. Negative τ''_{xy} is located on the positive *y-axis* and positive τ''_{xy} is located in the negative *y-axis*. The regions of non-zero τ''_{xy} begin at 1.2 X/D_m and extend to 2.7 X/D_m.

Model C shows a region of high τ''_{xy} centered at 1.7 X/D_m. Negative τ''_{xy} is located on the positive *y-axis* and positive τ''_{xy} is located in the negative *y-axis*. The regions of non-zero τ''_{xy} begin at 1.2 X/D_m and extend to 3 X/D_m.

Model D shows a region of high τ''_{xy} centered at 1.8 X/D_m. Negative τ''_{xy} is located on the positive *y-axis* and positive τ''_{xy} is located in the negative *y-axis*. The regions of non-zero τ''_{xy} begin at 1.2 X/D_m and extend to 3 X/D_m.

3.3.3 Cross-Sectional Plane at the Trough

The final test case conducted was the cross-sectional plane located at the trough of the whisker models. The following figures will describe the flow conditions observed behind the four different whisker models.

Figure 43 contains the u flow normalized with the free stream velocity. In addition to the color contour of the normalized velocity a dashed line indicated the recovery length, r, of $0.9U/U_o$ and a 'dahsed-dot-dot' line indicated the reversed flow section with $U_o = 0$. Model A has a reversed flow region that extends from the model to 1.9 X/D_m downstream. The u flow then begins to recover not fully reaching the free stream velocity condition within the measurement window. The flow recovery length is not visible within this measurement frame. The wake of reduced u velocity extends between 0.6 and -0.6 Y/D_m.

Model B has a reversed flow region that extends from the model to 1.7 X/D_m downstream. The u flow then begins to recover reaching 90% of the free stream flow at 4.2 X/D_m nearly fully recovered by the end of the measurement window. The wake of reduced u velocity extends between 0.6 and -0.6 Y/D_m.

Model C has a reversed flow region that extends from the model to 2.0 X/D_m downstream. The u flow then begins to recover not reaching 90% of the free stream

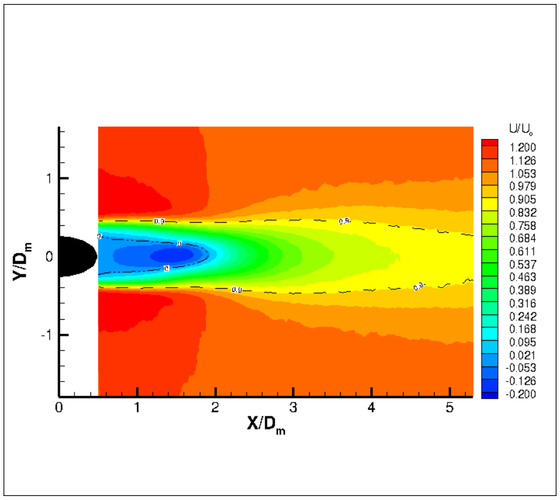

(a) Model A ($\alpha = 0°$, $\beta = 0°$)

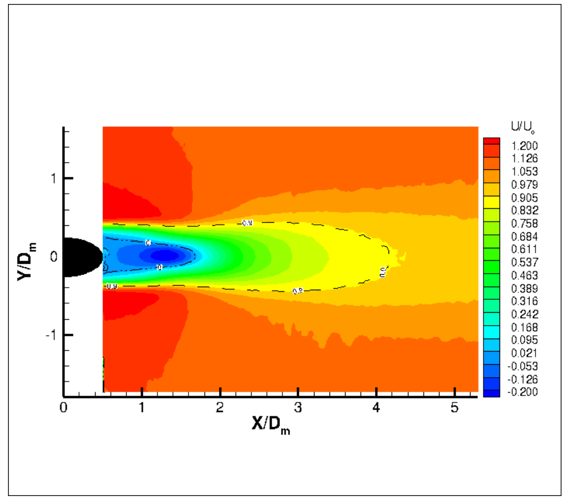

(b) Model B ($\alpha = 5°$, $\beta = -5°$)

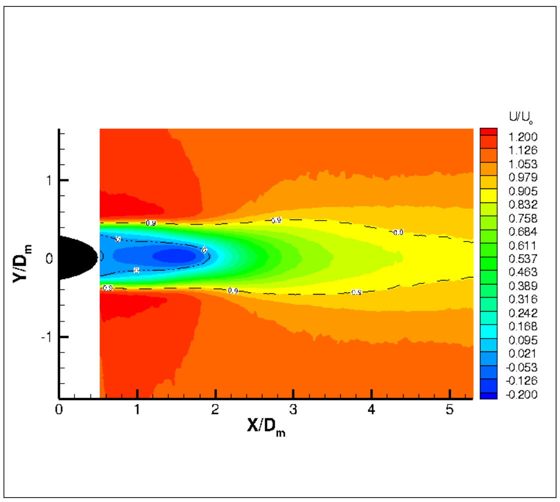

(c) Model C ($\alpha = -15°$, $\beta = -15°$)

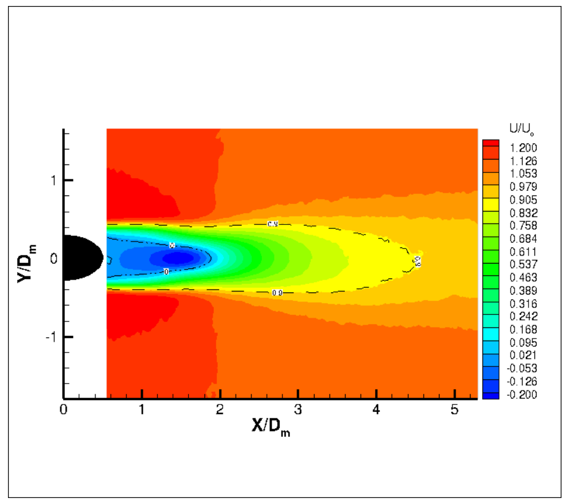

(d) Model D ($\alpha = -5°$, $\beta = -5°$)

Figure 43: Normalized u velocity fields in the wake of whisker models A-D (Trough cross section x-y plane)

flow before the end of the measurement window. The wake of reduced u velocity extends between 0.6 and -0.6 Y/D_m.

Model D has a reversed flow region that extends from the model to 1.9 X/D_m downstream. The u flow then begins to recover reaching 90% of the free stream flow at 4.5 X/D_m and does not fully recover within the measurement window. The wake of reduced u velocity extends between 0.6 and -0.6 Y/D_m.

Figure 44 shows the v velocity normalized with the free stream velocity. Model

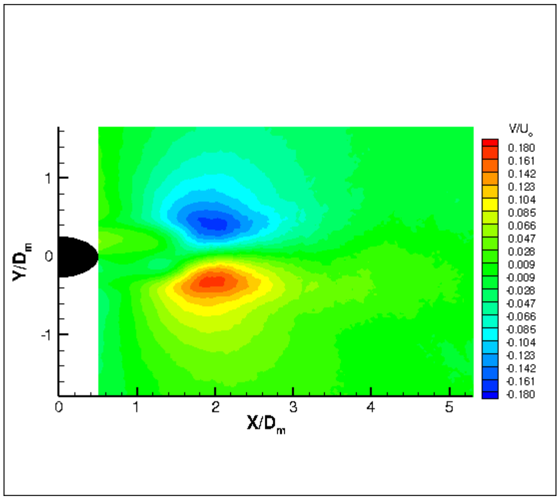

(a) Model A ($\alpha = 0°$, $\beta = 0°$)

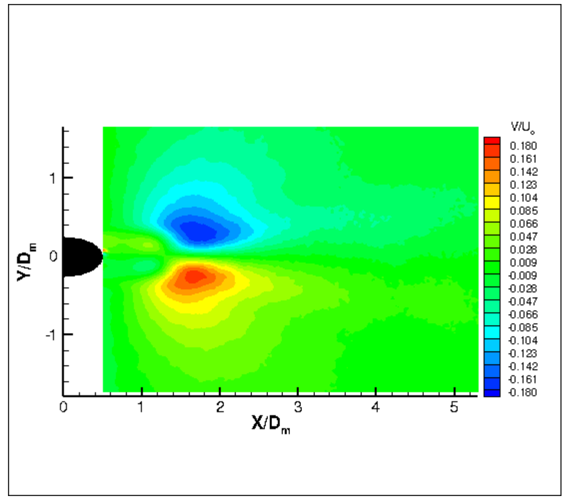

(b) Model B ($\alpha = 5°$, $\beta = -5°$)

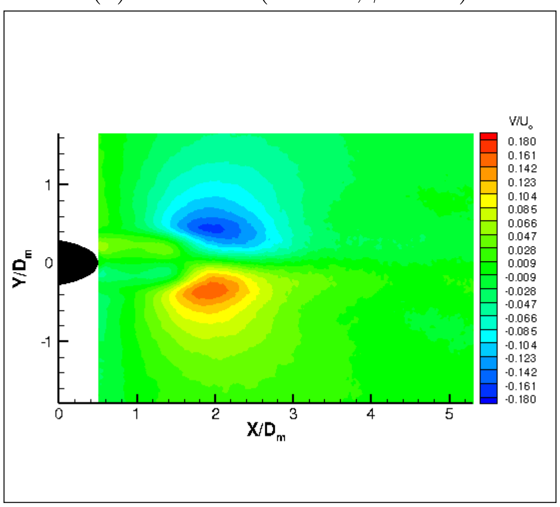

(c) Model C ($\alpha = -15°$, $\beta = -15°$)

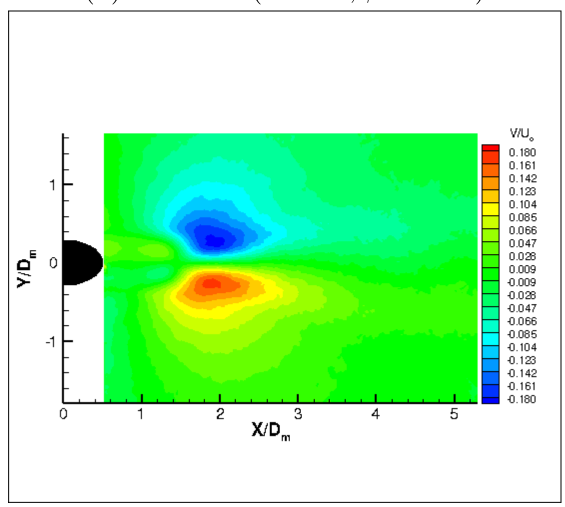

(d) Model D ($\alpha = -5°$, $\beta = -5°$)

Figure 44: Normalized v velocity fields in the wake of whisker models A-D (Trough cross section x-y plane)

A has two zones of nonzero v velocity. These regions are centered at 2 X/D_m downstream of the model and extend from 1.2 to 3 X/D_m. The region above the model centerline has a negative direction while the region below the model centerline has a positive direction. The region of negative $v$extend from 0.2 to 1.2 Y/D_m where the region of positive $v$extend from -0.2 to -1.2 Y/D_m.

Model B has two zones of nonzero v velocity. These regions are centered at 1.7 X/D_m downstream of the model and extend from 1.0 to 3 X/D_m. The region above the model centerline has a negative direction while the region below the model centerline has a positive direction. The region of negative $v$extend from 0.2 to 1.2 Y/D_m where the region of positive $v$extend from -0.2 to -1.2 Y/D_m.

Model C has two zones of nonzero v velocity. These regions are centered at 1.9 X/D_m downstream of the model and extend from 1.2 to 3.2 X/D_m. The region above the model centerline has a negative direction while the region below the model centerline has a positive direction. The region of negative $v$extend from 0.2 to 1.2 Y/D_m where the region of positive $v$extend from -0.2 to -1.2 Y/D_m.

Model D has two zones of nonzero v velocity. These regions are centered at 2.0 X/D_m downstream of the model and extend from 1.2 to 3 X/D_m. The region above the model centerline has a negative direction while the region below the model centerline has a positive direction. The region of negative $v$extend from 0.2 to 1.2 Y/D_m where the region of positive $v$extend from -0.2 to -1.2 Y/D_m.

Figure 45 contains the ω_z normalized by D_m/U_o for the trough cross-sectional plane. Model A has two arms of high ω_z. The positive rotation arm is located below the model centerline and extends to 2.2 X/D_m downstream. The negative rotation arm is located above the model centerline and extends to 2.2 X/D_m downstream. The remained of the ω_z field is relatively small in magnitude.

Model B has two arms of high ω_z. The positive rotation arm is located below the model centerline and extends to 2.0 X/D_m downstream. The negative rotation arm is located above the model centerline and extends to 2.0 X/D_m downstream. The remained of the ω_z field is relatively small in magnitude.

Model C has two arms of high ω_z. The positive rotation arm is located below the model centerline and extends to 2.0 X/D_m downstream. The negative rotation arm is located above the model centerline and extends to 2.0 X/D_m downstream. The remained of the ω_z field is relatively small in magnitude.

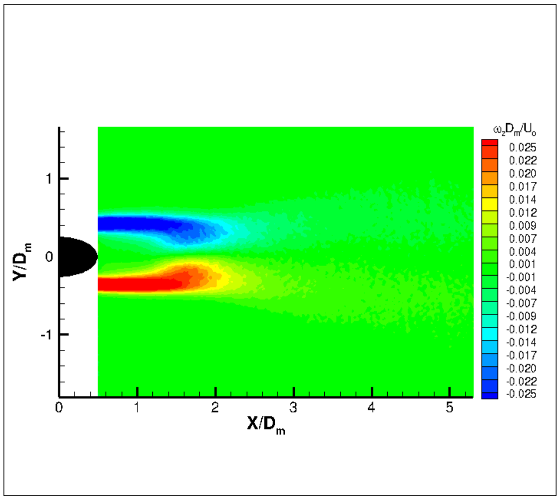

(a) Model A ($\alpha = 0°$, $\beta = 0°$)

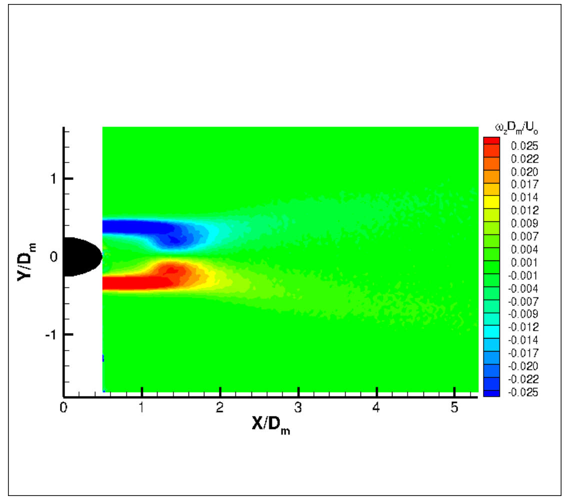

(b) Model B ($\alpha = 5°$, $\beta = -5°$)

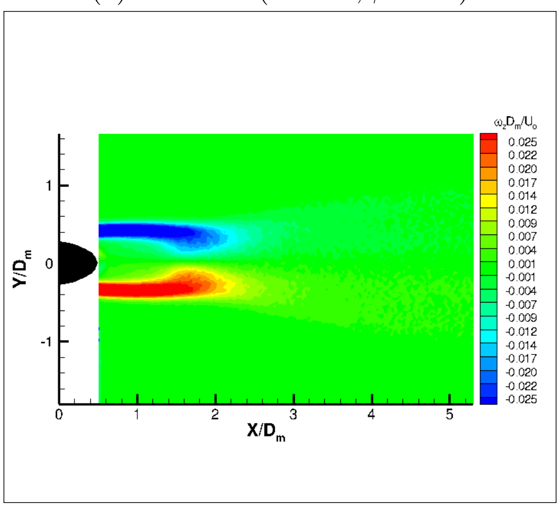

(c) Model C ($\alpha = -15°$, $\beta = -15°$)

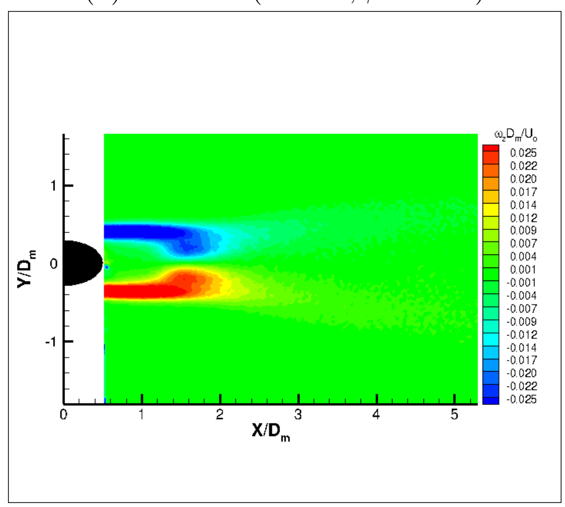

(d) Model D ($\alpha = -5°$, $\beta = -5°$)

Figure 45: Normalized ω_z vorticity fields in the wake of whisker models A-D (Trough cross section x-y plane)

Model D has two arms of high ω_z. The positive rotation arm is located below the model centerline and extends to 2.2 X/D_m downstream. The negative rotation arm is located above the model centerline and extends to 2.2 X/D_m downstream. The remained of the ω_z field is relatively small in magnitude.

Figure 46 contains the T_u for the trough cross-sectional plane. Model A has a low T_u region following the model the extends to 1.1 X/D_m downstream. There are two regions of high T_u on either side of the model centerline. These pockets are

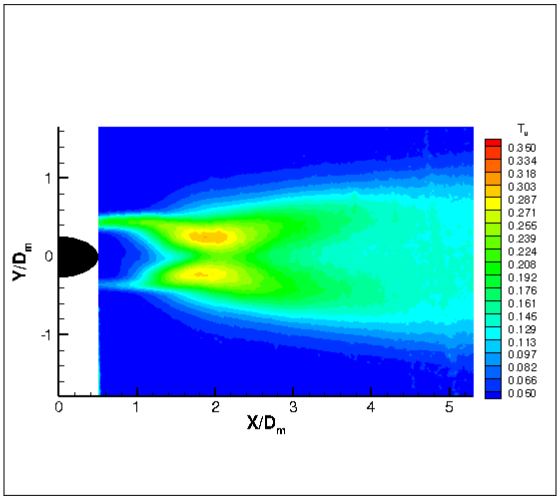

(a) Model A ($\alpha = 0°$, $\beta = 0°$)

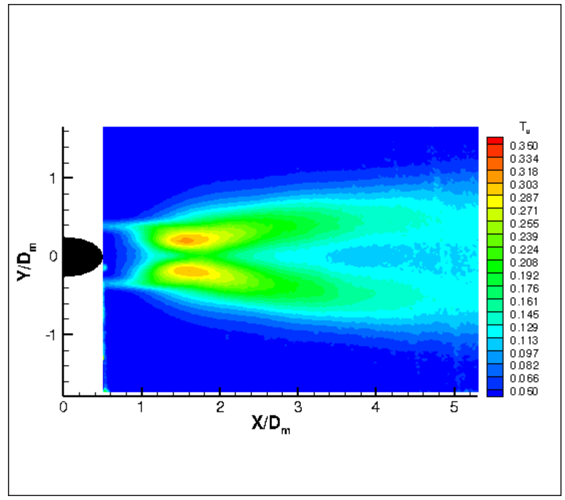

(b) Model B ($\alpha = 5°$, $\beta = -5°$)

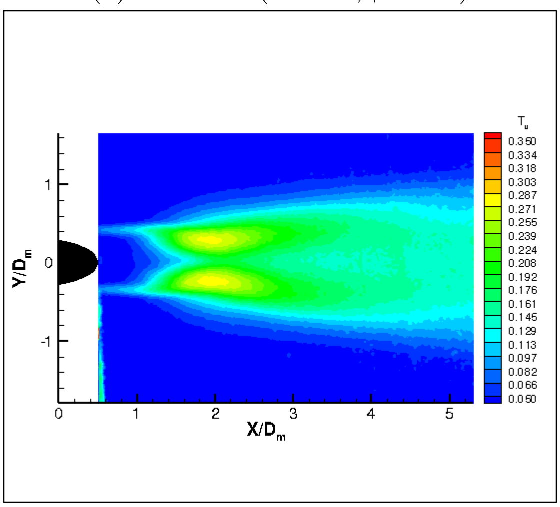

(c) Model C ($\alpha = -15°$, $\beta = -15°$)

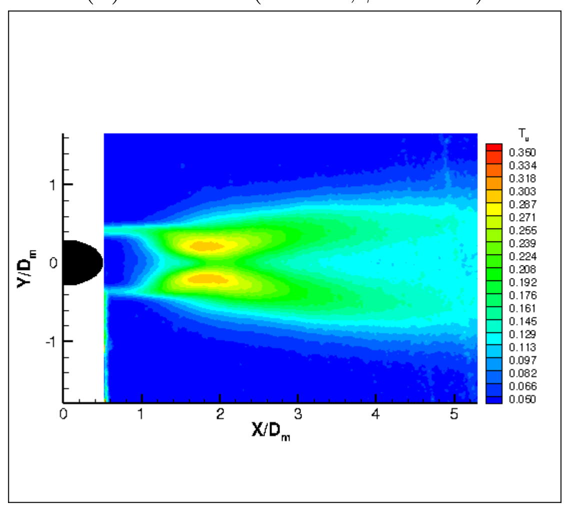

(d) Model D ($\alpha = -5°$, $\beta = -5°$)

Figure 46: Turbulence intensity of u fields in the wake of whisker models A-D (Trough cross section x-y plane)

centered at 1.9 X/D_m and extend from 1.3 to 3 X/D_m downstream. The two pockets are oriented parallel to the model centerline and reach maximum magnitudes near 30% T_u. The remainder of the wake region is defined by T_u 15 to 20% range. The wake expands from the model to width of 2.8 D_m evenly distributed about the model centerline.

Model B has a low T_u region following the model that extends to 0.8 X/D_m downstream. There are two regions of high T_u mirrored about the model centerline.

These regions begin at 1.2 and extend to 2.7 X/D_m. The maximum magnitude of these pockets are located at 1.6 X/D_m and have magnitudes above 30% T_u. The remainder of the wake is characterized by T_u in the 12 to 20% range. The wake of T_u greater than the free stream T_u expands from the model to a maximum width of 2.4 D_m even distributed about the model centerline.

Model C has a low T_u region following the model that extends to 1.0 X/D_m downstream. There are two regions of high T_u mirrored about the model centerline. These regions begin at 1.2 and extend to 2.9 X/D_m. The maximum magnitude of these pockets are located at 1.8 X/D_m and have magnitudes maximizing at 30% T_u. The remainder of the wake is characterized by T_u in the 12 to 20% range. The wake of T_u greater than the free stream T_u expands from the model to a maximum width of 2.7 D_m even distributed about the model centerline.

Model D has a low T_u region following the model that extends to 1.2 X/D_m downstream. There are two regions of high T_u mirrored about the model centerline. These regions begin at 1.5 and extend to 3.0 X/D_m. The maximum magnitude of these pockets are located at 2.0 X/D_m and have magnitudes maximizing at 30% T_u. The remainder of the wake is characterized by T_u in the 15 to 20% range. The wake of T_u greater than the free stream T_u expands from the model to a maximum width of 2.4 D_m even distributed about the model centerline.

Figure 47 displays T_v in the trough cross-sectional plane. Model A has a region of increased T_v beginning at 0.8 X/D_m. Along the centerline there is a region of high reaching a maximum of near 40% T_v. The region of T_v greater than 30% extends from 1.5 to 5.2 X/D_m. The width of the wake the experiences T_v greater than the free stream conditions expands from 0.8 X/D_m having a width at the edge of the measurement window of 3.2 D_m.

Model B has a region of increased T_v beginning at 0.5 X/D_m just connecting

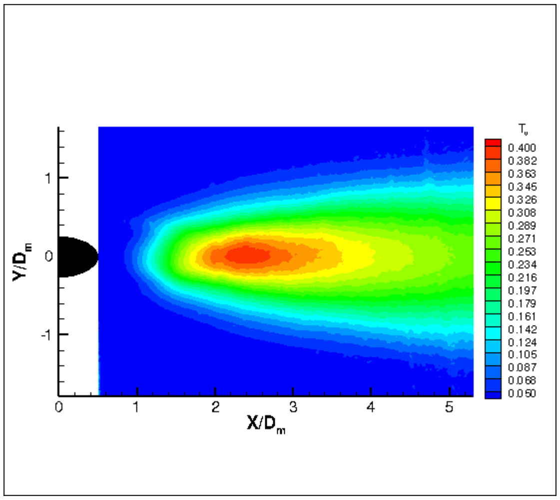

(a) Model A ($\alpha = 0°$, $\beta = 0°$)

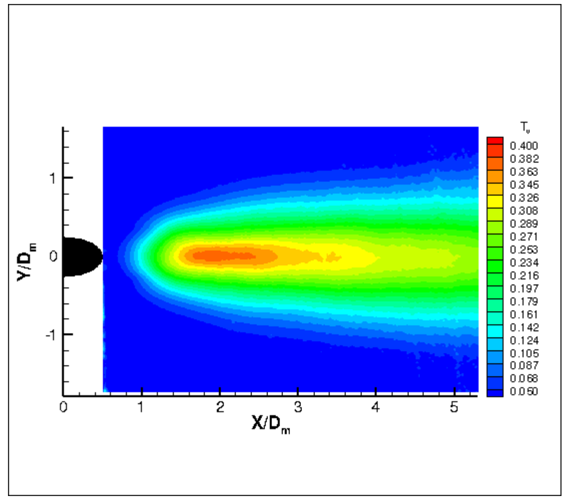

(b) Model B ($\alpha = 5°$, $\beta = -5°$)

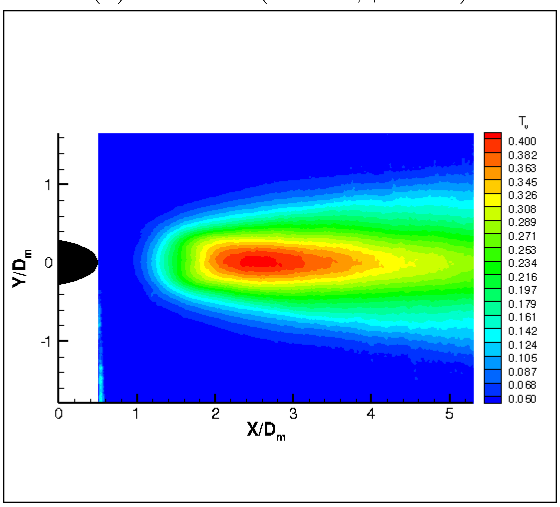

(c) Model C ($\alpha = -15°$, $\beta = -15°$)

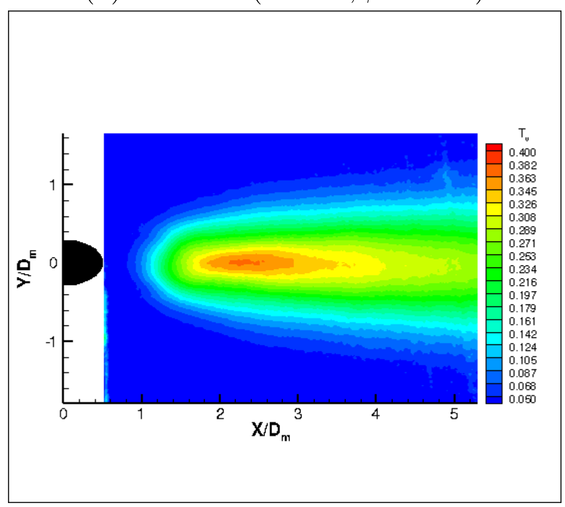

(d) Model D ($\alpha = -5°$, $\beta = -5°$)

Figure 47: Turbulence intensity of v fields in the wake of whisker models A-D (Trough cross section x-y plane)

with the whisker model. Along the centerline there is a region of high intensity reaching a maximum of near 40% T_v. The region of T_v greater than 30% extends from 1.3 X/D_m to beyond the measurement window of 5.8 X/D_m. The width of the wake the experiences T_v greater than the free stream conditions expands from 0.5 X/D_m having a width at the edge of the measurement window of 2.8 D_m.

Model C has a region of increased T_v beginning at 0.7 X/D_m. Along the centerline there is a region of high intensity reaching a maximum of near 40% T_v.

The region of T_v greater than 30% extends from 1.3 to 5.8 X/D_m. The width of the wake the experiences T_v greater than the free stream conditions expands from 0.7 X/D_m having a width at the edge of the measurement window of 3.2 D_m.

Model D has a region of increased T_v beginning at 0.9 X/D_m. Along the centerline there is a region of high intensity reaching a maximum of near 40% T_v. The region of T_v greater than 30% extends from 1.7 X/D_m to beyond 5.3 X/D_m the edge of the measurement window. The width of the wake the experiences T_v greater than the free stream conditions expands from 0.9 X/D_m having a width at the edge of the measurement window of 2.8 D_m.

Figure 48 shows the Reynolds shear stress in the *x-y* plane for the peak cross-sectional measurement plane. Model A shows a region of high τ''_{xy} centered at 2.2 X/D_m. Negative τ''_{xy} is located on the positive *y-axis* and positive τ''_{xy} is located in the negative *y-axis*. The regions of non-zero τ''_{xy} begin at 1.2 X/D_m and extend to 4.8 X/D_m.

Model B shows a region of high τ''_{xy} centered at 2 X/D_m. Negative τ''_{xy} is located on the positive *y-axis* and positive τ''_{xy} is located in the negative *y-axis*. The regions of non-zero τ''_{xy} begin at 1.4 X/D_m and extend to 4.8 X/D_m.

Model C shows a region of high τ''_{xy} centered at 2.2 X/D_m. Negative τ''_{xy} is located on the positive *y-axis* and positive τ''_{xy} is located in the negative *y-axis*. The regions of non-zero τ''_{xy} begin at 1.4 X/D_m and extend to 5 X/D_m.

Model D shows a region of high τ''_{xy} centered at 2.2 X/D_m. Negative τ''_{xy} is located on the positive *y-axis* and positive τ''_{xy} is located in the negative *y-axis*. The regions of non-zero τ''_{xy} begin at 1.4 X/D_m and extend to 5.2 X/D_m.

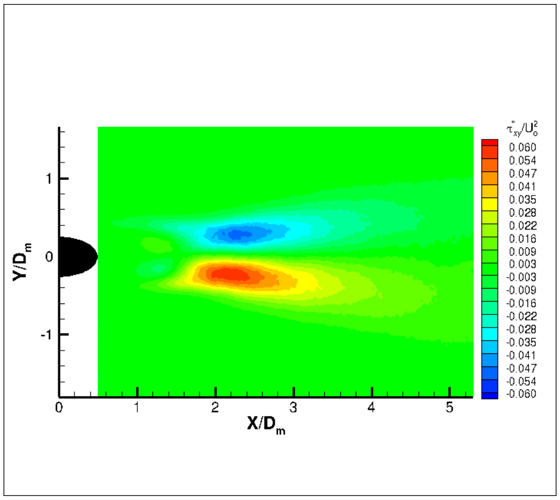

(a) Model A ($\alpha = 0°$, $\beta = 0°$)

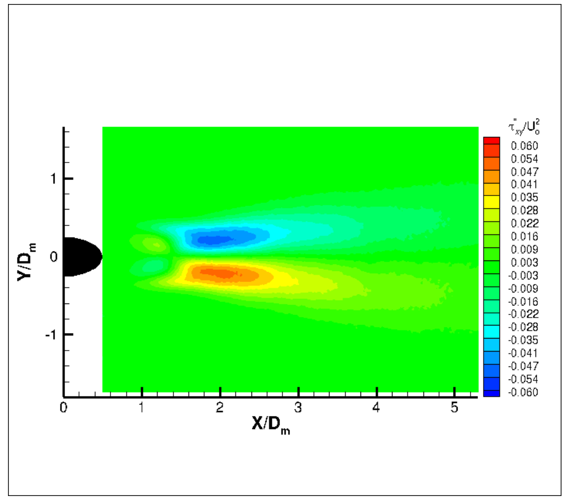

(b) Model B ($\alpha = 5°$, $\beta = -5°$)

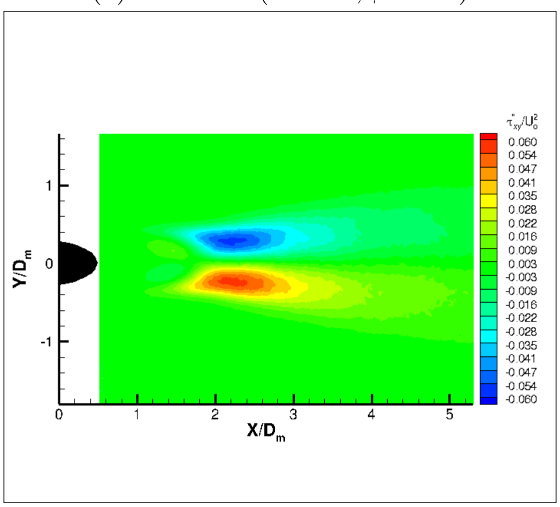

(c) Model C ($\alpha = -15°$, $\beta = -15°$)

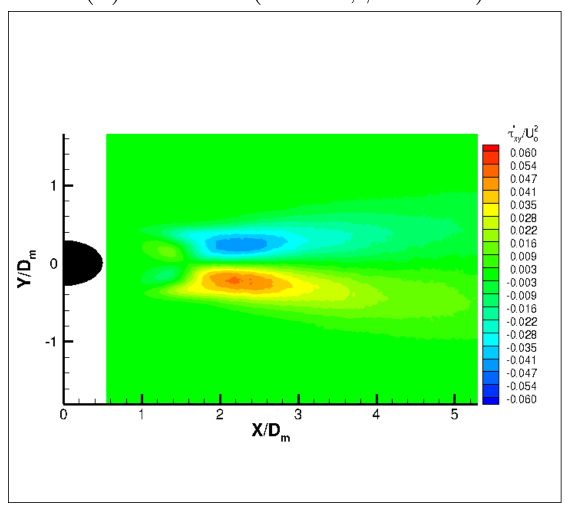

(d) Model D ($\alpha = -5°$, $\beta = -5°$)

Figure 48: Reynolds shear stress fields in the wake of whisker models A-D (Trough cross section x-y plane)

3.4 Comparison to Literature

A brief comparison to some of the results for similar studies in literature will be provided within this section to provide additional confidence to or results as well as highlight observations unique to this study. The work conducted by Wang et al. utilized a very similar test setup using a PIV measurement technique that captured wake data in similar measurement planes behind circular, elliptical, wavy and whisker-like cylinders [70]. While the setup of the experiment is very similar there are a couple of key features that are different between studies. First the non-dimensional parameter used by Wang et al. is the hydraulic diameter, D_h, which is defined in Eq. 3.22. Where the circumference of the ellipse cross section is approximated by Eq. 3.20 since there is no closed form solution of the elliptical integrals available an approximation provided by Ramanujan is utilized [55].

$$C \approx \pi(a+b)(1+\frac{3\frac{(a-b)^2}{(a+b)^2}}{10+\sqrt{4-3(\frac{(a-b)^2}{(a+b)^2})}}) \tag{3.20}$$

$$A = \pi ab \tag{3.21}$$

$$D_h = \frac{4A}{C} \tag{3.22}$$

Results presented within this section will use the D_h nondimensionalization to provide an easier comparison between studies. The second geometry difference is found in the spacing relationship of the undulations this study has a $\lambda/D_h = 7.28$ where the Wang study used $\lambda/D_h = 2.84$. The last significant difference observed is $Re_{Dh} = 1.8 \times 10^3$ which is significantly higher than this study at $Re_{Dh} = 300$. The influence of these differences is not well documented and no definitive statements will be made about the differences in wake structures as that is not the focus of this paper.

A comparison of the vertical centerline u velocity field in Fig. 49 shows near wake patterns. Figure 49a shows two results from Want et al., c is the wavy circular cylinder and d is the whisker-like geometry. The plots display normalized u velocity contours with velocity vectors overlaid with flow entering at the top of figure and exiting the bottom. The whisker models are depicted as black and grey shapes as viewed in profile at the top of the figures. The analogous plot is provided in Fig. 49b using the same color contour mapping. The general near wake structure is comparable between the two whisker-like geometries. Flow recovers with the shortest distance behind the peak location and longer behind the trough location. The strongest recirculation zones reside behind trough locations. It is noted that the results shown by Wang et al. have a much longer near wake with flow less than $\overline{u}/U_o = 0.5$ extending to 4 X/D_h nearly double what is observed in our study. The velocity field for the Wang et al. data caps color contour at $\overline{u}/U_o = 0.5$ and only extends to $6 = x/D_h$, this makes far wake comparisons are not possible between these data sets.

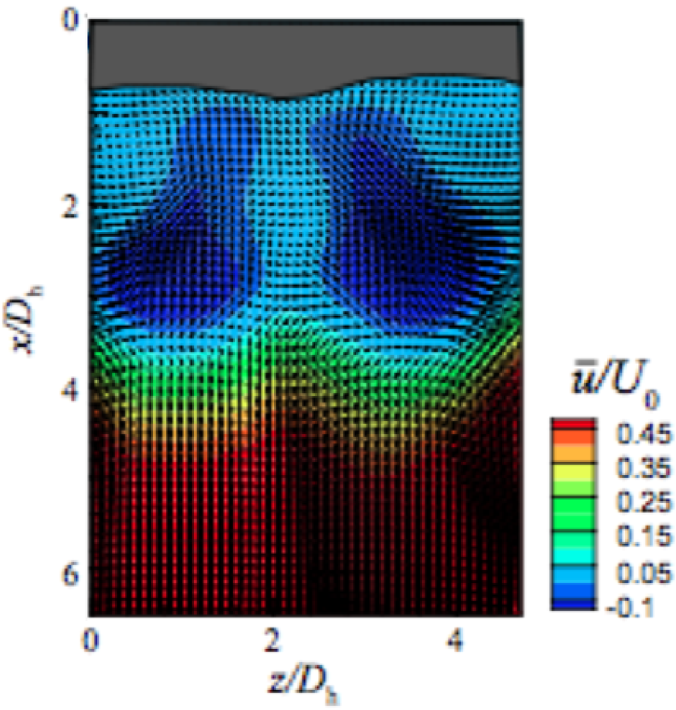

(a) Vertical centerline measurement plane for $\overline{u}/U_o$
Whisker-like geometry ($\alpha = -15.27°$, $\beta = -17.6°$) [70]

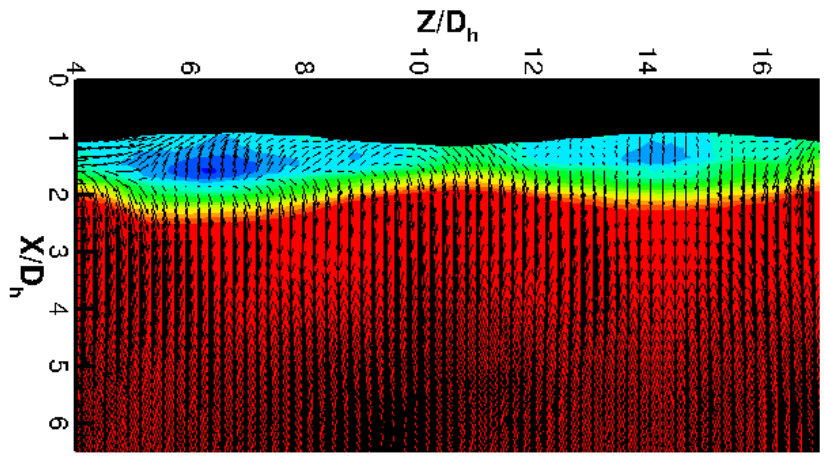

(b) Model C ($\alpha = -15°$, $\beta = -15°$)

Figure 49: Vertical centerline measurement plane for $\overline{u}/U_o$ profiles. Comparing Wang et al. compared to Model C of current study

Figure 50 shows the normalized velocity fields at peak and trough cross sectional planes. Flow is entering from left and exiting on the right. Whisker-like models are depicted by black and grey ellipses on the left of the figures. Figures 50b and 50c were generated with the same contour mapping as those used by Wang et al. The wake structures are comparable for both studies. The peak cross section plane shows a shorter recirculation zone when compared to the trough cross section plane for both studies. The Wang et al. study shows longer wakes for both peak and trough cross section planes.

Overall a brief comparison of the u velocity fields in the vertical and horizontal measurement planes show similar results for the wake structure. There are some differences in wake size between the studies this might be attributed to the difference in undulation spacing or the Re_{Dh} differences and could be interesting areas of further study in understanding the different roles the whisker morphology plays in the wake structure.

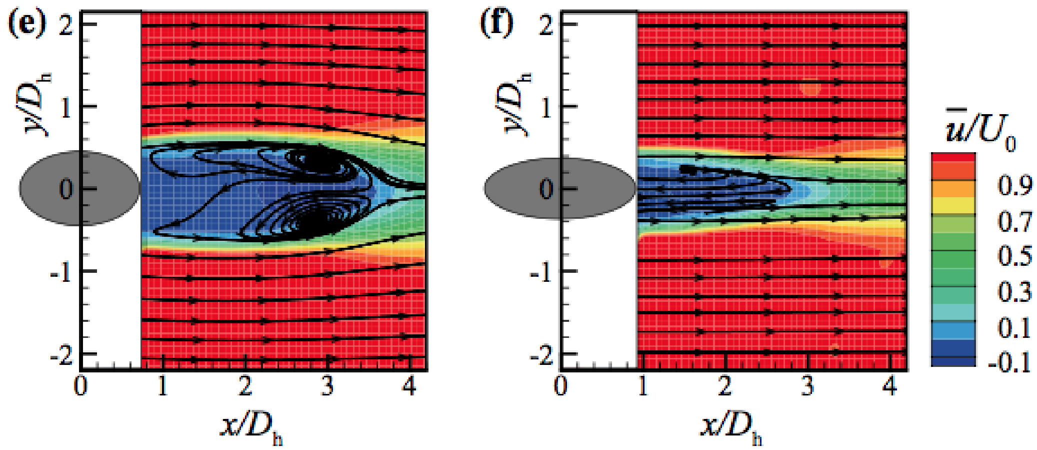

(a) Horizontal cross sectional planes (left trough and right peak) $\overline{u}/U_o$, ($\alpha = -15.27°$, $\beta = -17.6°$) [70]

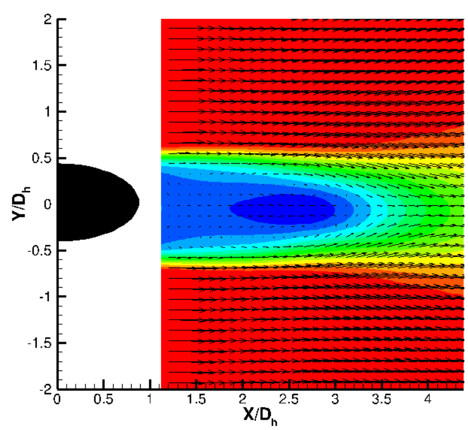

(b) Trough Model C ($\alpha = -15°$, $\beta = -15°$)

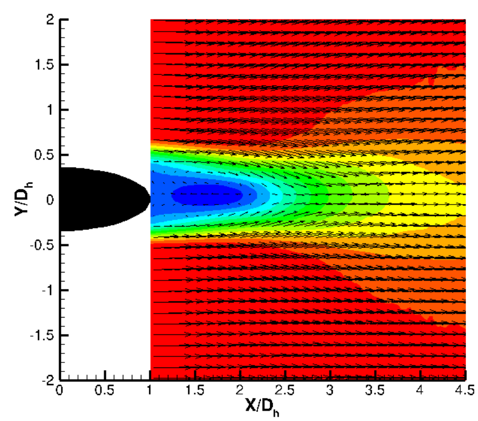

(c) Peak Model C ($\alpha = -15°$, $\beta = -15°$)

Figure 50: Comparison of $\overline{u}/U_o$ fields in the peak and trough horizontal planes to Wang et al. [70]

3.5 Discussion

In the previous chapter results of the the angle of incidence affect on the wake structure was presented. In this section further elaboration and analysis on the differences in wake structure between the models will be provided as well as a summary the key finds of this flow study.

3.5.1 Mean u Velocity Field

Common to all of the models in the near wake, less than 3 D_m, was the pattern of higher u velocities behind the peak geometries of the whisker models and lower velocities behind the trough geometries. The angle of incidence was shown to alter the velocity field beyond 3 D_m downstream of the whisker model. This was most pronounced in the $-15°$ model where the pattern of peak locations correlating with short recovery distances seen in the $0°$ model was reversed and short recovery distances were found to relate with the trough locations for the $-15°$ model. The $\pm 5°$ model showed an overall reduction in the recovery distance, either maintaining the distance of recovery seen in the $0°$ model in the peak locations or reducing in the trough locations. The pronounced pattern of alternation between short and longer recovery distances is not observed in the $-5°$ or $\pm 5°$ model instead a more even velocity distribution is observed along the length of the whisker model. It is also observed that the inclusion of any non-zero angle of incidence reduces the region of reverse flow as well as the near wake.

For the peak cross-sectional measurement plane a difference observed in the non-zero angle of incidence models is the far wake slowing of the flow in the wake of the models. Around 4 D_m all non-zero angle of incidence models show a reduction in the u velocity to various extents. This reduction in velocity is not observed in the $0°$ model where the flow exhibits a more traditional recovery pattern. This suggests that there is more shifting in the far velocity field when a non-zero angle of incidence in introduced to the model. The $\pm 5°$ shows the largest reduction in the in the reversed flow region in both magnitude and length.

In the trough cross-sectional measurement plane the $\pm 5°$ model shows a reduction length of the reversed flow region ending near 1.6 D_m the other models show reverse flows extending to 2 D_m. The flow also experiences faster recovery behind the $-5°$ and$\pm 5°$ models. Unfortunately some of the features observed in the far wake with the vertical centerline measurement plane are cannot be compared to the cross-sectional planes here due to the limited field of view. Some of the shifts in pattern shown between the $0°$ and $-15°$ model do not appear until distances greater than 6 D_m downstream of the model. The trough shows a larger region of accelerated flow around the model that is not observed in the peak cross-sectional plane.

3.5.2 Turbulence Intensity of u Velocity

For the vertical centerline measurement plane the T_u distribution is common for all four models in the near wake region. This is characterized by a lower intensity immediately following the model followed by a band of higher T_u located at 2 D_m downstream. This band observed in the vertical plane can be more clearly understood in the horizontal cross-sections and the peaks and troughs as a pocket of high T_u resides along either side of the model centerline. There is roughly 0.6 mm between the low intensity along the centerline and the maximum turbulence intensity. Any slight shift in the alignment of the laser light sheet and the model would result in variation in the T_u along the length of the whisker model. One of the more distinct differences between the models in the vertical plane is that the $0°$ model has a region of notably lower T_u within 1 D_m downstream of the model. Another difference seen comparing the non-zero angle of incidence models is the variation in the bands of 20%

T_u The non-zero models show some deviation from the horizontal pattern observed in the 0° model; however, these do not appear to be explicitly tied to the angle of incidence.

In the peak cross-sectional measurement plane the non-zero angle of incidence models show higher magnitudes of turbulence intensity in the two pockets of high turbulence intensity on either side of the model centerline. In addition introduction of nonzero angle of incidence results in a reduction in T_u starting at 2 X/D_m downstream expanding along the centerline. The reduction in T_u is most pronounced in model B and D. In the trough cross-sectional measurement plane the turbulence intensity for the trough cross-sectional plane shows a significant reduction in the model B in the near wake, where the region of low intensity is cut nearly in half when compared to the model A. The magnitude of the pockets of high intensity are also greatest in model B. Model C shows a slight extension of the low intensity region when compared to the model A which is due to some stretching that occurs from $\beta = -15°$. Both models B and D show a shift forward in the location of the high intensity regions when compared to the models A and C with the model B experiencing the largest shift upstream.

3.5.3 Mean v Velocity Field

No strongly distinguishing features appear in the peak cross-sectional measurement plane among the different models. The ±5° model shows a slight shift upstream in the location of the non-zero v velocity components. Non-zero v velocity are only found in the near wake and quickly dissipated beyond 2 D_m. For trough cross-sectional measurement plane the v velocity the ±5° model shows a the regions of high v shifting upstream to the whisker model occurring near 1.6 X/D_m where as the other models show maximum v occurring at 2 D_m downstream of the model.

3.5.4 Turbulence Intensity of *v* Velocity

For the peak cross-sectional measurement plane the T_v remains relatively consistent among the different models with modest shifts in how far regions of higher T_v extend downstream with the $-5°$ model having the longest region reaching to 5 X/D_m downstream followed closely by the $-15°$ model at 4.8 X/D_m. This is most likely due to the planes being taken at the same height and both the $-5°$ and $-15°$ model show smearing from the trough location to the peak location.

The region of highest T_v is dependent on the angle of incidence. The $\pm5°$ model shows high regions of T_v occurring as early as 1.5 D_m downstream of the model where those same values are not observed in the $0°$ model until 2 D_m downstream. The length of the high intensity region extends in the $-15°$ the furthest reaching 4 D_m downstream where the $0°$ model begins to experience reduction near 3.5 D_m. Both the $-5°$ and $\pm5°$ models experience even more pronounced reductions where the high T_v begin at 3 D_m and 2.6 D_m respectively.

3.5.5 Vorticity

Common to all of the models is the pattern of in plane rotation occurring at the top half of the peak and the bottom half of the trough with out of plane rotation occurring at the bottom half of the peak and the top half of the trough. One of the most pronounced differences among the models generation of ω_y is the greatly reduced distance for the $\pm5°$ model to dissipate the coherent structures. It should also be noted that these high regions of vorticity are provide a critical role in the development of strong vortices developing near the model about the *z-axis*. The other difference between model observed is that the $0°$ case shows that the structures of ω_y maintain patterns perpendicular to the vertical axis of the whisker model. The other models that posses non-zero angle of incidence values show some tendency for these ω_y structures to follow the angle of incidence.

For the both the peak and trough locations ω_z characteristics remain very similar among the four models. Regions of high vorticity are confined to less than 2 D_m downstream in very uniform patterns wrapping around and behind the model cross section. In the trough cross section models B shows a reduction in the distance the symmetric arms of vorticity extend downstream.

3.5.6 Reynolds Shear Stress

Common to all models is a region of high $\tau^{''}_{xy}$ and $\tau^{''}_{xz}$ located at 2 X/D_m. This indicates momentum transfer in the y and z directions in the near wake for all models. In the x-z plane a notable reduction in the size and magnitude of the positive $\tau^{''}_{xz}$ regions was observed in model C suggesting that with a sufficiently large angle of incidence the far wake can be momentum transfer can be altered.

A noted difference between the momentum transfer in the x-z plane and the x-y plane is that there does not appear to be a far wake pattern in the x-y plane that is observed in the x-z plane. Suggesting that the y momentum transfer is focused to the near wake and the z momentum transfer occurs in the near and far wake.

In the peak and trough cross-sectional planes the patterns of $\tau^{''}_{xy}$ are very similar between all four models. The peak cross-sectional planes have non-zero regions closer to the model contributing to the shorter recovery length noted inline with the peak locations.

CHAPTER IV

Conclusions

The aim of this research was to provide a more comprehensive understanding of the morphology of beaded seal whisker geometry in regard to the angle of incidence. Based on those findings study the effect that the angle of incidence has on the wake structure. Through the analysis of 27 harbor and elephant seal whiskers it was observed that the majority of the angle of incidence *alpha* and *beta* posses angles that fall within $\pm 5°$. The variation in the magnitude and direction of the angle of incidence does not correlate to the axial position on the whisker nor does there appear to be any coherent pattern along the length of the whisker. These findings are in strong agreement with the limited data sets publicly known to the author at the time of research and help to provide a strong case for the characterization of the angle of incidence found in both the harbor and elephant seal with expectations that other beaded seal would exhibit similar trends. From these trends a design foundation can be obtained and applied as a baseline to engineering applications looking to emulate the ability of the seal whisker either for enhanced sensitivity in flow sensor design or obtaining performance enhancements in drag reduction applications like airfoil design and offshore oil rig struts.

In addition to this finding is was observed that prior research of scaled up seal whisker models and computation models investigating the wake structure of the beaded seal whiskers focused on a very limited set of angles that find their origin with Hake et al. [5, 29, 32, 65]. While these angles of incidence fall within observed angles found in nature they are on the extreme edges of those found in nature.

The work conducted within this study looked at angles of α and β ranging from $0°$ to $15°$. Attempting to cover the rang observed within nature as well as investigate the direction of the angle as well as the magnitude of the angle of incidence. The four models used possessed the following angle of incidence; $\alpha = \beta = 0°$; $\alpha = \beta = -5°$, $\alpha = \beta = -5°$, and $\alpha = 5°$ $\beta = -5°$. From these models and the resulting flow studies it was observed that the angle of incidence can produce a significant effect on the flow structure. These effects can be summarized by; a re-organization of the pattern of velocity field, reduction in the distance required for velocity to recover, and enhanced mixing in the near and far wake with the inclusion of nonzero angle of incidence. These three functions of the angle of incidence are most clearly observed in the following cases.

Comparing u velocity field along the vertical centerline plane in the $0°$ to the $-15°$ model and observing a complete switch with peaks recovering fastest in the $0°$ case to slowest in the $-15°$ model.

The overall reduction of distance required for fully recovered u velocity field most notably observed in vertical centerline plane as well as the trough cross-sectional planes when comparing the $\pm 5°$ to the $\pm 0°$ case. In the trough cross-sectional plane a 27% reduction in the recovery length was observed from model A to model B.

Finally the enhanced mixing could be observed in the removal of the strongly ordered u field observed in both the $0°$ and $-15°$ in the vertical centerline plane that is not observable in the $\pm5^{\circ}$ model. The reduction in the low T_u zone following the model observed in the $\pm5^{\circ}$ at the trough cross-section also adds to the final finding of enhanced mixing.

From these results it can be understood that an intelligently designed whisker like geometry can provide enhanced performance advantages over a typical whisker observed in nature. Namely this study found that an alternation of direction for α and β can provide substantial performance gains.

CHAPTER V

Future Work

This research effort has identified some of the way the angle of incidence can affect the wake structure. Based on the results of this study there are a number of areas where this work could be expanded to more thoroughly understand the role the angle of incidence has on the flow structures.

One observation follows from the 3D printing used in building the whisker models. Due to the small scale of the models and the resolution of the 3D printers small ridges were present marking the layers of material. These ridges were minimized with the black paint that was applied to the printed models; however, the ridges were still present. It was determined that attempting to smooth the surface of the model by sanding may alter the geometry and distort the different angle of incidence features that are being studied. It is also unknown how sensitive the whisker geometry is to surface roughness. Additional testing could be conducted with various surface smoothness. Particularly tests could be conducted with circular cylinders of various surface roughness and compared against known flow structures in the wake region of a circular cylinder.

Another area of extension would be range of angle of incidence. The angles of incidence chosen in this study were bounded by observations found for the whiskers measures. Further experiments could be conducted to identify the range of effective angle of incidence and see if the angles observed in nature are reflective of the limit of effectiveness or if more extreme magnitudes could yield additional gains in control and ordering of the wake flow.

Another area that has not been bounded is the geometry dependency on Reynolds number. This study was conducted at a single Reynolds number of 630 based on the Reynolds number harbor seals are known to operate at. Understanding the range of Reynolds numbers where this geometry can be effective is critical for any future attempts to use whisker like geometry for engineering applications.

Another area that would help define where this morphology could be applied is related to the upstream flow conditions. This experiment were relatively well behaved with a mean T_u near 5%, applying this geometry to engineering applications it could be expected that the incoming flow would not be as well conditioned. Conducting experiments over a range of turbulence intensity flow could provide valuable information on the types of environments this geometry would be effective.

The flow structures in the wake are highly three dimensional and this study was limited to capturing single planes with two of the three velocity components. The ability to collect data in the vertical plane that is perpendicular to the major axis of the whisker model would be a simple first step to further round out the velocity features of the whisker geometry. Due to the highly three dimensional nature of the wake structure it would be most ideal to utilize a 3D PIV system to capture a volume behind the whisker allowing for a more complete resolution of how the geometry influences the wake structure.

Further more additional experiments conducted with air as the fluid would be helpful in determining if the whisker geometry has sensitivity to the viscous properties of the fluid it operates in as well.

The whisker geometry provides an very rich opportunity for optimization as well. Due to the complex 3D nature of the geometry it can be easily envisioned that future studies focus on optimizing the seven geometry features defining the whisker geometry with the understanding that different applications may require unique optimization.

The options for expanding and continuing this research listed above are admittedly a small sampling as this area of study is still relatively new many opportunities for study may still be unknown.

BIBLIOGRAPHY

[1] 3D Computed Tomography, North Star Imaging Inc., 2008.

[2] A.S. Ahl, The roe of vibrissae in behavior: a status review, *Veterinary research communications*, 10(1): 245-268, 1986.

[3] Asylum MFP-3D-BIO Atomic Force Microscope, Asylum Research Inc., 2015.

[4] MD Abramoff, P.J. Magalhaes, S.J. Ram, *'Image Processing with ImageJ'*, Biophotonics International, 11(7): 36-42, 2004.

[5] H. Beem, Passive Wake Detection Using Seal Whisker-Inspired Sensing, PhD Dissertation, Joint Program in Oceanography and Applied Ocean Sciences and Engineering, MIT and WHOI, Cambridege, Mass. 2015.

[6] M. Brambilla, E., Ferrante, M. Birattari, M. Dorigo, Swarm Robotics: a review from the swarm an engineering perspective, *Swarm Intelligence* 7, 2013.

[7] M. Castillo, The Industry of CT Scanning, *The American Journal of Neuroradiology*, 33: 583-585, 2012.

[8] C. Creton, S. Gorb, Sticky Feet: from Animals to Materials *Materials Research Society Bulletin*, 32(6): 466:472, 2007.

[9] E. DeArmon, M. Stone, E. Rogenski, D. Thurman, P. Poinsatte, V. Shyam, Characterization and Analysis of Phoca Vitulina, Zalophus Californianus and Mirounga Angustirostis Vibrissae, NASA Technical Manual, (pending publication).

[10] G. Dehnhardt, B. Mauck, W. Hanke, H. Bleckmann, Hydrodynamic trail following in harbor seals (*Phoca vitulina*). *Science* 293: 102-104, 2001.

[11] G. Dehnhardt, A. Kaminski, Sensitivity of the mystacial vibrissae of the harbour seals (*Phoca vitulina*) for size differences of actively touched objects, *Journal of Experimental Biology*, 198(11): 2317-2323, 1995.

[12] G. Dehnhardt, Preliminary results from psychophysical studies on the tactile sensitivity in marine mammals, *Sensory Abilities of Cetaceans* pp. 435-446, Springer, 1990.

[13] G. Dehnhardt, Tactile size discrimination by a california sea lion (*Zalophus californianus*) using its mystacial vibrissae. *Journal of Comparative Physiology*, 175(6): 791-800, 1994.

[14] G. Dehnhardt, M. Sinder, N. Sachser, Tactual discrimination of size by means of mystacial vibrissae in harbour seals: in air versus underwater. *Zeitschrift fur Saugetierkunde*, 62: 298-304, 1997.

[15] M. H., Dickinson, F. O. Lehmann, S. P. Sane, Wing rotation and the aerodynamic basis of insect flight, *Science*, 284, 1954-1960. 1999.

[16] R. Dudley, C.P. Ellington, Mechanics of Forward Flight in Bumblebees I. Kinematics and Morphology, *Journal of Experimental Biology*, 148: 19-52, 1990.

[17] R. DUDLEY, C. P. ELLINGTON Mechanics of Forward Flight in Bumblebees: II. Quasi-Steady Lift And Power Requirements, *Journal of Experimental Biology*, 148: 53-88, 1990.

[18] R.W. Dykes, Afferent fibers from mystacial vibrissae of cats and seals, *Journal of Neurophysiology*, 38(3): 650-662, 1975.

[19] F. Fish, P. Weber, M. Murray, L. Howel, The Tubercles on Humpback Whales' Flippers: Application of Bio-Inspired Technology *Oxford Journals*, 50(1): 203-213, 2011.

[20] S. M. Gatesy, D. B. Baier, The origin of the avian flight stroke: a kinematic and kinetic perspective. *Paleobiology*, 31: 382-399, 2005.

[21] Gill, F. B. Hummingbird flight speeds. *Auk: Ornithological Advances*, 102: 97-101. 1985.

[22] C. Ginter, F. Fish, C. Marshall, Morphological analysis of the bumpy profile of phocid vibrissae, *Marine Mammal Science*, 26: 733-743, 2010.

[23] C. Ginter, T. DeWitt, F. Fish, C. Marshall, Fused Traditional and Geometric Morphometerics Demonstrate Pinniped Whisker Diversity *PLoS ONE*, 7(4), 2012.

[24] C. Ginter, S. Ingole, F. Fish, C. Marshall, Comparative Analysis of Flexural Stiffness of Pinniped Vibrissae, *PLoS ONE*, 10(7), 2015.

[25] N. Glaser, B. Mauck, F. Kandil, M. Lappe, G. Dehnhardt, F. Hanke, Harbor Seals (Phoca vitulina) Can Perceive Optic Flow Under Water, *PLoS ONE*, 9(7), 2014.

[26] N. Glaser, S. Wieskotten, C. Otter, G. Dehnhardt, W. Hanke., Hydrodynamic trail following in a california sea lion (*Zalophus californianus*), *Journal of Comparative Physiology A: Neuroethology, Sensory, Neural, and Behavioral Physiology*, 197: 141-151, 2011.

[27] D.K. Greaves, M.O. Hammill, J.D. Eddingtion, D. Pettipas, J.F. Schreer, Growth rate and shedding of vibrissae in gray seal, *Halichoerus Grypus*: A cautionary note for stable isotope diet analysis. *Marine Mammal Science*, 20(2);296-304, 2004.

[28] Greenewalt, C. H. The wings of insects and birds as mechanical oscillators, *Proceedings of the American Philosophical Society* 104, 605-611, 1960.

[29] W. Hanke, M. Witte, L.I. Miersch, M. Grede, J. Oeffner, M., Michael, F. Hanke, A. Leader, G. Denhardt, Harbor Seal Vibrissae Morphology Suppresses Vortex-Induced Vibrations, *The Journal of Experimental Biology* 213: 2665-2672, 2010.

[30] W. Hanke, H. Bleckmann, The hydrodynamic trails of *Lepomis gibbosus* (centrarchidae), *Colomesus psittacus* (tetraodontidae) and *Thysochromis ansorgii* (cichlidae) investigated with scanning particle image velocimetry. *Journal of Experimental Biology*, 207(9): 1585-1596, 2004.

[31] W. Hanke, C. Brucker, H. Bleckmann. The ageing of the low-frequency water disturbances caused by swimming goldfish and its possible relevance to prey detection, *Journal of Experimental Biology*, 203(7):1193-1200, 2000.

[32] H. Hans, J. Miao, M. Triantafyllou, G. Weymouth, Whisker-like Geometries and Their Force Reduction Properties, *OCEANS MTS/IEEE Conference*, 2013.

[33] H. Hans, J.M. Miao, M.S. Triantafyllou, Mechanical characteristics of harbor seal (*Phoca vitulina*) vibrissae under different circumstances and their implications on its sensing methodology, *Bioinspiration & biomimetics*, 9(3), 2014.

[34] K. L. Hansen, R.M. Kelso, B.B. Dally, Performance Variations of Leading-Edge Tubercles for Distinct Airfoil Profiles, *Journal of Aircraft*, 49(1): 185-194, 2011.

[35] A.C. Hirons, D.M. Schell, D.J. St. Aubin, Growth rates of vibrissae of harbor seals (Phoca vitulina) and stellar sea lions (Eumetopias jubatus), *Canadian Journal of Zoology*, 79(6): 1053-1061, 2001.

[36] H. Hyvariene, "Diving in darkness: whiskers as sense organs of the ringed seal (Phoca hispida saimensis)", *Journal of Zoology*, 218(4): 663-678, 1989.

[37] H. Hyvarinen, On the histology an histochemistry of the snout and vibrissae of the common shrew (Sorex araneus), *Zeitschrift fur Zellforschung und Mikroskopische Anatomie*, 124(4): 445-453, 1972.

[38] H. Hyvarinen, H. Katajisto, Functional strucutre of the vibrissae of the ringed seal (Phoca hispida schr.), *Acta Zoologica Fennica*, 171: 17-30, 1984.

[39] Some Experiments on Navigation in the Harbour Seal, Phoca vitulina, Animal Migration, Navigation, and Homing, 7: 395-404, 1978.

[40] H. Johari, C. Henoch, D. Custodio, A. Levshin, Effects of Leading-Edge Protuberances on Airfoil Performance, *AIAA Journal*, 45(11): 2634-2642, 2007.

[41] R.A. Kastelein, M.A. Van Gaalen, The sensitivity of the vibrissae of a pacific walrus (*Odobenus rosmarus divergem*), *Aquatic Mammals*, 14: 123-133, 1988.

[42] A. Kesel, Aerodynamic Characteristics of Dragonfly Wing Sections Compared to Technical Airfoils, *Journal of Experimental Biology*, 203: 3125-3135, 2000.

[43] J. E., King, Seals of the World, Ithaca: Cornell University Press 1983.

[44] J. Kruyt, E. Quicanzan-Rubio, G. Heijst, D. Altshuler, D. Lentink, Hummingbird wing efficacy depends on aspect ratio and compares with helicopter rotors, *Journal of Royal Society of Interface*, 11(99), 2014.

[45] Y.F. Lin, H.L. Bai, Md. Mahbub Alam, W.G. Zhang, K. Lam, Effects of large spanwise wavelength on the wake of sinusoidal wavy cylinder, *Journal of Fluids and Structures*, 61: 392-409, 2016.

[46] J. K., Ling, Vibrissae of marine mammals, *Functional anatomy of marine mammals*, London: Academic Press, pp. 387-415, 1977.

[47] E. A. van Nierop, S. Alben, M. P. Brenner, How Bumps On Whale Flippers Delay Stall: An Aerodynamic Model, *Physical Review Letters*, 100(5):054502, 2008.

[48] K.M. Madden, L.A. Fuiman, T.M. Williams, R.W. Davis, Weddell seal foraging dives: comparison of free-ranging and isolated-hole paradigms, *Antarctic Science*, 27(1): 57-69, 2015.

[49] D. S. Miklosovic, M. M. Murray, L. E. Howle, F. E. Fish, Leading-Edge Tubercles Delay Stall On Humpback Whale (Megaptera Novaeangliae) Flippers, *Physics of Fluids*, 16, 2004.

[50] F.H. Mills D. Renouf, Determination of the vibration sensitivity of harbour seal, *Phoca vitulina* (l.) vibrissae, *Journal of Experimental Marine Biology and Ecology*, 100(1-3): 3-9, 1986.

[51] C. Murphy, W. Eberhardt, B. Calhoun, K. Mann, D. Mann, Effect of Angle on Flow-Induced Vibrations of Pinniped Whisker Diversity, *PLoS ONE*, 8(4), 2012.

[52] C. Murphy, Structure and Function of Pinniped Vibrissae, PhD Dissertation, University of South Florida, 2013.

[53] G. Oliver, Navigation In Mazes By Grey Seal, Halichoerus grypus (Fabricius), *Behaviour*, 67: 7-114, 1978.

[54] K. Pohlmann, F.W. Grasso, T. Breithaupt, Tracking wakes: the nocturnal predatory strategy of piscivorous catfish, *Proceedings of the National Academy of Sciences*, 98(13):7371-7374, 2001.

[55] Ramanujan, Srinivasa, Modular Equations and Approximations to π, *The Quarterly Journal of Pure and Applied Mathematics*, 45: 350-372, 1914.

[56] C. J. Rees, Aerodynamic properties of an insect wing section and a smooth aerofoil compared, *Nature*, 258: 141-142, 1975.

[57] D. Renouf, Fishing in captive harbor seals. A possible role for vibrissae. *Netherlands Journal of Zoology*, 303: 504-509, 1980.

[58] D. Renouf, Sensory reception and processing in phocidae and otariidae, *The Behaviour of Pinnipeds* pp. 345-394, Springer, 1991.

[59] D. Renouf, L. Gaborko, Speed Sensing in harbour seal, *Journal of Marine Biological Association of the Uniter Kingdom* 62(01): 227-228, 1982.

[60] D. Renouf, Preliminary measurements of the sensitivity of the vibrissae of harbour seals (*Phoca vitulina*) to low frequency vibrations, *Journal of Zoology*, 188(4): 443-450, 1979.

[61] D. Roth, R. Rauser, The Effect of Experimental Variables on Industrial X-Ray Micro-Computer Sensitivity, NASA/TM 2014-218332, NASA Glenn Research Center, 2014.

[62] R. Schafer, What is a Savitzky-Golay Filter?, *IEEE Signal Processessing Magazine*, 28: 111-117, 2011.

[63] L.F. Shatz, T. De Groot, The frequency response of the vibrissae of harp seal, *Pagophilus groenlandicus*, to sound in air and water, *PLoS ONE*, 8(1), 2013.

[64] V.B. Sheffer, J.W. Slipp, The Harbor Seal in Washington State, *American Midland Naturalist*, pp. 373-416, 1944.

[65] V. Shyam, A. Ameri, P. Pointsatte, D. Thurman, A. Wroblewski, C. Synder, Application of Pinniped Vibrissae to Aeropropulsion. *Proceedings of ASE Turbo Expo*, 2015.

[66] R. Elsner, D. Wartzok, N.B. Sonafrank, B.P. Kelly, Behavioral and physiological reactions of arctic seals during under-ice pilotage, *Canadian Journal of Zoology*, 67: 2506-2513 1989.

[67] Stratasys uPrintSE Plus 3D Product Spec. Sheet stratasys, 2016.

[68] M. Thompson , J. Burnett, A. Batra, D. Ixtabalan, D. Tran, A. Rodriguez, B. Steele, Experimental Design of a Flapping Wing Micro Air Vehicle through Biomimicry of Bumblebees AIAA SciTech Conference Proceedings Jan, Florida, 2015.

[69] Vargas, A., Mittal, R. and Dong, H. A computational study of the aerodynamic performance of a dragonfly wing section in gliding flight. *Bioinspiration and Biomimetics*, 3, 026004, 2008.

[70] S. Wang, Y. Liu, Wake dynamics behind seal-vibrissa-shaped cylinder: a comparative study by time-resolved particle velocimetry measurements, *Experimental Fluids*, 53(32), 2016.

[71] P. W. Weber, L. E. Howle, M. Murray, D. S. Miklosovic, Computational Evaluation Of The Performance Of Lifting Surfaces With Leading-Edge Protuberances, *Journal of Aircraft*, 48(2):591-600, 2011.

[72] B. Wieneke, PIV Uncertainty Quantification from Correlation Statistics, *Measurement Science and Technology*, 26(7): 074002-074012, 2015.

[73] W. Zhang, Daichin, S.J. Lee, PIV measurements of the near-wake behind a sinusoidal cylinder, *Experiments in Fluids*, 38: 824-832, 2005.

[74] C. Zeiss, Axio Scope and Axio Imager, Carl Zeiss Microscopy GmbH, 2009.

APPENDIX

APPENDIX A

Ensemble Averaging Code

```
% This code reads the data files and calculates the average quantities of them.

clear all

close all

FileName = 'B';

Nfile=input('Number of files');


StartFile = 1;

str1='VARIABLES=X,Y,U,V';

str2='ZONE I= 127J= 127F=POINT';

str3='VARIABLES=X,Y,Urms,Vrms,Rstress';

strmean=strvcat(str1,str2);

strrms=strvcat(str3,str2);

\% --------------------------

\% Reading files

\% --------------------------
```

```
Umean=0.0;

Vmean=0.0;

Urms=0.0;

Vrms=0.0;

Rstress=0.0;

FileCount=0;


for k=StartFile:StartFile+Nfile-1

if (k < 10)

title_num=['0000',int2str(k)];

title=[FileName,title_num,'.','dat']

[X Y U V]=textread(title,'%f %f %f %f','delimiter',',','headerlines',3);

end


if (k < 100 & k >=10)

    title_num=['000',int2str(k)];

title=[FileName,title_num,'.','dat']

[X Y U V]=textread(title,'%f %f %f %f','delimiter',',','headerlines',3);

end


if (k < 1000 & k >= 100)

title_num=['00',int2str(k)];

title=[FileName,title_num,'.','dat']

[X Y U V]=textread(title,'%f %f %f %f','delimiter',',','headerlines',3);

end
```

```
if (k < 10000 & k >= 1000)
title_num=['0',int2str(k)];
title=[FileName,title_num,'.','dat']
[X Y U V]=textread(title,'%f %f %f %f','delimiter',',','headerlines',3);
end

if (k < 100000 & k >= 10000)
title_num=[int2str(k)];
title=[FileName,title_num,'.','dat']
[X Y U V]=textread(title,'%f %f %f %f','delimiter',',','headerlines',3);
end

FileCount=FileCount+1;
Umean=Umean+U;
Vmean=Vmean+V;
end

Umean=Umean./FileCount;
Vmean=Vmean./FileCount;

% ------------------------------------------------------------------------
% Calculating the flactuations field
% ------------------------------------------------------------------------

for k=StartFile:StartFile+Nfile-1
if (k < 10)
```

```
title_num=['0000',int2str(k)];
title=[FileName,title_num,'.','dat']
[X Y U V]=textread(title,'%f %f %f %f','delimiter',',','headerlines',3);
end

if (k < 100 & k >=10)
title_num=['000',int2str(k)];
title=[FileName,title_num,'.','dat']
[X Y U V]=textread(title,'%f %f %f %f','delimiter',',','headerlines',3);
end

if (k < 1000 & k >= 100)
title_num=['00',int2str(k)];
title=[FileName,title_num,'.','dat']
[X Y U V]=textread(title,'%f %f %f %f','delimiter',',','headerlines',3);
end

if (k < 10000 & k >= 1000)
title_num=['0',int2str(k)];
title=[FileName,title_num,'.','dat']
[X Y U V]=textread(title,'%f %f %f %f','delimiter',',','headerlines',3);
end

if (k < 100000 & k >= 10000)
title_num=[int2str(k)];
title=[FileName,title_num,'.','dat']
```

```
[X Y U V]=textread(title,'%f %f %f %f','delimiter',',','headerlines',3);
end

Uflac=U-Umean;
Vflac=V-Vmean;

Urms=Urms+Uflac.^2;
Vrms=Vrms+Vflac.^2;
Rstress=Rstress+Uflac.*Vflac;

end

Urms=sqrt(Urms./FileCount);
Vrms=sqrt(Vrms./FileCount);
Rstress=Rstress./FileCount;

DataMean=[X Y Umean Vmean];
DataRms=[X Y Urms Vrms Rstress];

TitleMean='MeanVelocity.dat';
dlmwrite(TitleMean,strmean,...
'delimiter','');
dlmwrite(TitleMean,DataMean,...
    'delimiter',' ',...
'-append');
TitleRms='RmsVelocity.dat';
```

```
dlmwrite(TitleRms,strrms,...
'delimiter','');
dlmwrite(TitleRms,DataRms,...
'delimiter',' ',...
'-append');
```

APPENDIX B

Whisker Data

The raw whisker morphology measurements are provided below. Lengths measured in mm and angles measured in degrees.

Whisker	crest angle	crest width	crest minor width	crest wavelength top	crest wavelength bottom	trough angle	trough width	trough minor width	trough wavelength top	trough wavelength bottom
2.000	4.577873	0.576340	0.190628	3.864000	4.180000	1.638342	0.419719	0.250531	4.208000	4.132000
hs 2343	-11.305438	0.571314	0.193556	3.948000	3.840000	6.704194	0.428290	0.237952		
	-6.191474	0.537777	0.191638							
Whisker	crest angle	crest width	crest minor width	crest wavelength top	crest wavelength bottom	trough angle	trough width	trough minor width	trough wavelength top	trough wavelength bottom
3.000	-2.877694	0.637398	0.345178	4.788000	4.232000	-25.565940	0.607114	0.401652	4.072000	4.056000
es 3636	22.242071	0.655182	0.319438	3.932000	4.228000	-25.817691	0.583226	0.372807		
	9.312870	0.605591	0.307117							

Figure 51: Raw Whisker Measurements Case1

Whisker	crest angle	crest width	crest minor width	crest wavelength top	crest wavelength bottom	trough angle	trough width	trough minor width	trough wavelength top	trough wavelength bottom
3.000	-1.404027	0.652996	0.321457	4.160000	4.220000	-11.330407	0.519172	0.380736	4.404000	3.948000
es 3628	-4.361328	0.604897	0.305397	4.436000	4.236000	14.204711	0.513474	0.362681		
	5.352586	0.578875	0.297334							
Whisker	crest angle	crest width	crest minor width	crest wavelength top	crest wavelength bottom	trough angle	trough width	trough minor width	trough wavelength top	trough wavelength bottom
4.000	4.223248	0.651794	0.363830	4.344000	4.516000	9.302258	0.532038	0.414170	4.348000	4.264000
	-3.442646	0.632813	0.322458			13.906014	0.532601	0.390243		
Whisker	crest angle	crest width	crest minor width	crest wavelength top	crest wavelength bottom	trough angle	trough width	trough minor width	trough wavelength top	trough wavelength bottom
7.000	4.441872	0.593949	0.154299	3.684000	3.588000	-5.161822	0.466828	0.216671	3.616000	3.676000
hs 2373	9.400313	0.575517	0.165311	3.380000	3.528000	-8.620143	0.480375	0.209759		
	2.115999	0.541671	0.163155							
Whisker	crest angle	crest width	crest minor width	crest wavelength top	crest wavelength bottom	trough angle	trough width	trough minor width	trough wavelength top	trough wavelength bottom
8.000	4.520439	0.507519	0.141685	3.276000	3.648000	-6.204688	0.444113	0.188049	3.504000	3.528000
hs 2373	-17.473771	0.486230	0.160078			-7.729752	0.446094	0.169701		

Figure 52: Raw Whisker Measurements Case 2

Whisker	crest angle	crest width	crest minor width	crest wavelength top	crest wavelength bottom	trough angle	trough width	trough minor width	trough wavelength top	trough wavelength bottom
3.000	12.734017	0.598842	0.242445	4.168000	4.260000	-17.119175	1.141459	0.600906	4.504000	3.760000
es 3531	9.089322	0.544393	0.220300			24.784296	0.973275	0.579662		
Whisker	crest angle	crest width	crest minor width	crest wavelength top	crest wavelength bottom	trough angle	trough width	trough minor width	trough wavelength top	trough wavelength bottom
4.000	7.542848	0.563734	0.229240	3.516000	3.764000	13.353297	0.935248	0.531658	3.672000	3.724000
es 3531	-5.153087	0.556687	0.221038			10.665653	0.886115	0.492776		
Whisker	crest angle	crest width	crest minor width	crest wavelength top	crest wavelength bottom	trough angle	trough width	trough minor width	trough wavelength top	trough wavelength bottom
5.000	-7.897059	0.538598	0.235943	3.928000	3.892000	-30.351581	0.546205	0.268834	4.168000	3.812000
es 3527	-6.265386	0.513132	0.218449			-12.792742	0.442588	0.246292		
Whisker	crest angle	crest width	crest minor width	crest wavelength top	crest wavelength bottom	trough angle	trough width	trough minor width	trough wavelength top	trough wavelength bottom
6.000	-8.317603	0.483893	0.201585	3.396000	3.404000	-16.652916	0.397804	0.229508	3.604000	3.332000
es 3527	-9.262231	0.459761	0.185861	3.440000	3.248000	3.438078	0.366851	0.203834		
0.000	3.031409	0.416010	0.165862							

Figure 53: Raw Whisker Measurements Case 3

Whisker	crest angle	crest width	crest minor width	crest wavelength top	crest wavelength bottom	trough angle	trough width	trough minor width	trough wavelength top	trough wavelength bottom
4.000	-5.542427	0.664715	0.378179	5.232300	5.360700	-13.281643	0.605473	0.425738	5.350000	5.307200
es 3531	-10.732272	0.689507	0.448596	4.847100	4.772200	-11.612606	0.584719	0.453867	4.697300	4.847100
	-7.568746	0.690502	0.414005	4.932700	4.665200	-18.291487	0.613666	0.478052	5.125300	4.825700
	3.811964	0.643781	0.447325	4.344200	4.601000	-4.108860	0.597334	0.461885	4.547500	4.697300
	-7.306929	0.673038	0.483809	4.205100	3.680800	-11.219512	0.604929	0.494959	3.980400	4.108800
	14.370874	0.711329	0.495949			-17.038628	0.620784	0.523420		
Whisker	crest angle	crest width	crest minor width	crest wavelength top	crest wavelength bottom	trough angle	trough width	trough minor width	trough wavelength top	trough wavelength bottom
3.000	15.615928	0.476991	0.299491	3.680800	4.387000	-4.134372	0.445241	0.340654	4.130200	3.980400
es 3546	-24.555650	0.540694	0.309073	4.226500	3.616600	5.366378	0.457636	0.348143	3.712900	4.001800
	8.796527	0.524764	0.331910	3.734300	3.798500	-11.529192	0.508588	0.394558	3.969700	3.766400
	4.957610	0.557171	0.345946	4.033900	4.023200	0.000000	0.503156	0.432788	3.884100	3.905500
	5.156216	0.595294	0.374308	3.531000	3.691500	-1.194721	0.513182	0.440465	3.498900	3.616600
	-2.549461	0.601370	0.395135	4.130200	3.948300	-7.434533	0.537509	0.433992	4.568900	4.568900
	6.050277	0.609102	0.373304	3.498900	3.980400	-7.678219	0.520547	0.421330		
	-16.871293	0.608326	0.370385							
Whisker	crest angle	crest width	crest minor width	crest wavelength top	crest wavelength bottom	trough angle	trough width	trough minor width	trough wavelength top	trough wavelength bottom
2.000	-53.957408	0.886616	0.263719	4.119500	4.900600	-57.381532	0.755866	0.270541	3.916200	4.461900
es 3643	-67.137372	1.201870	0.291238	4.162300	3.531000	-67.415368	0.985039	0.282865	4.087400	4.536800
	-58.496114	0.928684	0.292413	5.189500	3.038800	-71.746522	1.194297	0.307487	4.269300	2.450300
	22.676552	0.735484	0.297684	4.183700	4.740100	-23.252781	0.569166	0.294542	4.622400	4.237200
	0.428468	0.715421	0.304033	4.697300	4.772200	-3.204880	0.574172	0.323074	4.954100	5.243000
	-2.648813	0.694594	0.331910			-17.910204	0.574098	0.340157	4.964800	4.269300
						15.330208	0.647549	0.417134		
Whisker	crest angle	crest width	crest minor width	crest wavelength top	crest wavelength bottom	trough angle	trough width	trough minor width	trough wavelength top	trough wavelength bottom
1	2.927041	0.209540	0.090951	2.257700	2.354000	0.000000	0.196280	0.089682	2.428900	2.514500
es 3600	-9.037188	0.238420	0.087461	2.557300	2.503800	-11.743386	0.210290	0.093458	2.471700	2.450300
	-2.242300	0.273479	0.083040	2.161400	2.193500	-7.329366	0.251621	0.089120	2.343300	2.364700
	-4.929298	0.311313	0.119420	2.760600	2.653600	-9.051201	0.272062	0.139577	2.664300	2.621500
	4.713727	0.325516	0.142620	2.354000	2.568000	-4.075269	0.301125	0.119209	3.038800	3.028100
	-12.224998	0.378982	0.153403	3.317000	3.145800	-3.035724	0.303067	0.143025	3.092300	3.092300
	0.753262	0.406952	0.160087	3.092300	3.135100	-2.797229	0.328884	0.137091	3.049500	3.028100
	-2.107026	0.436542	0.167907	2.996000	2.985300	-0.869850	0.352410	0.156557	2.889000	2.878300
	-1.212513	0.505653	0.186504	2.760600	2.717800	0.000000	0.393725	0.167139		
	1.096599	0.559094	0.252869							

Figure 54: Raw Whisker Measurements Case 4 (Elephant)

Whisker	crest angle	crest width	crest minor width	crest wavelength top	crest wavelength bottom	trough angle	trough width	trough minor width	trough wavelength top	trough wavelength bottom
8.000	-12.384645	0.324282	0.127874	2.867600	2.792700	-10.357201	0.267821	0.120329	2.782000	2.546600
hs 2373	-5.328733	0.345645	0.124945	2.621500	2.535900	14.624711	0.275460	0.131493	2.578700	2.675000
	1.600736	0.383039	0.121350	3.028100	2.985300	3.714586	0.330316	0.148111	3.028100	3.092300
	4.410999	0.417369	0.148696	3.006700	3.070900	-1.772482	0.345934	0.169879	3.070900	2.974600
	0.000000	0.451243	0.152170	3.295600	3.370500	5.673903	0.378794	0.166925	2.974600	3.028100
	-4.320423	0.497118	0.089682	3.188600	3.060200	1.541281	0.397811	0.146906	3.381200	3.359800
	2.681984	0.571674	0.088922	3.263500	3.274200	2.996264	0.409406	0.091966	3.381200	3.338400
	2.185606	0.561138	0.080489	3.156500	3.317000	5.861278	0.419114	0.119707	3.177900	3.231400
	-5.565147	0.606842	0.111730			2.115467	0.434801	0.112332		
Whisker	crest angle	crest width	crest minor width	crest wavelength top	crest wavelength bottom	trough angle	trough width	trough minor width	trough wavelength top	trough wavelength bottom
7.000	0.993087	0.617363	0.209295	4.344200	4.322800	0.651187	0.470739	0.267821	4.258600	4.301400
hs 2372	1.957496	0.626498	0.208616	4.494000	4.547500	-1.917927	0.479564	0.276135	4.526100	4.387000
	-0.483725	0.633698	0.237357	4.665200	4.718700	6.136904	0.500447	0.273991	4.772200	4.718700
	-2.819531	0.652568	0.244256	4.387000	4.151600	9.195854	0.502160	0.291421	4.365600	4.579600
	8.052883	0.611049	0.249441	3.830600	3.905500	-3.036387	0.505001	0.314306	4.023200	3.894800
	4.445533	0.621199	0.267148	3.370500	3.391900	4.342653	0.494578	0.323058	3.702200	3.691500
	3.405186	0.630506	0.286545			4.800598	0.511422	0.276186		
Whisker	crest angle	crest width	crest minor width	crest wavelength top	crest wavelength bottom	trough angle	trough width	trough minor width	trough wavelength top	trough wavelength bottom
6.000	2.473840	0.495792	0.150358	3.145800	3.252800	-3.456156	0.443728	0.181160	3.359800	3.252800
hs 2357	-3.464177	0.531242	0.147381	3.338400	3.295600	3.552880	0.431662	0.190379	3.391900	3.456100
	-1.098260	0.558249	0.140431	3.445400	3.391900	-0.716216	0.428000	0.205834	3.498900	3.477500
	1.595934	0.576287	0.145593	3.552400	3.595200	0.727325	0.421463	0.210148	3.584500	3.563100
	-0.526388	0.582340	0.159478	3.413300	3.456100	2.170925	0.423698	0.223868	3.370500	3.370500
	-2.645824	0.579482	0.173875	3.552400	3.413300	2.084440	0.441270	0.226318	3.424000	3.413300
	4.442284	0.552580	0.188843	3.263500	3.327700	2.770373	0.442759	0.249163	3.081600	3.092300
	1.094347	0.560245	0.197621	2.953200	2.889000	2.005617	0.458605	0.258715		
	4.207383	0.583371	0.205187							
Whisker	crest angle	crest width	crest minor width	crest wavelength top	crest wavelength bottom	trough angle	trough width	trough minor width	trough wavelength top	trough wavelength bottom
5.000	2.845973	0.538759	0.255743	3.402600	3.531000	-1.387622	0.441853	0.301453	3.488200	3.456100
hs 2347	-3.735189	0.574870	0.274308	3.605900	3.541700	0.656422	0.466985	0.320842	3.573800	3.627300
	-0.517594	0.592233	0.296115	3.841300	3.862700	-2.516876	0.487320	0.337301	3.520300	3.552400
	-1.487213	0.618405	0.330317	4.012500	3.926900	-4.120397	0.521206	0.364263	4.098100	3.755700
	2.529605	0.606087	0.340093	4.686600	4.761500	13.657794	0.566443	0.373283	4.247900	4.429800
	-0.993087	0.617363	0.361947	4.579600	4.579600	4.565519	0.537695	0.397199	4.472600	4.611700
	-0.954311	0.642446	0.369317			-2.746281	0.558300	0.408371	4.536800	4.354900
						6.785879	0.543335	0.400659		

Figure 55: Raw Whisker Measurements Case 4 (Harbor)

Whisker		crest angle	crest width	crest minor width	crest wavelength to	crest wavelength	trough angle	trough width	trough minor width	trough wavelength	trough wavelength
	8	3.462957	0.608411	0.299483	4.063500	4.021500	3.739999	0.482914	0.349880	3.969000	3.759000
es 3600		5.315692	0.623359	0.337595	4.242000	4.294500	14.105936	0.560079	0.379458	4.000500	4.137000
		2.910733	0.620323	0.345922	4.714500	4.819500	7.122084	0.550474	0.380230	4.620000	4.809000
		-1.940373	0.620211	0.351866	4.672500	4.746000	-2.857560	0.526546	0.409921	4.389000	4.483500
		-5.068764	0.653641	0.359340	4.567500	4.378500	-7.739981	0.545748	0.414246	4.777500	4.725000
		3.283752	0.641575	0.374384			-4.830049	0.561161	0.428880	4.378500	4.357500
							-3.692520	0.570634	0.441011		
Whisker		crest angle	crest width	crest minor width	crest wavelength to	crest wavelength	trough angle	trough width	trough minor width	trough wavelength	trough wavelength
	7	-6.236598	0.531600	0.277384	3.559500	3.559500	-9.430225	0.448591	0.338580	3.517500	3.454500
es 3645		-6.072896	0.545874	0.292006	3.654000	3.591000	-5.079608	0.474363	0.380121	4.326000	4.273500
		-2.739743	0.549171	0.318974	4.630500	4.399500	-1.908564	0.472908	0.372140	4.347000	4.158000
		9.041994	0.567899	0.343965	4.200000	4.515000	9.229200	0.491008	0.396723	4.116000	4.378500
		-6.656372	0.588796	0.350558	3.885000	3.864000	-5.808053	0.518795	0.399775	4.105500	3.864000
		-5.551529	0.596955	0.349773	3.811500	3.801000	7.852468	0.499551	0.413730	3.234000	3.402000
		-5.225444	0.576449	0.392955			-1.711106	0.527462	0.448399		
Whisker		crest angle	crest width	0	crest wavelength to	crest wavelength	trough angle	trough width	trough minor width	trough wavelength	trough wavelength
	6	2.119554	0.567802	0.299593	4.168500	4.326000	5.648247	0.480081	0.348127	4.137000	4.326000
es 3546		-5.492817	0.603316	0.327852	4.168500	3.948000	-5.390242	0.502987	0.363085	4.179000	4.000500
		4.742381	0.635011	0.337451	4.105500	4.273500	4.563708	0.527853	0.397426	4.273500	4.137000
		-2.680428	0.673577	0.363782	3.895500	3.853500	11.332486	0.561063	0.412349	3.664500	3.801000
		-0.905144	0.664680	0.394513	4.231500	4.168500	4.093266	0.588398	0.424341	4.452000	4.336500
		1.810061	0.664846	0.369976			9.750194	0.589007	0.433958	4.053000	4.284000
							-1.549226	0.582561	0.422729		
Whisker		crest angle	crest width	crest minor width	crest wavelength to	crest wavelength	trough angle	trough width	trough minor width	trough wavelength	trough wavelength
	5	-48.063839	0.875129	0.261932	4.074000	4.714500	-61.928867	0.922238	0.267625	4.011000	4.420500
es 3531		-56.507666	1.164625	0.291712	4.042500	4.158000	-63.878123	1.134365	0.278912	4.210500	3.885000
		-57.582186	1.218961	0.292458	5.260500	4.011000	-56.959118	1.020838	0.290161	4.242000	4.011000
		-32.252760	0.757512	0.300638	4.798500	3.895500	-51.962829	0.939867	0.308135	4.819500	4.242000
		3.952742	0.685442	0.319794	4.158000	4.546500	-38.335415	0.727916	0.363440	4.494000	4.777500
		-12.584973	0.674661	0.329179			-46.917514	0.812258	0.367399	5.985000	3.486000
							45.355474	0.922373	0.405086		

Figure 56: Raw Whisker Measurements Case 5 (Elephant)

Whisker	crest angle	crest width	crest minor width	crest wavelength to	crest wavelength	trough angle	trough width	trough minor width	trough wavelength	trough wavelength
4	-0.797186	0.377343	0.107241	3.160500	3.097500	1.052643	0.285776	0.120680	3.213000	3.202500
hs 2347	3.783351	0.397824	0.122899	2.835000	2.919000	1.892159	0.318004	0.128944	3.066000	2.971500
	-2.033778	0.443804	0.136298	3.234000	3.181500	9.747758	0.341088	0.155410	3.045000	3.118500
	1.311468	0.458767	0.135638	3.328500	3.381000	3.469819	0.346977	0.176051	3.223500	3.265500
	-1.844735	0.489265	0.152232	3.559500	3.559500	0.000000	0.352102	0.196016	3.391500	3.454500
	-1.746783	0.516692	0.159413	3.580500	3.622500	-4.809574	0.375696	0.203756	3.570000	3.517500
	-3.837573	0.549096	0.162716	3.633000	3.633000	-0.790782	0.380399	0.218457	3.591000	3.675000
	-3.639086	0.579001	0.176019			-7.012780	0.387007	0.228749	3.780000	3.675000
						0.706942	0.425509	0.248435		
Whisker	crest angle	crest width	crest minor width	crest wavelength to	crest wavelength	trough angle	trough width	trough minor width	trough wavelength	trough wavelength
3	-10.773330	0.280863	0.074727	2.341500	2.163000	10.962357	0.193254	0.073242	2.320500	2.352000
hs 2357	7.924369	0.266564	0.090518	1.932000	1.816500	5.293241	0.227635	0.083483	1.921500	1.858500
	19.443493	0.283889	0.097417	2.415000	2.488500	11.938239	0.253798	0.095650	2.394000	2.352000
	10.693969	0.311215	0.116804	2.457000	2.562000	15.639272	0.272646	0.111447	2.268000	2.373000
	0.822748	0.365620	0.126724	2.898000	2.877000	3.835379	0.313948	0.119826	2.992500	2.929500
	2.342129	0.385401	0.130794	2.940000	2.929500	9.023796	0.334726	0.144252	2.919000	2.950500
	2.847783	0.422682	0.139544	3.034500	3.055500	5.948066	0.354637	0.153377	3.034500	3.108000
	1.401563	0.429282	0.143898	3.496500	3.349500	0.000000	0.367687	0.159673	2.961000	3.087000
	9.327157	0.518290	0.158675	2.950500	3.160500	-9.291423	0.390199	0.164289	3.685500	3.580500
	-2.477595	0.485788	0.161209			-1.480770	0.406324	0.187875	2.971500	3.087000
						-9.625261	0.408185	0.198411		
Whisker	crest angle	crest width	crest minor width	crest wavelength to	crest wavelength	trough angle	trough width	trough minor width	trough wavelength	trough wavelength
2	5.902456	0.561578	0.185863	3.948000	4.095000	0.696986	0.431587	0.246316	4.074000	4.021500
hs 2372	-1.528265	0.590549	0.205422	4.021500	4.011000	3.945186	0.457835	0.249416	4.137000	4.137000
	-1.008896	0.596332	0.195618	4.189500	4.158000	3.816660	0.473229	0.251476	4.074000	4.231500
	0.490844	0.612835	0.209826	4.084500	4.210500	-5.756668	0.471069	0.269978	4.032000	4.042500
	-5.687295	0.582750	0.215602	3.990000	3.822000	-6.506441	0.463311	0.273511	3.874500	3.853500
	2.499292	0.601967	0.228382	3.622500	3.685500	-5.128335	0.469868	0.284732	3.517500	3.570000
	-0.514331	0.584851	0.230911	3.454500	3.465000	-8.494137	0.462060	0.310434		
	-1.038371	0.579406	0.250924							
Whisker	crest angle	crest width	crest minor width	crest wavelength to	crest wavelength	trough angle	trough width	trough minor width	trough wavelength	trough wavelength
1	0.482575	0.623337	0.144160	3.727500	3.706500	2.613879	0.460476	0.219527	3.748500	3.738000
hs 2373	1.407448	0.641231	0.157341	3.675000	3.685500	3.178069	0.473491	0.226939	3.748500	3.706500
	0.939159	0.640608	0.165791	3.780000	3.853500	5.686929	0.476826	0.241928	3.717000	3.706500
	-2.307864	0.651867	0.161926	3.853500	3.822000	6.377394	0.472646	0.232515	3.759000	3.874500
	-0.933750	0.644319	0.191857	3.885000	3.853500	-0.628953	0.478269	0.258238	3.906000	3.927000
	0.496283	0.606119	0.201894	3.958500	4.021500	-1.918524	0.470454	0.258583	3.916500	4.000500
	-2.520191	0.596978	0.204621			-7.119105	0.465980	0.273007	3.748500	3.759000
						-7.709316	0.469633	0.285778		

Figure 57: Raw Whisker Measurements Case 5 (Harbor)